Chapter 3

A regional model of the South African West coast

Setting up a high resolution numerical model of the ocean circulation in the surroundings of the South and West coasts of southern Africa was the direction chosen by the VIBES project to explore the physical processes affecting fish, eggs, larvae and juveniles during the recruitment cycle. This chapter provides a description of the main characteristics of the numerical tools that were set up. A detailed analysis of the numerical model output is provided and is aimed at evaluating the validity of the modeling experiments. An illustration of the potential use of such numerical tools in fisheries oceanography is provided by a set of experiments designed to investigate the effect of transport on the fish spawning products using a passive tracer.

Afin d'explorer les processus physiques affectant poissons, œufs, larves et juvéniles durant le cycle de reproduction, la direction choisit par le projet VIBES consistait en la mise au point d'un modèle numérique à haute résolution de la circulation océanique autour des côtes Sud et Ouest de l'Afrique australe. Ce chapître apporte la description des caractéristiques principales des outils numériques développés. Une analyse détaillée des sorties du modèle numérique est conduite et est employée afin d'évaluer la validité des solutions. Une illustration de l'utilisation potentielle de ces outils numériques en Océanographie des pêches est fournie par une suite d'expériences utilisant un traceur passif, développées pour étudier les effets du transport sur les produits de la ponte des poissons.

3.1 Previous modeling work conducted in the Benguela

Few attempts have been undertaken to model the shelf and slope dynamics around the South and West coast of South Africa. Van Foreest and Brundrit [1982] developed a two-mode linear numerical model using a Galerkin procedure for the vertical and applied it to the South Benguela. The surface forcing was idealized (constant northward wind stress), and the time of integration was short (3 days). Nevertheless, the solution was showing the topographic steering of the baroclinic jet of Cape Peninsula. More recently, the Princeton Ocean Model (POM), a sigma coordinate model, has been applied to simulate the circulation around the Southern Africa from about 46^o S to 12^o S and 4^o E to 30^o E [*Skogen,* 1998]. 18 bottom following σ-layers are used in the vertical, and the horizontal resolution is 20 km. We can note that a condition of zero barotropic velocities is given for the initial and boundary conditions. The simulations are forced using data of a specific year. The results showed most of the characteristic features of the circulation of the Benguela, but the resolution was too coarse to resolve the mesoscale characteristics patterns that develops on the shelf in the West Coast area. Several basin-scale models had the Benguela included in their simulation domains [*Barnier et al.,* 1998, *Biastoch and Krauß,* 1999, *Marchesiello,* 1995, *de Miranda,* 1996]. But their resolutions were also too coarse (1/3 of a degree for the bests) to provide a satisfactory circulation pattern for the transport of eggs and larvae around the South and West coasts of South Africa .

3.2 Model description

The first developed oceanic primitive equation models were using for the vertical, the geopotential coordinate z. In this case the bottom topography is represented by steps in the grid. This was not satisfactory for the simulation of bottom flows along the topography, of particular importance in coastal dynamics. Thus, traditionally in coastal modeling, it has been preferred to use models in which the vertical coordinate follows the topography.

For this study, we use ROMS (the Regional Ocean Modeling Systems), a community code developed by the modeling groups at Rutgers University (USA) and at University of California Los Angeles (USA). It belongs to a hierarchy of terrain-following models originated with the semi-spectral primitive equation model (SPEM, [*Haidvogel et al.,* 1991]), which solves the hydrostatic primitive equations with a rigid lid at the sea surface, coupled with advection/diffusion equations for potential temperature and salinity and the nonlinear UNESCO equation of state. SCRUM (S-coordinate Rutgers University Model), a free sea surface version of SPEM has been developed by Song and Haidvogel [1994]. It improves upon SPEM by allowing for a generalized nonlinear terrain-following coordinate, which provides enhanced resolution at either the sea surface or sea floor. This feature might be of importance for the biology, since biological activity occurs mostly in the surface oceanic layers. ROMS represents an evolution of SCRUM, including several substantial developments required to efficiently and robustly calculate the coastal circulations at high spatial resolution, such as subgrid scale parameterization, high order schemes, and high performance computing on SMP-class computer architecture (like the SGI Origin 2000 of the University of Cape Town).

3.2.1 Equations of motion

The equations of motion in Cartesian coordinates, following the Boussinesq and hydrostatic approximations, take the form:

$$\frac{\partial u}{\partial t} = -u\frac{\partial u}{\partial x} - v\frac{\partial u}{\partial y} - w\frac{\partial u}{\partial z} + fv - \frac{\partial \phi}{\partial x} + \mathcal{F}_u + \mathcal{D}_u \tag{3.1}$$

$$\frac{\partial v}{\partial t} = -u\frac{\partial v}{\partial x} - v\frac{\partial v}{\partial y} - w\frac{\partial v}{\partial z} - fu - \frac{\partial \phi}{\partial y} + \mathcal{F}_v + \mathcal{D}_v \tag{3.2}$$

$$\frac{\partial T}{\partial t} = -u\frac{\partial T}{\partial x} - v\frac{\partial T}{\partial y} - w\frac{\partial T}{\partial z} + \mathcal{F}_T + \mathcal{D}_T \tag{3.3}$$

$$\frac{\partial S}{\partial t} = -u\frac{\partial S}{\partial x} - v\frac{\partial S}{\partial y} - w\frac{\partial S}{\partial z} + \mathcal{F}_S + \mathcal{D}_S \tag{3.4}$$

$$\rho = \rho(T, S, P) \tag{3.5}$$

$$\frac{\partial \phi}{\partial z} = -\frac{\rho g}{\rho_0} \tag{3.6}$$

$$0 = \frac{\partial u}{\partial x} + \frac{\partial v}{\partial y} + \frac{\partial w}{\partial z} \tag{3.7}$$

With the vertical boundary conditions prescribed as follows:

$$\text{at the top: } z = \zeta \quad \kappa_M \frac{\partial u}{\partial z} = \tau^x_{surf} \tag{3.8}$$

$$\kappa_M \frac{\partial v}{\partial z} = \tau^y_{surf} \tag{3.9}$$

$$\kappa_T \frac{\partial T}{\partial z} = \frac{Q_T}{\rho_0 C_p} \tag{3.10}$$

$$\kappa_S \frac{\partial S}{\partial z} = \frac{(E - P)S}{\rho_0} \tag{3.11}$$

$$w = \frac{\partial \zeta}{\partial t} + u\frac{\partial \zeta}{\partial x} + v\frac{\partial \zeta}{\partial y} \tag{3.12}$$

$$\text{at the bottom: } z = -h \quad \kappa_M \frac{\partial u}{\partial z} = \tau^x_{bot} \tag{3.13}$$

$$\kappa_M \frac{\partial v}{\partial z} = \tau^y_{bot} \tag{3.14}$$

$$\kappa_T \frac{\partial T}{\partial z} = 0 \tag{3.15}$$

$$\kappa_S \frac{\partial S}{\partial z} = 0 \tag{3.16}$$

$$w = -u\frac{\partial H}{\partial x} - v\frac{\partial H}{\partial y} \tag{3.17}$$

Where,

- x, y, z are the coordinates in the Cartesian frame (z being the vertical, increasing towards the top)
- u, v, w are components of the velocity vectors in this frame
- f is the Coriolis parameter
- ϕ is the dynamic pressure
- $\mathcal{F}_u$, $\mathcal{F}_v$, $\mathcal{F}_T$, $\mathcal{F}_S$ are the forcing terms

- $\mathcal{D}_u$, $\mathcal{D}_v$, $\mathcal{D}_T$, $\mathcal{D}_S$ are the dissipation terms
- T is the potential temperature of the Ocean
- S is the salinity of the Ocean
- P is the total pressure
- $\rho_0 + \rho$ is the total in-situ density
- g is the acceleration of gravity
- ζ is the free surface elevation
- κ_M, κ_T, κ_S are the vertical turbulent mixing coefficients, defined by a vertical turbulent closure scheme
- τ^x_{surf}, τ^y_{surf} are the surface wind stress components
- Q_T is the surface heat flux
- $E - P$ is the evaporation minus the precipitation
- τ^x_{bot}, τ^y_{bot} are the bottom stress components, the bottom stress is parameterized in a sum of linear and quadratic terms:

$$\tau^x_{bot} = \left(\gamma_1 + \gamma_2\sqrt{u^2 + v^2}\right) u \tag{3.18}$$

$$\tau^v_{bot} = \left(\gamma_1 + \gamma_2\sqrt{u^2 + v^2}\right) v \tag{3.19}$$

- H is the resting thickness of the water column

Equations (3.1) and (3.2) express the momentum balance in the x and y directions. Equations (3.3) and (3.4) express the time evolution of Temperature and Salinity. Equation (3.5) gives the non-linear equation of state. Under the hydrostatic approximation, the momentum balance in the vertical direction limits itself to a balance between the pressure gradient and the buoyancy forces (3.6). In the Boussinesq approximation, density variations are neglected in the momentum equations except in their contribution to the buoyancy forces in the vertical momentum equation (3.6). Equation (3.7) expresses the continuity equation for an incompressible fluid.

3.2.2 The s stretched vertical coordinate system and the horizontal curvilinear coordinates

With an active sea surface, a generalized topography-fitting coordinate takes the form:

$$s = s\left(\frac{z - \zeta}{H + \zeta}\right) \quad -1 \leq s \leq 0 \tag{3.20}$$

As an extension to standard terrain-following transformations, a nonlinear stretching of the vertical coordinate is applied that depends on local water depth [*Song and Haidvogel,* 1994].

It can be used to generate a more uniform vertical resolution near the surface (or the bottom) and consequently a better representation of the mixed layer and the thermocline. The transformation used in SCRUM and ROMS is:

$$z = h_s + (h - h_s)C(s) \tag{3.21}$$

where h_s is a constant to be chosen as a typical surface mixed layer depth, and

$$C(s) = (1 - \theta_b)\frac{\sinh(\theta s)}{\sinh(\theta)} + \theta_b \frac{\tanh\left[\theta(s + 1/2)\right] - \tanh(\theta/2)}{2\tanh(\theta/2)} \tag{3.22}$$

For large θ, the coordinate lines are more tightly confined to the surface; additionally, if θ_b approaches 1, resolution at the bottom boundary is enhanced. These possibilities might be of great importance for the coupling with the biological components. The vertical velocity in the s coordinate is defined as:

$$\Omega = \frac{\partial s}{\partial z}\left[w - (1 + s)\frac{\partial \zeta}{\partial t} - u\left(\frac{\partial z}{\partial x}\right)_s - v\left(\frac{\partial z}{\partial y}\right)_s\right] \tag{3.23}$$

In the transformed coordinate system, the kinematic boundary conditions (3.12) and (3.17), at the surface ($s = 0$) and at the bottom ($s = -1$) simplify to:

$$\Omega = 0 \tag{3.24}$$

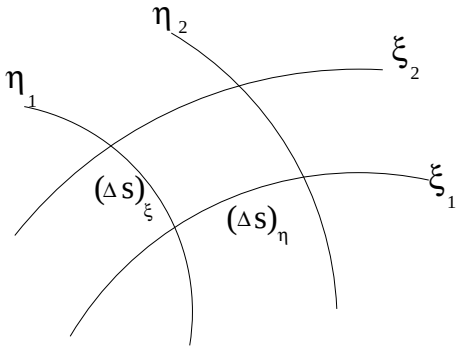

Figure 3.1 Curvilinear coordinates.

In the horizontal, like SPEM and SCRUM, ROMS is written in horizontal curvilinear coordinates. This system can conform to irregular lateral boundaries or allows the placing of more computational resolution in regions of interest. These new coordinates are introduced by a transformation in the horizontal coordinate from (x,y) to (ξ, η), where the relationship of horizontal arc length to the differential distance is given by:

$$(ds)_\xi = \left(\frac{1}{m}\right) d\xi \tag{3.25}$$

$$(ds)_\eta = \left(\frac{1}{n}\right) d\eta \tag{3.26}$$

Here, $m(\xi, \eta)$ and $n(\xi, \eta)$ are the scale factors which relate the differential distances $(\Delta\xi, \Delta\eta)$ to the physical arc lengths $((\Delta S)_\xi, (\Delta S)_\eta)$ (figure 3.1). Coastal boundaries can also be specified as a finite-discretized grid via land/sea masking.

3.2.3 Discretization

In the horizontal direction (ξ, η), except where noted below, a centered second-order finite difference approximation is adopted on an Arakawa "C" grid (figure 3.2), which is well suited for problems with horizontal resolution that is fine compared to the first radius of deformation [*Hedström,* 1997].

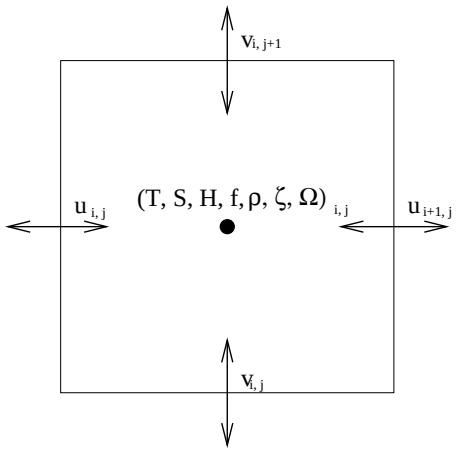

Figure 3.2 Position of the variables on the Arakawa horizontal C-grid.

The vertical also uses a second-order finite-difference approximation. Just as we use a staggered grid in the horizontal, the grid is staggered also in the vertical (figures 3.3 and 3.4). These choices are traditional for second-order, finite differences models, and provide for conservation of the first and second moments of momentum and tracers [*Haidvogel et al.,* 2000].

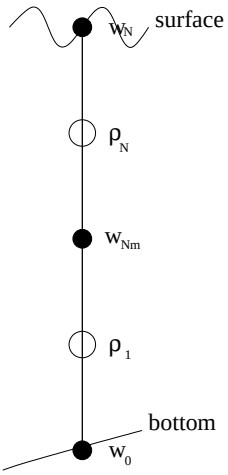

Figure 3.3 Position of variables on the staggered vertical grid.

For computational economy, the hydrostatic primitive equations for momentum are solved using a split-explicit time-stepping scheme which requires a special treatment and coupling between barotropic (fast) and baroclinic (slow) modes. A finite number of barotropic time steps, within each baroclinic step, are carried out to evolve the free-surface and vertically integrated momentum equations. In order to avoid the errors associated with the aliasing of frequencies resolved by the barotropic steps but unresolved by the baroclinic step, the barotropic fields are time averaged before they replace those values obtained with a longer

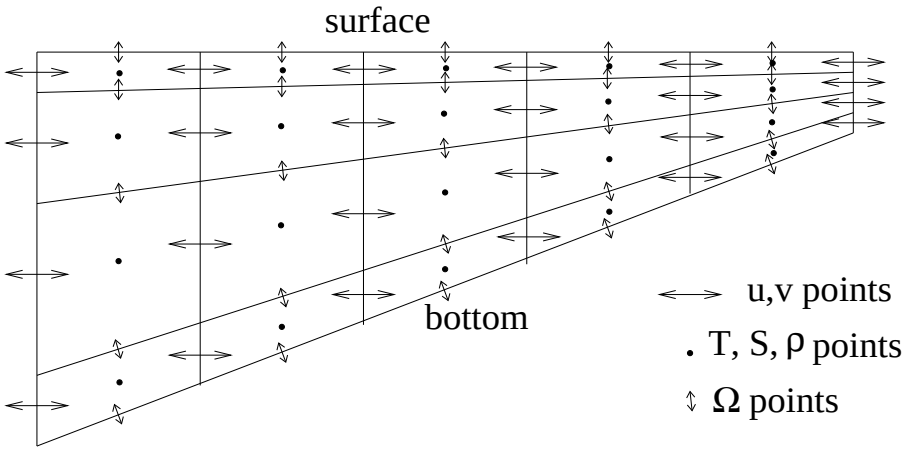

Figure 3.4 Placement of variables on a ROMS cross section.

baroclinic step. A cosine-shape time filter, centered at the new time level, is used for the averaging of the barotropic fields. In addition, the separated time-stepping is constrained to maintain exactly both volume conservation and constancy preservation properties which are needed for the tracer equations. Currently, all 2D and 3D equations are time discretized using a third-order accurate predictor (Leap-Frog) and corrector (Adams-Molton) time-stepping algorithm which is very robust and stable. The enhanced stability of the scheme allows larger time steps than in more traditional numerical scheme, by a factor of four, which more than offsets the increased cost of the predictor-corrector algorithm.

3.2.4 The pressure gradient scheme

The major advantage of sigma coordinate models is the transformation of the surface and sea bottom to coordinate surfaces. Unfortunately, this is also the source of their major disadvantage: the well known pressure gradient error. In linear σ coordinate, the x-component of the pressure gradient force is determined by the sum of 2 terms:

$$\frac{\partial p}{\partial x}\Big)_{z=cst} = \frac{\partial p}{\partial x}\Big)_{\sigma=cst} - \frac{\sigma}{h}\frac{\partial p}{\partial \sigma}\frac{\partial h}{\partial x} \tag{3.27}$$

The first term of the right involves the variation of pressure along a constant σ-surface and the second is the hydrostatic correction. Near steep topography, these 2 terms are large, comparable in magnitude and tend to cancel each other. A small error in computing either term can result to a relatively large error in the resulting horizontal pressure gradient [*Song,* 1998]. Another source of error, the hydrostatic inconsistency [*Haney,* 1991], can occur when using second order central differences in the discretization of equation (3.27). It can be demonstrated that the second order discretization of equation (3.27) is equivalent to interpolating pressure between the contiguous sigma layers to obtain the horizontal pressure gradient [*Kliem and Pietrzak,* 1999]. Hydrostatic inconsistency arises if the slope and horizontal resolution are such that extrapolation is performed instead of interpolation. Kliem and Pietrzak [1999] and Song [1998] proposed different ways to reduce errors:

- Reducing the truncation error in the derivation of equation (3.27) by subtracting an horizontally homogeneous averaged density $\bar{\rho}(z)$ to the density field. This trick has an efficiency only for small domains, where the horizontal variations in density are limited.

- Interpolating density back to z levels before computing the pressure gradient. Problems can arise with the lowest and highest σ levels that could require extrapolations over steep topography.
- Using higher-order numerical schemes.
- Retaining integral properties. The best pressure gradient formulation should minimize truncation errors while retaining integral properties such as mass, energy and vorticity.

The scheme implemented in ROMS is the weighted Jacobian formulation proposed by Song [1998]. This formulation has been designed to minimize truncation errors and to retain integral properties. If s is the generalized topographic following coordinate system, the horizontal pressure gradient can be rewrite in a Jacobian form:

$$\frac{\partial p}{\partial x}\Big)_{z=cst} = \frac{\partial p}{\partial x}\Big)_{z=\zeta} + \frac{g}{\rho_0}\int_s^0 \left\{ \frac{\partial z}{\partial s'}\frac{\partial \rho}{\partial x} - \frac{\partial z}{\partial x}\frac{\partial \rho}{\partial s'} \right\} ds' \tag{3.28}$$

Hence, vertical variations in the horizontal pressure gradient are given by an integral of the Jacobian:

$$J(z,\rho) = \frac{\partial z}{\partial s}\frac{\partial \rho}{\partial x} - \frac{\partial z}{\partial x}\frac{\partial \rho}{\partial s} \tag{3.29}$$

Song [1998] defined the standard Jacobian formulation as the second order central difference discretization of equation (3.29). He proposed another scheme, the weighted Jacobian, centered in z space rather than in s space, as for the standard Jacobian. In an idealized case, Song [1998] shows that whereas the standard Jacobian outperforms the weighted Jacobian when the hydrostatic consistency condition is satisfied, the weighted Jacobian gives superior results if the condition is violated (which is often the case in realistic configurations). The conservation of momentum and energy and the accurate representation of the bottom pressure torque has been validated [*Song and Wright,* 1998]. The conservation of these properties can constrain model errors.

3.2.5 The advection scheme

A classic approach in Ocean modeling for the treatment of advection is the use of second order central difference schemes. In conjunction, Laplacian, higher-order diffusion operators or low-pass spatial filters are employed to smooth the numerical noise induced by dispersive computational errors or turbulent cascades. The advection operator for the momentum and tracer variables in ROMS has been redesigned to reduce dispersive errors. It consists of an upstream-biased third order scheme. Using this scheme, explicit smoothing of the fields is no longer mandatory, enhancing the effective resolution of the solution for a given grid [*Shchepetkin and McWilliams,* 1998].

3.2.6 The turbulent closure scheme

The parameterization of the unresolved physical vertical mixing processes in ROMS is done via a non-local, K-profile planetary (KPP) boundary layer scheme [*Large et al.,* 1994]. Two distinct parameterizations are conducted: one for the ocean interior and one for the oceanic surface boundary layer. The boundary layer depth (h) depends on the surface forcing, the buoyancy and the velocity profile and is determined by equating a bulk Richardson number relative to the surface to a critical value. Below the boundary layer, the vertical mixing

is regarded as the superposition of 3 processes: vertical shear, internal wave breaking, and double diffusion. In the surface layer, the diffusivity is formulated to agree with a similarity theory of turbulence. At the base of the surface layer, both diffusivity and its gradient have to match the interior values. The KPP model has been shown to simulate accurately processes such as convective boundary layer deepening, diurnal cycling, and storm forcing.

3.3 Configuration

3.3.1 The grids

Several arguments constrain the choices for the computational domain:

- the domain must be large enough so that the most important dynamic features for the transport of eggs and larvae have enough space to develop. This includes the upwelling filaments that extend several hundred of km offshore, the Agulhas retroflection, etc...
- the domain must be small enough so that we can keep a high resolution at a reasonable computational cost.
- the open boundaries should cross the current at right angles. They should be placed where there is a minimum in current velocities and in variability, they should also be placed where the topographic gradient perpendicular to the boundary is as small as possible to avoid along-boundary currents [*Penduff,* 1998].

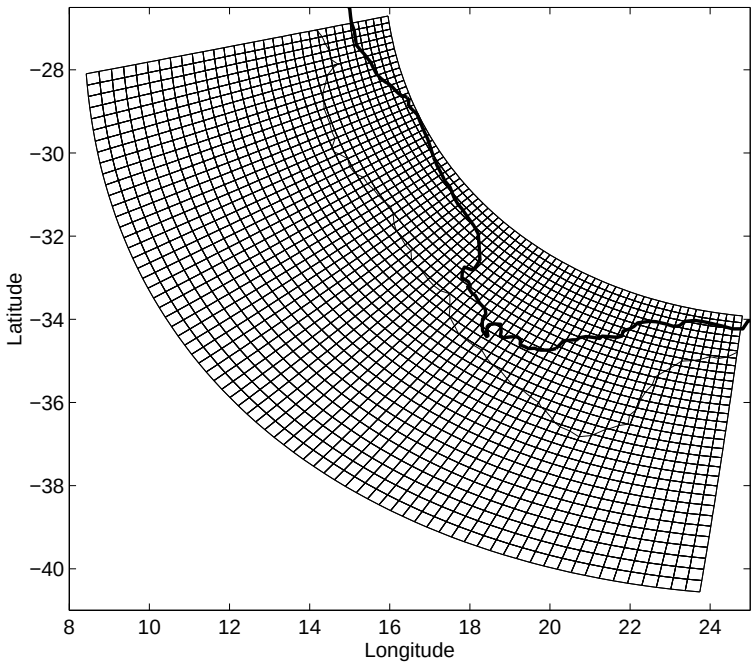

Figure 3.5 The pie shaped grid for the low resolution experiment. The dark line represent the coastline and the 500 m isobath is an indicator of the position of the shelf break.

To satisfies these criteria, the grid has been built following the arc of a circle. It follows roughly the South-west corner of Africa and the resolution is identical in the ξ and η directions. This way, the number of masked points, that are a dead weight in computing the solution, has

been reduced. To facilitate the connections to the open Ocean, the Northern and Eastern open boundaries cut the shelf in its narrowest parts at about respectively 27.5^o S and 24.5^o E. Hence, the model domain includes all the South and South-West coasts of South Africa from Lüderitz to Cape St. Francis (figure 3.5). The Eastern boundary is not at a place where the currents are weak, since it cuts the strong Agulhas Current. We rely on a specific open boundary scheme to handle this feature properly. The offshore boundary is placed beynd the shelf break, on the ocean plane, roughly 300 kilometers away from the tip of the Agulhas Bank. This way, the domain is 1300 km long in its inner radius (at the coast), 2240 km long offshore, and 740 km wide. Two kinds of grid have been realized:

- a low resolution one where the resolution is linearly ranging from 18 km at the coast to 31 km offshore.
- a high resolution one where the resolution is linearly ranging from 9 km at the coast to 16 km offshore.

Note that the grid is isotropic and thus doesn't produce a dissymetry in the dissipation of the turbulence. The resolution is higher at the coast where we need a more accurate solution. The first baroclinic Rossby radius of deformation is everywhere resolved in the high resolution experiment.

Although the pressure gradient scheme should allow the use of a steeper slope, some degree of topographic smoothing may be necessary to ensure stable and accurate simulations using realistic bathymetry. A useful parameter is found to be:

$$r = \frac{\Delta h}{2h} = \frac{h^{+1/2} - h^{-1/2}}{h^{+1/2} + h^{-1/2}} \tag{3.30}$$

Empirical studies have shown that robust results are obtained if r does not significantly exceed a value of 0.2 [*Haidvogel et al.,* 2000]. To filter the topography only where it is needed, we used a Shapiro filter weighted by the values of r: if r is smaller than a target value (here, 0.15), the weight is 0; if r is bigger, the weight is 1. The filter has been passed on the topography until $r < 0.24$ for the low resolution experiments and until $r < 0.15$ for the high resolution experiments. The low resolution experiment has a bigger r value because it was not possible to filter further the topography at this resolution without removing all the shelf on the West Coast (see for example figure 3.8).

Comparing figure (3.6) and figure (3.7), one can note that whereas some features like the Cape Canyon or the steep wall just South of the Agulhas Bank have been filtered out, the major topographical characteristics remain in the bathymetry used for the high resolution experiment. Although smaller, the Agulhas Bank is approximately well represented as well as the widening of the shelf in St. Helena Bay or the narrowing of the shelf South of Lüderitz. The filtering has removed the narrow shelf in the Cape Peninsula area. For the low resolution grid, most of the topographical features have been filtered out and there only remains a very smoothed shelf break that follows the coastline. Tests have been conducted for the high resolution configuration with a neutral stratification to validate the value of the smoothing on the pressure gradient error.

On the vertical, we have chosen N=20 vertical levels. It would have been interesting to use more vertical levels to resolve more accurately the bottom layers, but tests along a vertical slice with an increased number of vertical levels did not produce a significant improvement of the solution. The minimum depth has been fixed at 30 meters and the maximum depth at 5000 meters. The number of levels were concentrated at the surface where most of the

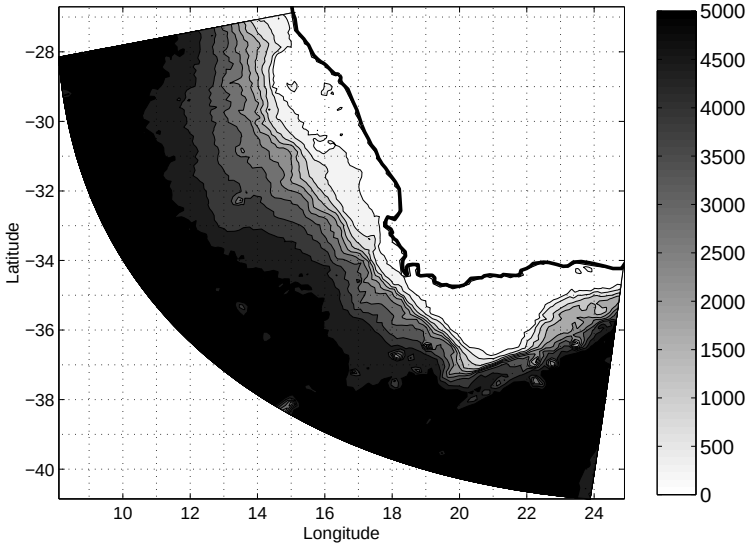

Figure 3.6 Raw ocean topography (greyscale range in meters) from the ETOPO2 dataset.

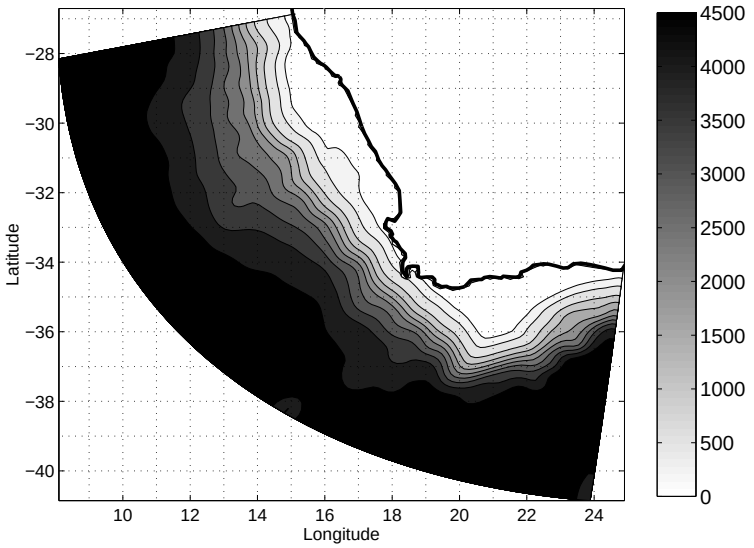

Figure 3.7 Smoothed ocean topography (greyscale range in meters) for the high resolution experiment.

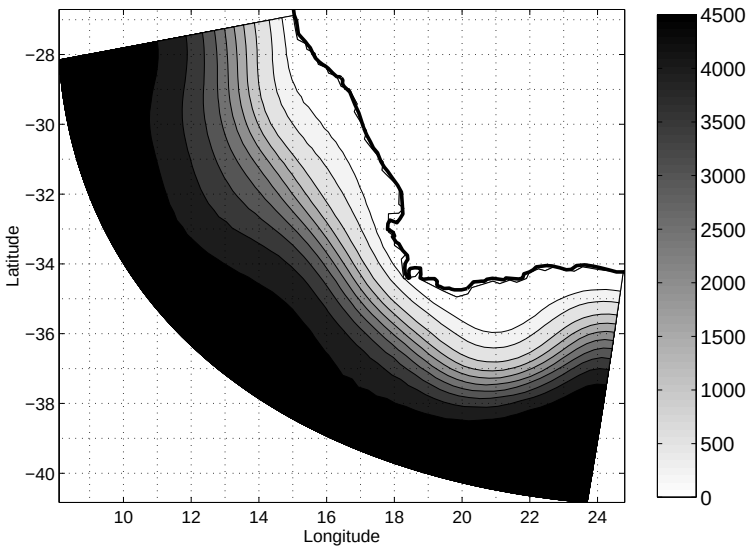

Figure 3.8 Smoothed ocean topography (greyscale range in meters) for the low resolution experiment.

variability occurs and to keep a good resolution for the biological components (table 3.3.1 and figure 3.9). To do so, θ has been chosen equal 7, θ_b equal 0.3, and h_s equal 20 meters. Note that with these parameter values, the resolution is less than 5 meters everywhere at the surface, but can be really coarse on the bottom of the deep ocean (more than 1000 m when h=5000 m) (table 3.3.1).

3.3.2 Surface fluxes

The atmospheric forcing fields are based on monthly climatologies derived from the Comprehensive Ocean-Atmosphere Data Set (COADS) [*Da Silva et al.,* 1994]. The momentum forcing is given by the longitudinal and latitudinal components of the wind stress. One can note on figure (3.10) that on the South Coast, the climatological wind field in never favorable to upwelling. North of 30^o S the upwelling favorable wind is perennial throughout the year, whereas it is seasonal South of 30^o S [*Shillington,* 1998]. A cyclonic wind stress curl is present on the shelf associated with the upwelling favorable wind.

Setting up the thermohaline forcing of an ocean is less straightforward. The specification of the surface fluxes alone may lead to an undesirable drift of the model fields as it neglects the feed-back to the atmosphere entirely. Therefore, basin scale models are often forced by nudging towards monthly mean climatological surface fields. A method physically more satisfactory is to linearize the thermal forcing around climatological sea surface temperature (T_{clim}), in order to represent the model sea surface temperature (T_{mod}) feedback on the surface heat fluxes [*Barnier et al.,* 1998], as

$$Q_T = Q_{net} + \frac{\partial Q}{\partial T_{clim}} (T_{mod} - T_{clim}) \tag{3.31}$$

The term $\frac{\partial Q}{\partial T_{clim}}$ is computed as Q_{net} from the different contributions for the heat fluxes: infrared, sensible heat, and latent heat [Siefridt, 1994]:

Level	at h_{min}	at h_{moy}	at h_{max}
20	0.0	0.0	0.0
19	-1.0	-2.8	-4.7
18	-2.0	-6.5	-11.0
17	-3.0	-11.9	-20.7
16	-4.1	-20.5	-36.9
15	-5.1	-35.2	-65.2
14	-6.2	-61.1	-116.0
13	-7.4	-106.4	-205.5
12	-8.7	-181.7	-354.8
11	-10.1	-294.2	-578.3
10	-11.7	-436.9	-862.2
9	-13.3	-586.2	-1159.0
8	-14.8	-719.0	-1423.2
7	-16.3	-831.1	-1645.8
6	-17.7	-934.0	-1850.4
5	-19.1	-1045.7	-2072.2
4	-20.7	-1184.8	-2348.9
3	-22.4	-1371.8	-2721.2
2	-24.5	-1631.7	-3238.9
1	-26.9	-1997.5	-3968.1
0	-30.0	-2515.0	-5000.0

Tab. 3.1 Vertical s-coordinate system: depth in meters of the s levels for the w-points. The other variables are at intermediate levels.

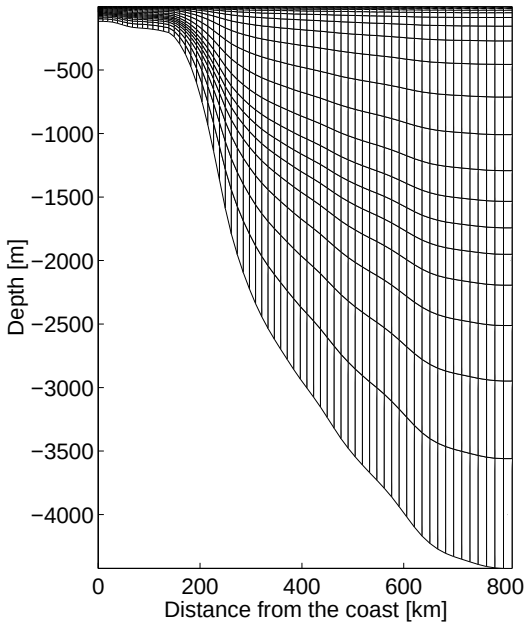

Figure 3.9 Vertical s-coordinate system: vertical levels of the ρ points for a section across the shelf North of St Helena Bay.

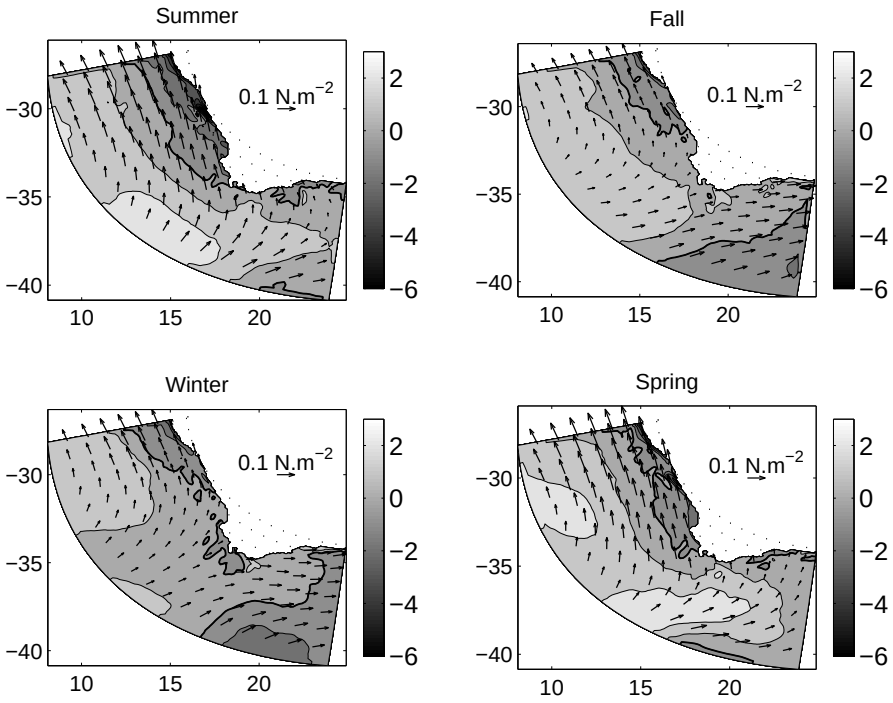

Figure 3.10 Wind stress based on the COADS monthly climatology (1 vector is portrayed every 8 vectors). The greyscale range represent the wind stress curl ($\times 10^-7$) in N.m^{-3}.

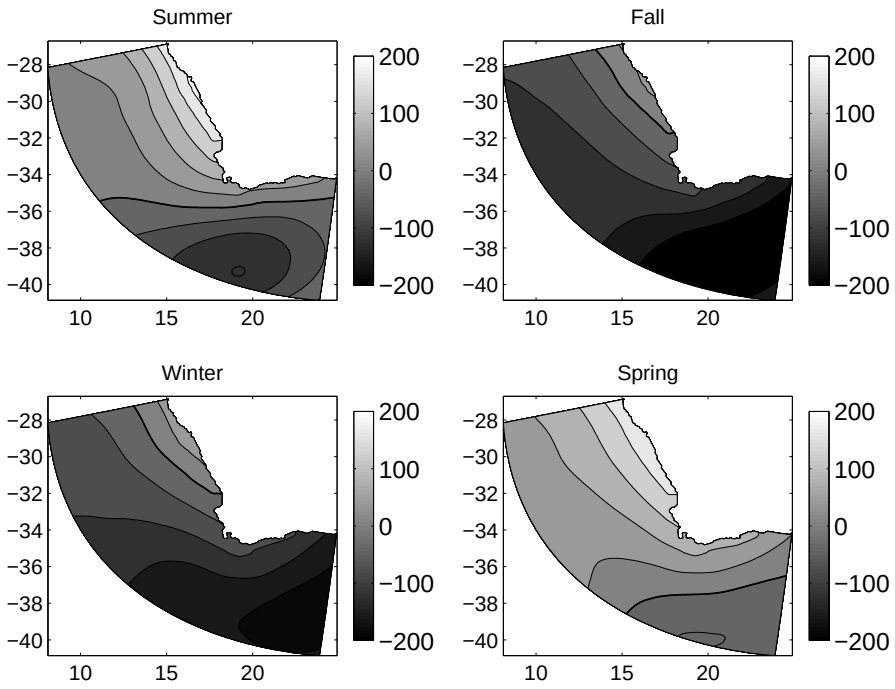

Figure 3.11 Net heat flux in W.m^{-2} based on the COADS monthly climatology.

$$\frac{\partial Q}{\partial T_{clim}} = -4\,\sigma\,T_{clim}^3 - \rho_{atm}\,C_p\,C_h\,U - \rho_{atm}\,C_e\,L\,U \times 2353\log(10)\,q_s\,T_{clim}^{-2} \tag{3.32}$$

Where σ is the constant of Stefan, C_p is the specific heat of the atmosphere, C_h is the sensible heat transfer coefficient, U is the wind speed, C_e is the latent heat transfer coefficient, L is the latent heat of vaporization, and q_s is the sea level specific humidity. The term $\frac{\partial Q}{\partial T_{clim}}$ is portrayed on figure 3.12. For a mixed layer depth of 50 m it corresponds to a nudging coefficient toward the climatology ranging from about 50 days in the South to a maximum 90 days in the West Coast. Figure (3.13) shows the sea surface temperature used for the correction of the surface heat flux, obtained from the COADS dataset. In this dataset, the Agulhas Current and the upwelling system are poorly represented.

The fresh water fluxes are specified as salt fluxes based on the climatological precipitation (P) and evaporation (E) fields (figure 3.14). The use of E-P data independent of the model solution can induce a drift of the model solution [*Haidvogel et al.,* 2000]. To counter this behavior a correction term for the surface salinity flux has been added to the formulation, identically to the heat flux correction term. We obtain:

$$\text{Salt flux} = \frac{(E-P)S_{mod}}{\rho_0} + \text{Cff}\,(S_{mod} - S_{clim}) \tag{3.33}$$

This method has been chosen for our configuration, using a nudging coefficient, corresponding to 75 days, the same order of magnitude as the averaged value of the heat flux correction term. Unfortunately, a bug has crept into the model and the salinity flux remained equal to zero during all the simulations. Nevertheless, the cold water doesn't evaporate dramatically in an upwelling system and the precipitation in the Benguela is low (figure 3.14). This induces low values for the E-P field of the West Coast. The salinity fluxes coming from the lateral

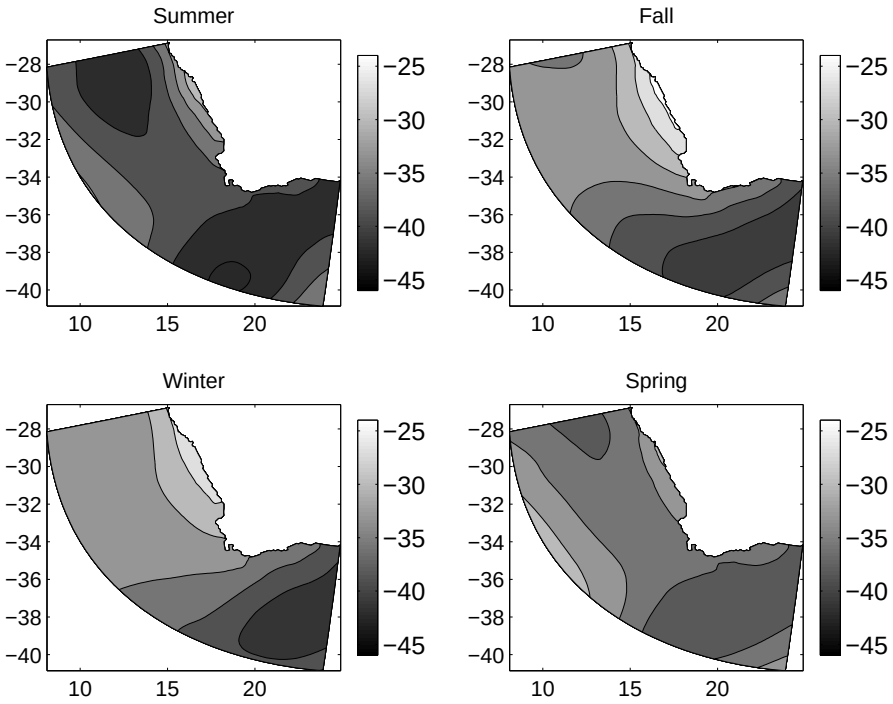

Figure 3.12 Linear dependence of the net heat flux on the sea surface temperature in $W.m^{-2}.C^{-1}$ based on the COADS monthly climatology.

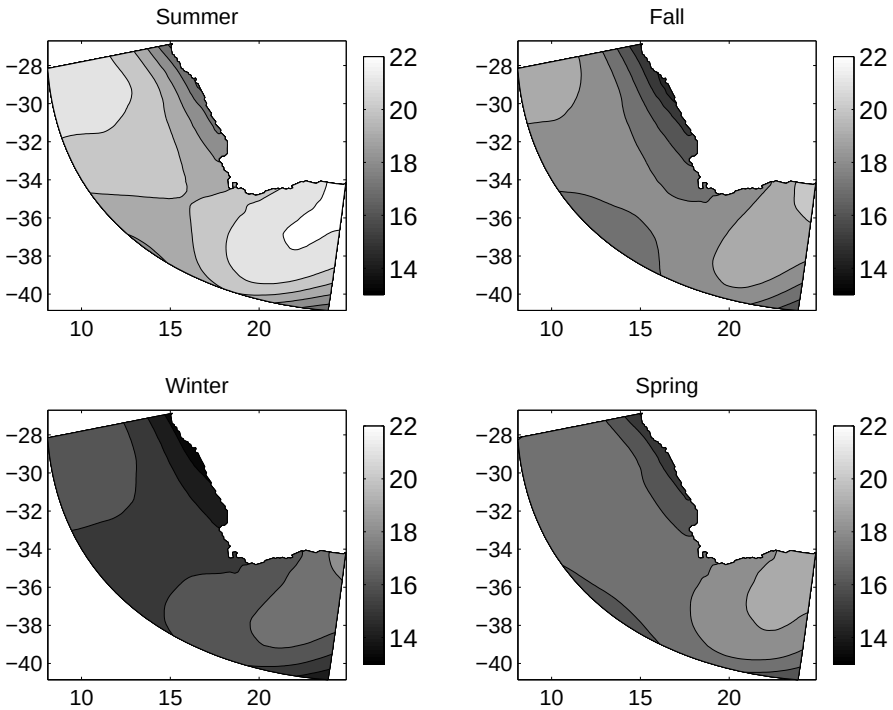

Figure 3.13 Sea surface temperature (^oC) of the COADS monthly climatology, used in the net heat flux correction term.

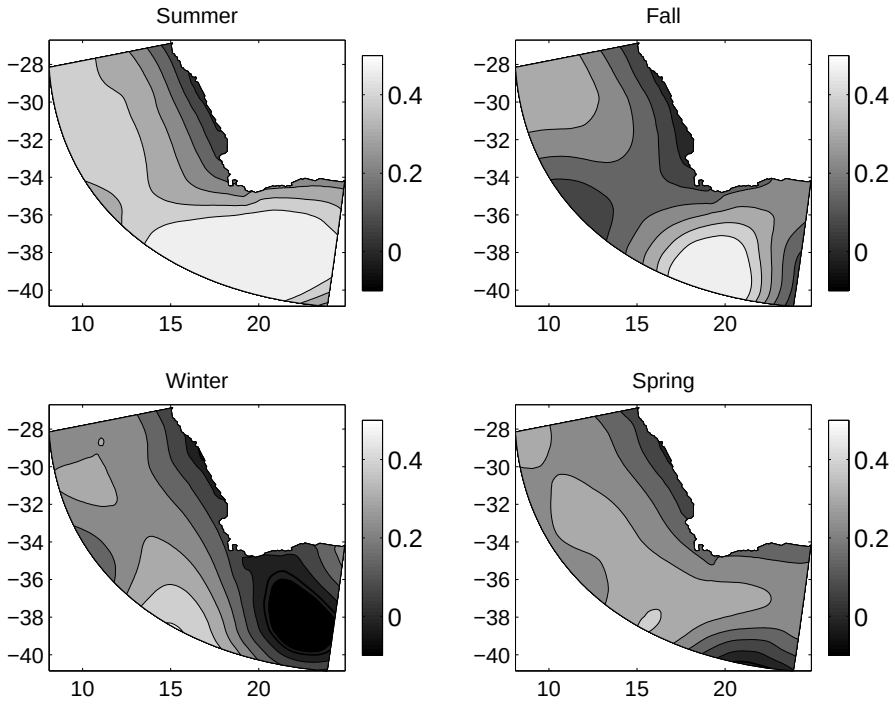

Figure 3.14 Evaporation minus precipitation (cm.day^{-1}) of the COADS monthly climatology.

boundaries should overwhelm the surface flux. Hence, we expect the solution to not drift excessively from the climatology values.

3.3.3 Initial and boundary conditions

(a) Open boundary scheme

Coastal modeling requires well behaved, long term solutions for configurations with open boundaries on up to 3 sides. A numerical boundary scheme should allow the inner solution to radiate through the boundary without reflection and information from the surrounding ocean to come into the model. The active open boundary scheme implemented in ROMS estimates the two dimensional horizontal phase velocities in the vicinity of the boundary [*Marchesiello et al.*, 2000]. For each model variable ϕ, following Raymond and Kuo [1984], the normal (c_x) and tangential(c_y) phase velocities are:

$$c_x = -\frac{\frac{\partial\phi}{\partial t}\frac{\partial\phi}{\partial x}}{(\frac{\partial\phi}{\partial x})^2 + (\frac{\partial\phi}{\partial y})^2} \tag{3.34}$$

$$c_y = -\frac{\frac{\partial\phi}{\partial t}\frac{\partial\phi}{\partial y}}{(\frac{\partial\phi}{\partial x})^2 + (\frac{\partial\phi}{\partial y})^2} \tag{3.35}$$

If the propagation is towards the open ocean, the features produced inside the model are evacuated following the wave equation:

$$\frac{\partial\phi}{\partial t} + c_x\frac{\partial\phi}{\partial x} + c_y\frac{\partial\phi}{\partial y} = \frac{\phi_{data} - \phi}{\tau_{out}} \tag{3.36}$$

If the propagation is towards the interior, the value at the boundary is nudged towards data:

$$\frac{\partial \phi}{\partial t} = \frac{\phi_{data} - \phi}{\tau_{in}} \tag{3.37}$$

The tangential and normal propagations are discretized in ROMS in an upstream biased fashion, where the normal component is treated implicitly. Hence, this scheme allows large time steps without loss of stability. At the corners the averaged value of the two adjacent boundary points is taken. Mass conservation is enforced around the model domain [*Marchesiello et al.,* 2000]. The inflow/outflow split scheme can cause problems in the sense that a grid point can be an inflow for one process and an outflow for another (for example the Eastern boundary is an inflow boundary for the Agulhas Current and the barotropic Rossby waves, but it is an outflow boundary for coastal trapped waves and Kelvin waves). A series of actions are taken to counter this problem in order to obtain a long term satisfactory behavior of the solution:

(1) The solution is weakly relaxed towards data in outflow conditions [right term of equation (3.36)].

(2) The solution is weakly nudged towards data in nudging bands close to the boundaries. The nudging coefficient is linearly decreasing in the 6 points near the boundaries (figure 3.15).

(3) Whereas no explicit mixing is mandatory in the model domain, a sponge layer with linearly increasing lateral mixing coefficient (figure 3.16) filters out the possible numerical noise or reflections produced by the open boundaries. Recent simulations of the US West Coast ocean model [*Marchesiello et al.,* 2000] have shown that with the active boundary condition schemes, the sponge layers were no longer necessary.

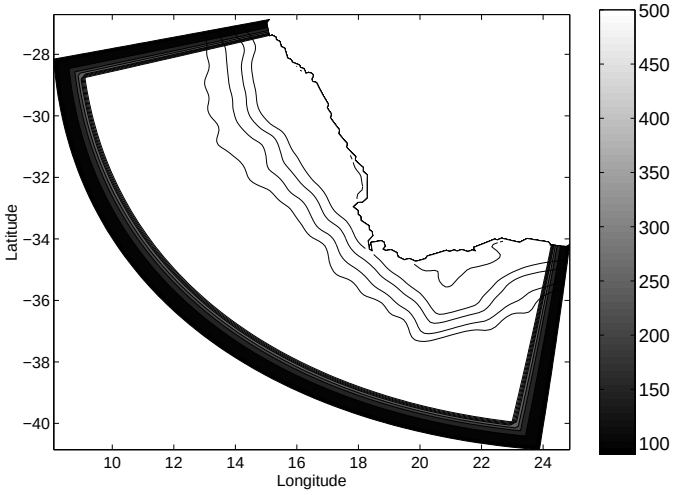

Figure 3.15 Nudging time in days for the high resolution experiment.

This method filters the model solution to connect it to the surrounding smooth oceanic data, while allowing the development of a meaningful internal solution. The relaxation times are chosen empirically to avoid long-term drift and over-specification:

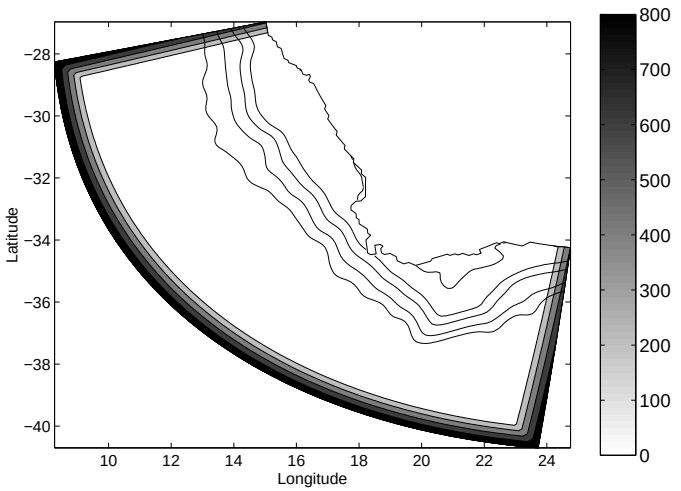

Figure 3.16 Lateral Laplacian mixing coefficient ($m.s^{-2}$) for the high resolution experiment.

- $\tau_{out} = 360$ days for all the variables
- $\tau_{in} = 10$ days for the velocities
- $\tau_{in} = 3$ days for the tracers

Since the boundary values of the free surface elevation does not affect the inner solution on a C-grid, a simple non-gradient scheme is applied for the boundary condition of the free surface elevation.

An important particularity of the regional model of the South African West Coast is the highly energetic Agulhas Current that is flowing into the domain via the Eastern boundary. In the presence of this meandering current, the solution happened to be instable after a year or two of simulations. To obtain a long term stable solution, a specific open boundary scheme has been implemented into the code for the barotropic component of the velocities perpendicular to the boundaries. This scheme was originally proposed by Flather [1976] for a tidal model, and combines a one dimensional radiation equation (3.38) with a one dimensional version of the linearized continuity equation (3.39):

$$\frac{\partial \bar{u}}{\partial t} \pm c\frac{\partial \bar{u}}{\partial x} = 0 \tag{3.38}$$

$$\frac{\partial \zeta}{\partial t} + H\frac{\partial \bar{u}}{\partial x} = 0 \tag{3.39}$$

$$\Rightarrow \frac{\partial \bar{u}}{\partial t} = \pm\frac{c}{H}\frac{\partial \zeta}{\partial t} \tag{3.40}$$

$$\Rightarrow \bar{u}_{bound} = \bar{u}_{data} \pm \frac{c}{H}(\zeta - \zeta_{data}) \tag{3.41}$$

The sign in equation (3.41) depends on the position of the boundary. For the phase velocity, we assumes that the waves approaching the open boundary are mostly non dispersive surface gravity waves. Hence, c in equation (3.41) is fixed at $c = \sqrt{gH}$ (g being the gravity acceleration and H the water column depth). Equation (3.41) becomes;

$$\bar{u}_{bound} = \bar{u}_{data} \pm \sqrt{\frac{g}{H}}(\zeta - \zeta_{data}) \tag{3.42}$$

This open boundary scheme can be seen as a one way nesting scheme that conserves mass. The differences between the specified values ($\bar{u}_{data}$ and ζ_{data}), and those calculated by the model ($\bar{u}$ and ζ) are forced to radiate at the speed of the external gravity waves [*Palma and Matano,* 1998]. Information is constantly provided by the boundary, that could over-determine the inner solution. Nevertheless, if consistent data were provided for the boundary, this scheme gave the best overall performance in test cases conducted using a shallow water model [*Palma and Matano,* 1998]. One should expect that for a realistic simulation, if data of good quality are given for the boundary, this scheme should stabilize the inner solution in comparison to a scheme that allows a more important degree of freedom. This is what it is observed during our simulation. The drawback is that an important control from the boundaries could limit the physical significance of the solution obtained inside the model domain.

(b) Climatology fields

In a first attempt, the initial and boundary conditions have been derived from a global monthly climatology dataset [*Levitus,* 1982]. The sea surface elevation is computed as the dynamic height referenced to the 500 m level. The thermal wind relationship gave the baroclinic velocities. Several problems arose from this derivation:

(1) The solution was dependent of the arbitrary choice of the no-motion reference level.

(2) Extrapolation was necessary to obtain data on the shelf and gave spurious recirculation.

(3) The Agulhas Current was badly represented (see figure 3.13).

Whereas it was possible to obtain a solution by this method, it has been preferred to rely on a seasonal averaged data derived from a z-coordinate, $1/3\ ^o$ resolution, rigid lid, basin scale model of the Indian and South-Atlantic Oceans [*Biastoch and Krauß,* 1999]. This model is currently implemented at the Oceanographic Department of the University of Cape Town. The rigid lid assumption made in this model forces us to diagnose a free surface elevation from the other variables. This seasonal data gives an annual cyclic information for each model variable (e.g. u, v, $\bar{u}$, $\bar{v}$, T, S, ζ). To avoid discontinuities in the climatology (and forcing) fields, ROMS linearly interpolates in time the data to obtain a field at each model time.

The summer values of the climatology (e.g. 15 February) are used for the initial conditions. For the model spin-up, it has been preferred to let the model adjust itself from rest on the density field associated with the temperature and salinity. The variables u, v, $\bar{u}$, $\bar{v}$ and ζ are set to zero a t=0. The circulation has to adjust to the stratification, the domain geometry, the surface and the lateral forcings. Because the domain is relatively small, this should occur relatively quickly, and we expect to obtain an equilibrium state after a few years of simulation.

3.4 Results for the low resolution model

3.4.1 Spin-up

As explained by Penduff [1998], several mechanisms rapidly adjust the solution to the initial stratification, and the different forcing. After 1 day, the sea surface elevation shows the

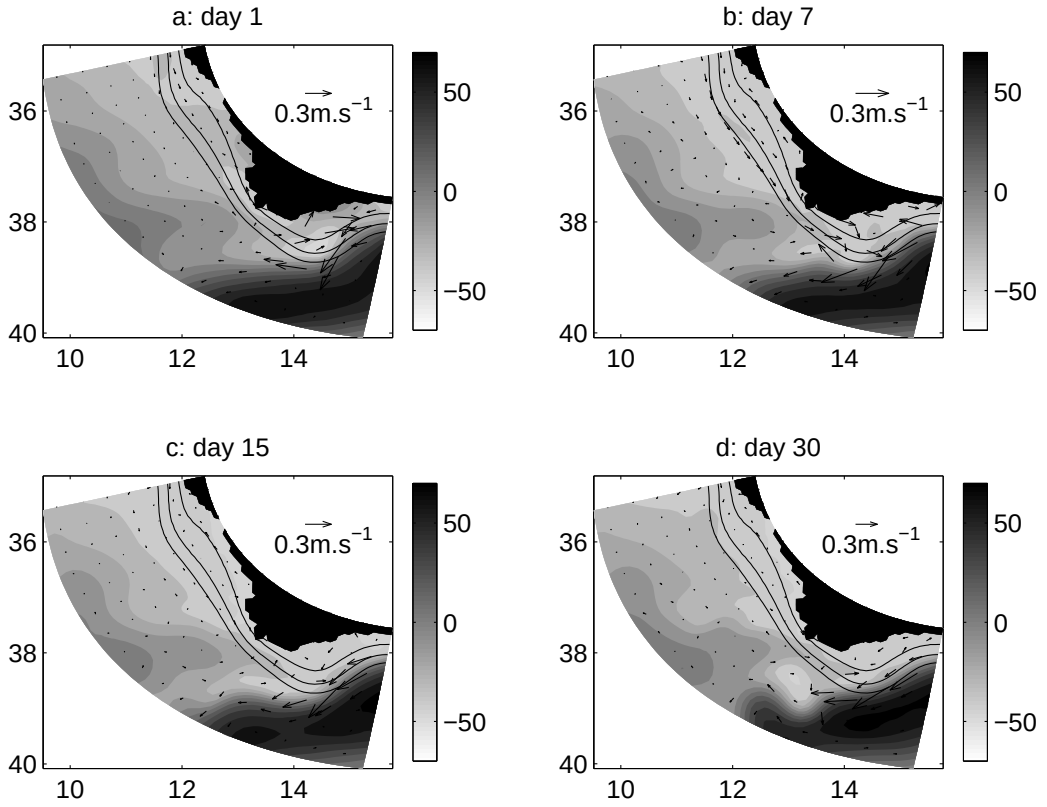

Figure 3.17 Sea surface height and barotropic currents for the low resolution experiment. a: after 1 day of simulation. b: after 1 week. c: after 2 weeks. d: after 1 month. The greyscale range represents the sea surface elevation in centimeters. 1 current vector is portrayed every 4 vectors.

geostrophic adjustment to the initial stratification (figure 3.17-a), . From the Northern boundary, a signal of low elevation (associated with the upwelling) propagates along the West Coast to the South as a coastal trapped wave (figures 3.17-a, 3.17-b and 3.17-c), and connects with locally forced low sea surface elevation around Cape Peninsula. The adjustment processes induce relatively strong barotropic velocities on the Agulhas Bank (figures 3.17-a and 3.17-b). After 15 days, the velocities are weaker on the shelf and slope (figure 3.17-c), and a ring detaches from the Agulhas Current.

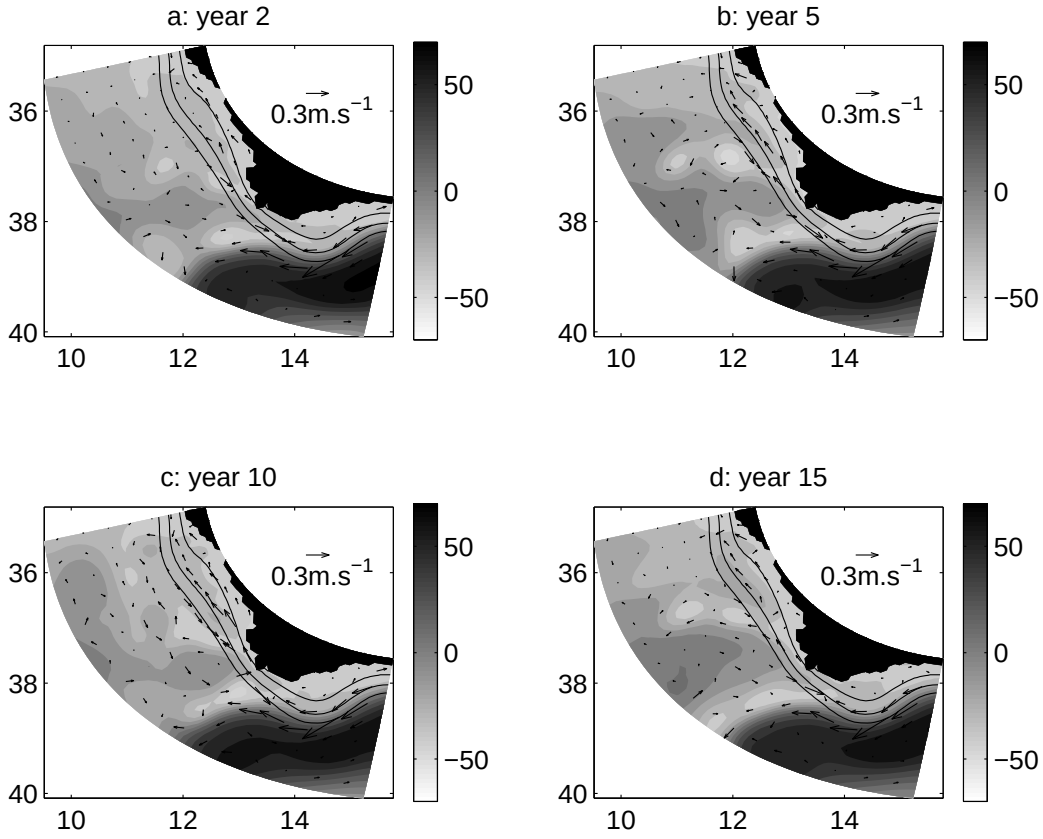

Figure 3.18 Sea surface height and barotropic currents for the low resolution experiment. a: 3 January of model year 2. b: 3 January of model year 5. c: 3 January of model year 10. d: 3 January of model year 15. The greyscale range represents the sea surface elevation in centimeters. 1 current vector is portrayed every 4 vectors.

Though the model resolution is coarse (ranging from 18 km to 31 km), mesoscale activity is able to develop during the simulation. On figure (3.18), the sea surface elevation and the barotropic currents have been portrayed for 3 January of model year 2 (figure 3.18-a), model year 5 (figure 3.18-b), model year 10 (figure 3.18-c), and model year 15(figure 3.18-d). After 1 year of simulation (figure 3.18-a), the solution appears to be adjusted. Regardless of the mesoscale activity, very few differences occur in the following years. Cyclonic eddies appears to be shed from the Agulhas Bank and from the Cape Point / Cape Columbine area. Though very close to the open boundary, from time to time an anticyclonic eddy detaches from the Agulhas Current at the Agulhas retroflection (figure 3.18-b). The adjustment process can be seen on a graph of the domain averaged norm of ζ: $\sqrt{\frac{1}{S}\iint_S \zeta^2 ds}$ (figure: 3.19). The model "forgets" quasi immediately the shock of the start from rest. A low pass filtering with a

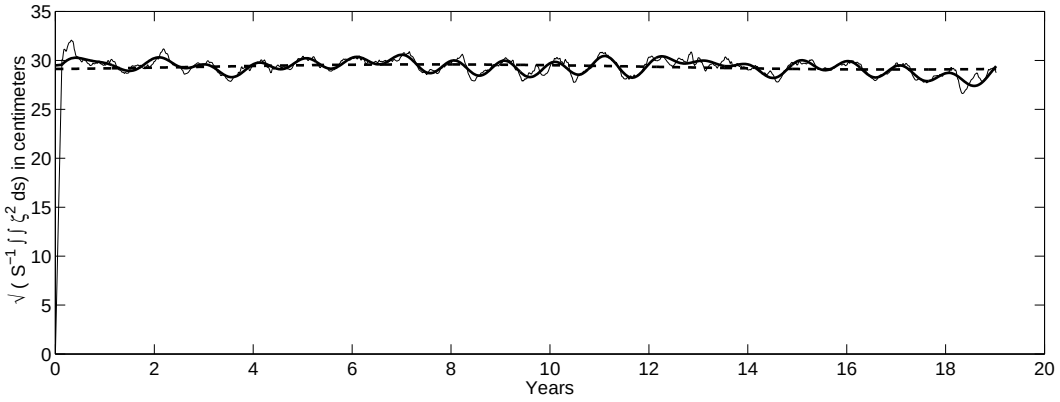

Figure 3.19 Root mean square of the sea surface elevation over the domain The thick line represents the data after a low pass filter with a cutoff at 1 year.

cut-off at 1 year is applied to the data (thick line on figure 3.19) to show the seasonal and interannual variability. No significant long term trend is observed after the first adjustment of the sea surface elevation.

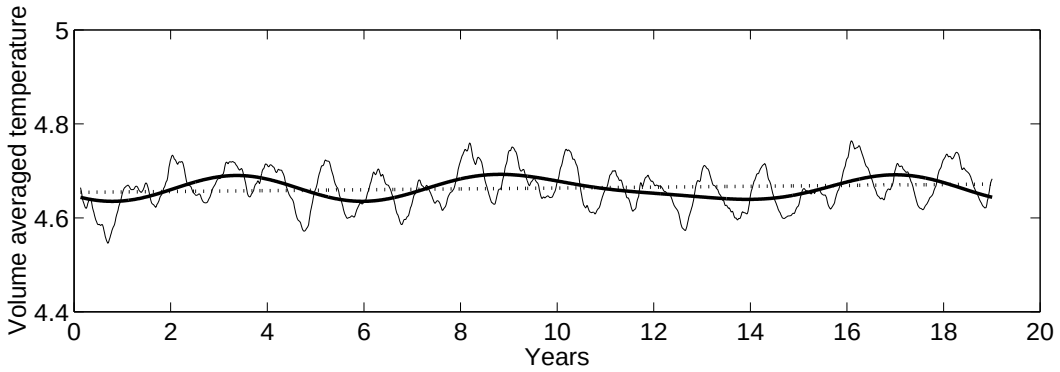

Figure 3.20 Volume averaged potential temperature (^{o} C)for the low resolution experiment as a function of time.The thick line represents the data filtered by a low pass filter with a cut off at 4 years. The dotted line represents the trend of the data.

After the quick adjustment to the initial values, the slow response of the stratification occurs. These long term processes consist of the propagation of baroclinic waves, advection and mixing. The presence of the Agulhas Current associated with strong velocities accelerates the adjustment process. Because the domain is relatively small, it takes a relatively short time for a baroclinic wave or an advected water particle to cross it. An important measure of model fidelity is the degree to which it is able to preserve the globally averaged values of its tracer fields. The volume averaged temperature time series shows a strong seasonal pattern (figure 3.20). After 2-3 years it oscillates around a mean of approximately 4.65^o C. No significant trend is noticeable. But the solution exhibits variations on the interannual scale. This variability is quite surprising. It can be related to the presence of the Agulhas Current that produces, on an irregular basis, large eddies in comparison with the size of the domain. Interannual variability is also a characteristic pattern observed in the time series of the domain averaged salinity (figure 3.21). Freshening occurs during the 5 first years, in a range of 0.002 PSU. As the surface forcing didn't operate correctly during this simulation, a

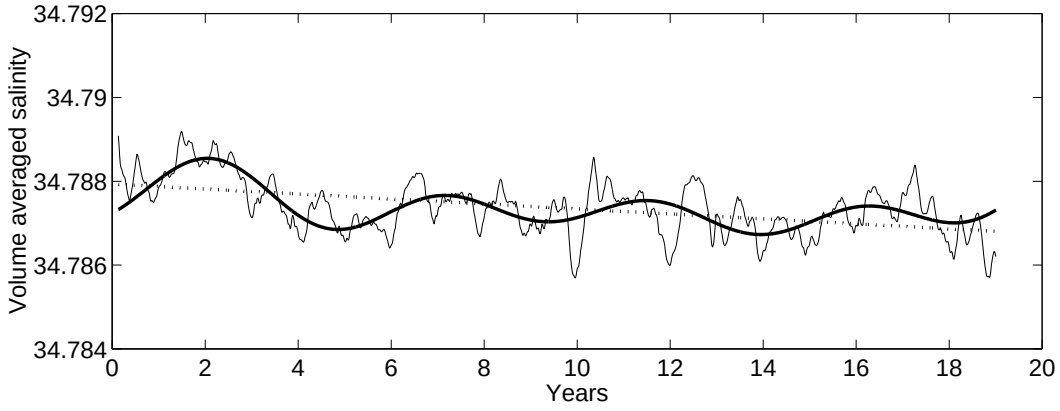

Figure 3.21 Volume averaged salinity (PSU) for the low resolution experiment as a function of time. The thick line represents the data filtered by a low pass filter with a cut off at 4 years. The dotted line represents the trend of the data..

trend should have been noticed in the volume averaged salinity. The weakness of the observed trend emphasises an important constraint of the open boundaries on the solution. Tests should be conducted with less restrictive open boundary nesting values.

Time series of the volume averaged kinetic energy and of the averaged surface kinetic energy are shown on figure (3.22-top) and figure (3.22-bottom) respectively. During the first months of the simulation, the volume averaged kinetic energy rises rapidly to reach an averaged value of about 90 $cm^2.s^{-2}$. Little temporal trend is apparent in the time series. The seasonal pattern is not really dominant in the volume averaged kinetic energy. On the contrary, the surface kinetic energy shows the marked ocean response to the seasonal varying surface forcing. The absence of a significant trend is a sign of correct behavior of the solution. As expected, the surface averaged kinetic energy has a maximum during the upwelling season.

3.4.2 Time average

The outputs of the low resolution experiment have been time averaged from model year 3 to model year 10 in order to obtain a smooth 3-dimentional field of the mean circulation resolved by the model.

For the low resolution experiment, the averaged sea surface temperature is close to the surface climatology employed for the heat forcing of the model (figure 3.23-a). Upwelling is relatively homogeneous with 14^oC waters all along the west coast from Cape Peninsula to the northern boundary. The isotherms tend to move away from the coast North of 30^o S, but the northern boundary constrains them back towards the coast north of 29^o S. The Agulhas current is characterized by a tongue of warm water ($> 20^oC$) that rounds the Agulhas Bank, enclosing colder surface water onto the bank. The presence of the Subtropical front is noticeable in the South Corner of the model domain. It shows a marked sea surface temperature gradient ranging form 13^oC to 17^oC in a short distance. The Agulhas Current does not retroflect properly in this experiment (figure 3.23-b). When it flows along the Agulhas Bank, it reaches on average a maximum velocity of 1.1 $m.s^{-1}$, which is a realistic value. Because the topography is smooth, the current does not detach from the southern tip of the Agulhas Bank, and rounds the bank to flow in a North-east direction. This behavior is not observed

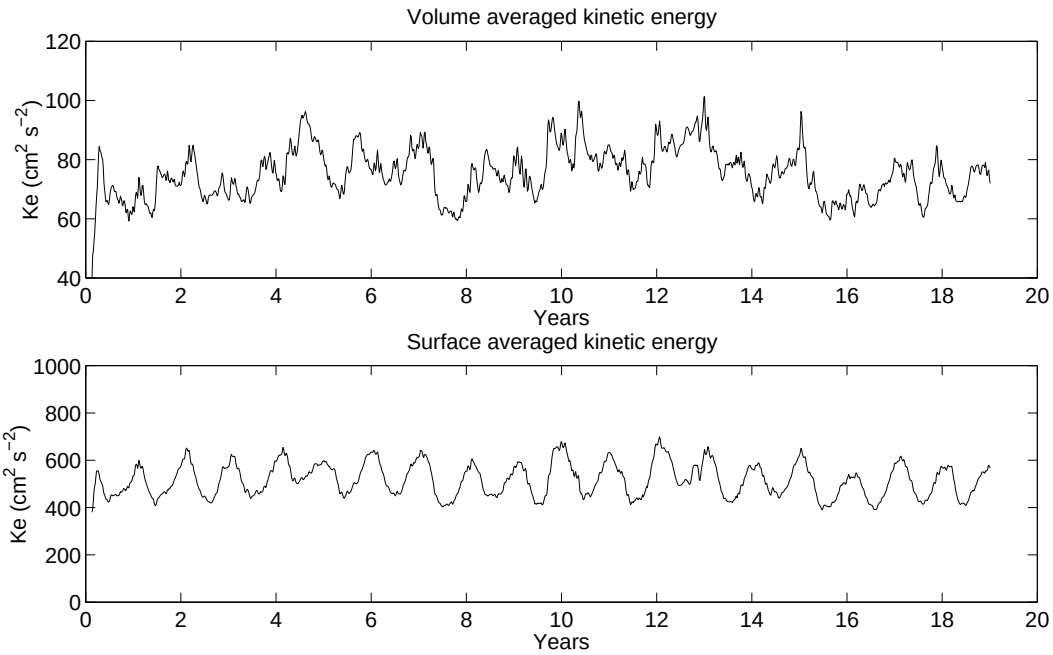

Figure 3.22 Top: Volume averaged kinetic energy ($cm^2.s^{-2}$) for the low resolution experiment. Bottom: Surface kinetic energy ($cm^2.s^{-2}$) for the low resolution experiment.

in nature. As a consequence, the retroflexion area is displaced westward close to the offshore boundary. On the Agulhas Bank, currents are weak as pointed by Boyd and Oberlholster [1994]. The Good Hope jet is not present on the western part of the bank. Along the west coast, the north westward surface current flows continuously towards the equator with characteristic velocities of about 30 $cm.s^{-1}$. Divergence is evident offshore of Cape Columbine (17^o E - 33^o S), in agreement with the schematic representations of Boyd and Shillington [1994] (figure 1.8) and Shannon [1985] (figure 1.13). The Subtropical front is well represented by the surface salinity (figure 3.23-c) with values ranging from 34.6 PSU to 35 PSU in the South corner of the model domain. The effect of the zero surface salinity flux is visible near the northern boundary where the solution has departed from the climatology forcing values and is restored back in the vicinity of the boundary. Nevertheless, the averaged surface salinity values remain close (in a range of $0.1 \sim 0.2$ PSU) to the Levitus [1982] climatology data. The Agulhas Current does not have a marked signature in surface salinity. On the contrary, it dominates the averaged sea surface elevation signal 3.23-d). In the few kilometers between the Agulhas Bank and the southern part of the Agulhas Current, the averaged sea surface elevation ranges from -30 cm to 60 cm (figure 3.23-d). Along the west coast, the variations in sea surface height are very small ($\sim$ 10cm).

The horizontal averaged currents have been portrayed for z = -100 m (figure 3.24-a), z = -500 m (figure 3.24-b), z = -1000 m (figure 3.24-c), and z = -2000 m (figure 3.24-d). The Agulhas current is present on the 3 first levels. Its magnitude diminishes smoothly with depth. For z=-100 m (figure 3.24-a), a narrow coastal jet with velocities of 30 $cm.s^{-1}$ flows past Cape Peninsula towards the equator. Between this jet and the coast, the equatorward flow is weak. For z=-500 m (figure 3.24-b), poleward motion is present along the topography North of 32^o S. Between Cape Peninsula and 32^o S equatorward motion is still present. Below 500 m weak poleward motion is present North of 36^o S (figures 3.24-c and 3.24-d) as described by Nelson [1989].

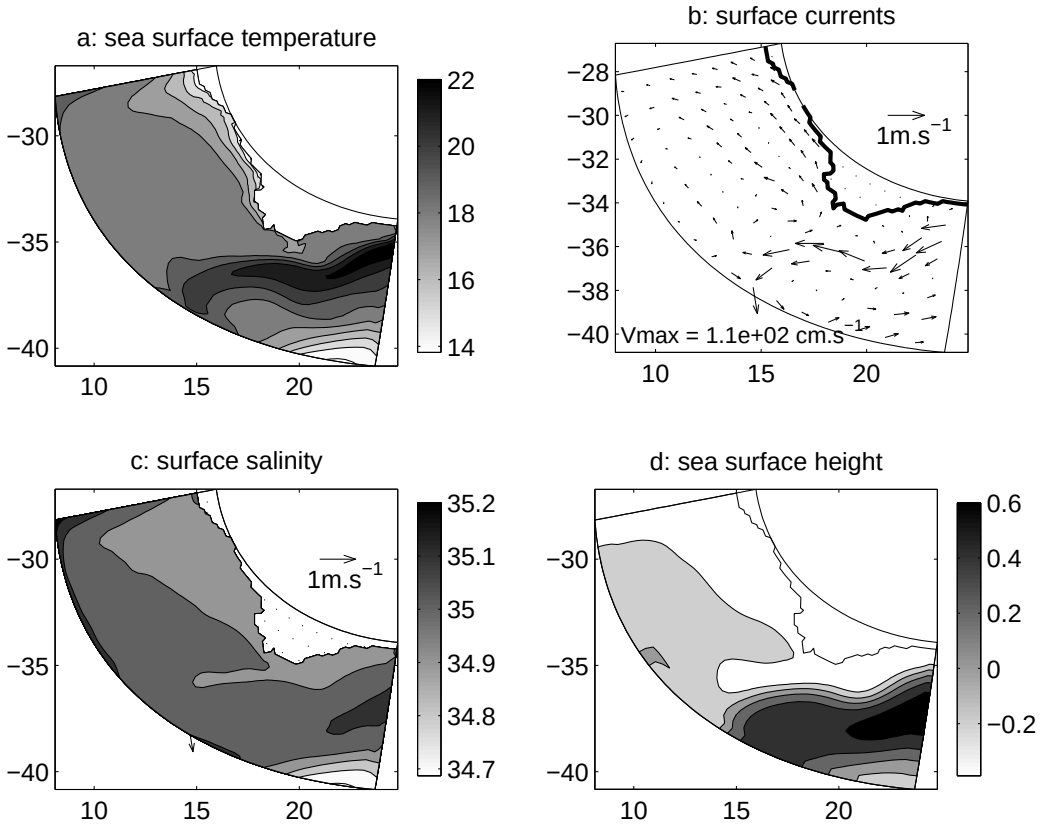

Figure 3.23 Annual surface climatology derived from the results of the low resolution experiment. a: sea surface temperature (^{o}C). b: surface currents (m.s^{-1}), Vmax is the maximum velocity, 1 vector is portrayed every 4 vectors. c: sea surface salinity (PSU). d: sea surface height (m). The horizontal coordinates account for the longitude and the latitude.

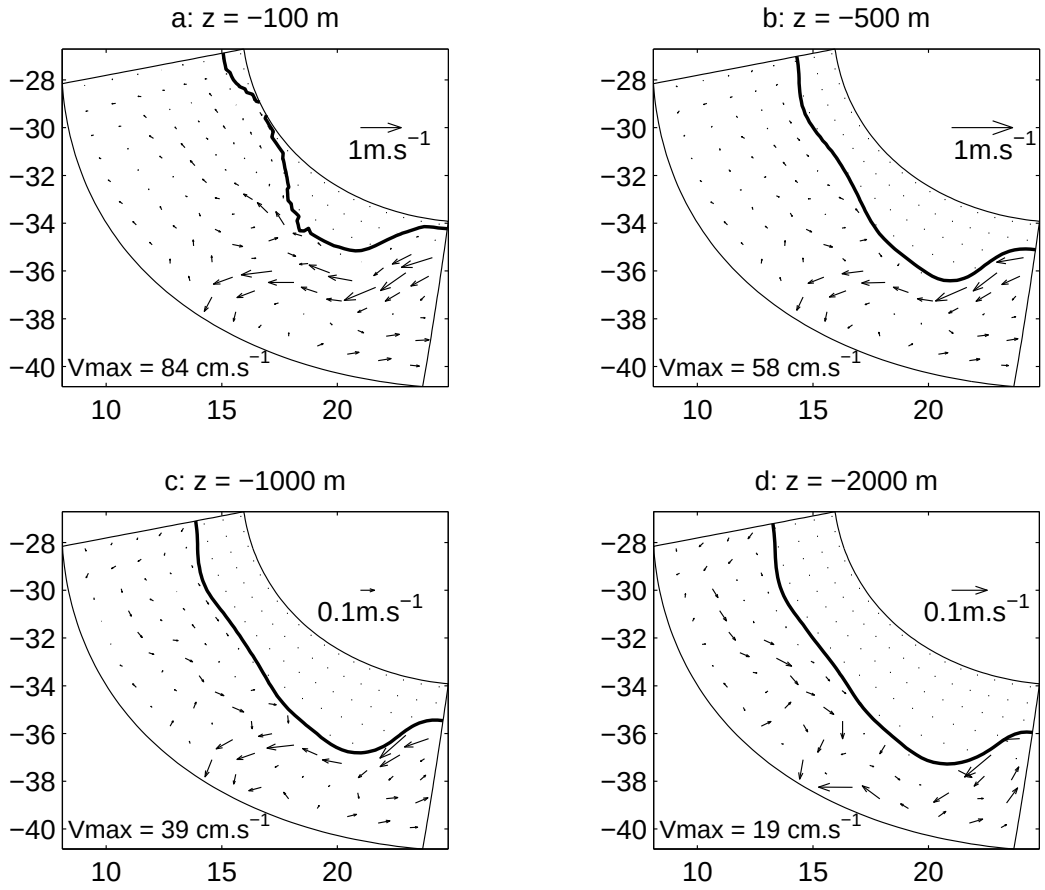

Figure 3.24 Averaged currents in m.s^{-1} for the low resolution experiment. a: for $z = -100$ m, b: for $z = -500$ m, c: for $z = -1000$ m, and d: for $z = -2000$ m. The maximum velocity is given for each level. One vector is represented every 4 vectors. The horizontal coordinates account for the longitude and the latitude.

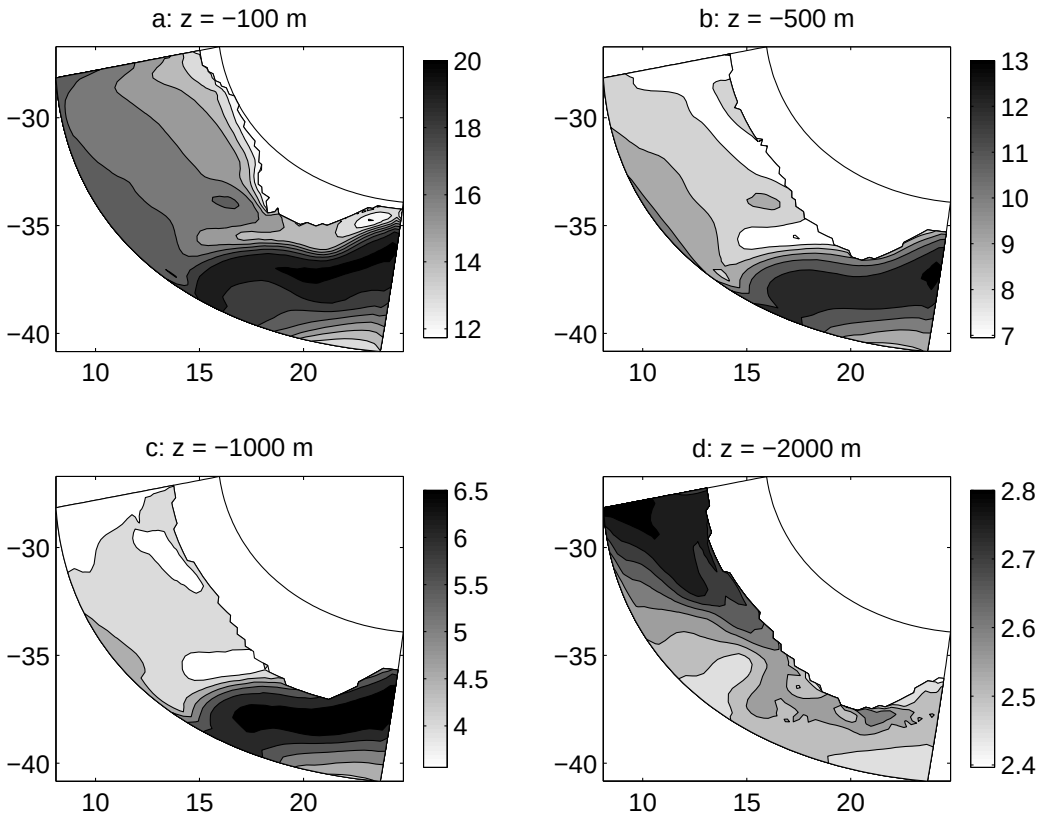

Figure 3.25 Potential temperature annual climatology (°C) for the low resolution experiment. a: for $z = -100$ m, b: for $z = -500$ m, c: for $z = -1000$ m, and d: for $z = -2000$ m. The horizontal coordinates account for the longitude and the latitude.

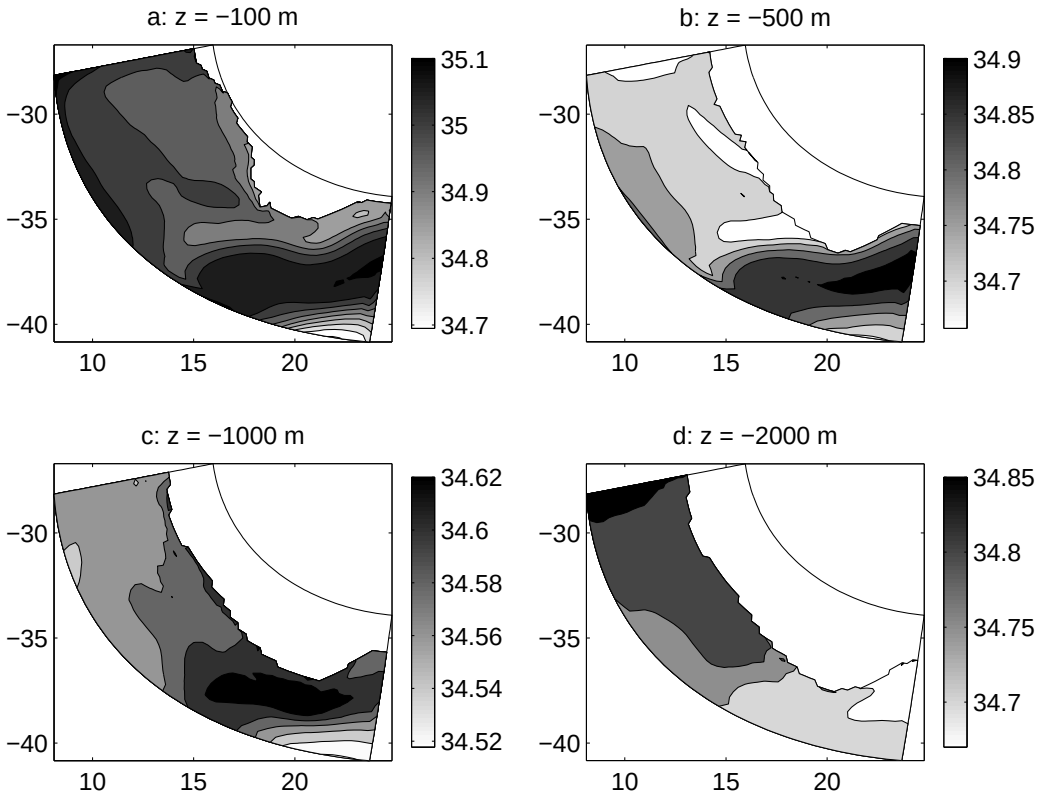

Figure 3.26 Salinity annual climatology (PSU) for the low resolution experiment. a: for $z = -100$ m, b: for $z = -500$ m, c: for $z = -1000$ m, and d: for $z = -2000$ m. The horizontal coordinates account for the longitude and the latitude.

The potential temperature and the salinity have been also portrayed for the 4 horizontal levels defined previously (figures 3.25 and 3.26). The upwelling signal all along the west coast is present for z=-100m with a minimum in temperature (12^o C, figure 3.25-a) and a minimum in salinity (34.7 PSU, figure 3.26-a). This minimum in salinity is caused by the presence of the Antarctic Intermediate Water (AAIW), characteristic of the South-East Atlantic Ocean, with its core of minimum of salinity around 700-800 m (see section 1.2). This minimum of salinity can diminish the density gradient induced by the upwelling in comparison to the other upwelling systems. This is a particularity of the Benguela. The impact of this salinity minimum on the dynamics of the upwelling system still have to be quantified. On the eastern side of the Agulhas Bank, for z = -100 m, a local minimum in temperature stands at the offshore limit of the shelf. It can be the signature of the subsurface cool-water feature described by Boyd and Shillington [1994]. For z = -100 m, -500 m, and -1000 m, the Agulhas Current is recognizable by a maximum both in salinity and temperature. At these levels, a zonal tongue of local minimum of temperature and salinity extends from the Agulhas Bank at 35^o S. An averaged cyclonic circulation of the surface currents (visible also in the sea surface elevation) is associated to this structure. It might be related to upwelled waters transported offshore by mesoscale eddies shed from the Agulhas Bank-Cape Peninsula area. For z = -2000 m, an equatorward increase of potential temperature of 0.4^o C (figure 3.25-d) and for salinity of 0.15 PSU (figure 3.26-d) over the length of the domain is visible. This shows a transition from Antarctic Intermediate Water to North Atlantic Deep Waters (see the TS-diagram 1.4).

Although the results of the low resolution experiment show interesting features that can be related to observations, some aspects of the solution, like the Agulhas Current retroflection or the coastal circulation, are not well represented at this level of resolution. The bottom topography appears to have an important control of the flow and need to be treated more accurately. Hence, a new set of experiments is conducted by doubling the horizontal number of grid points in each direction. Nevertheless, the low resolution configuration is a useful tool that provides a reference solution to compare with new results and that can be used to test new numerical schemes or parameterizations at a reasonable computer cpu time.

3.5 Results for the high resolution model

Keeping the same surface and lateral boundary forcing of the previous experiment, a new configuration has been set up using an horizontal grid with an accuracy ranging from 9 km at the coast to 16 km offshore. This configuration should resolve most of the mesoscale features observed along the southwestern coast of Africa. The criterion for the error in the pressure gradient allows the use of a less smoothed bottom topography (figure 3.7). Because the bathymetry is of primary importance in the control of the shelf and slopes dynamics, the behavior of the solution in this configuration should be more satisfactory.

In a first step, the effects of the s-coordinate related pressure gradient error are tested in an experiment with no forcing and no horizontal variations in density. Four walls are placed at the lateral boundaries of the domain. The vertical structures in temperature and salinity are defined analytically at the model initialization to account for the horizontally spatial average of the vertical density structure. During this test, no horizontal or vertical mixing is present, to concentrate on the effects of the pressure gradient. Because there is no forcing and no horizontal variations in density, the pressure gradient should remain equal zero during all the simulation. If currents are generated, they are spurious circulations induced by errors in computing the pressure gradient. The spurious circulation should be maximum in the bottom s-level, where the slopes in the s coordinates are the highest. As explained in section (3.2.4),

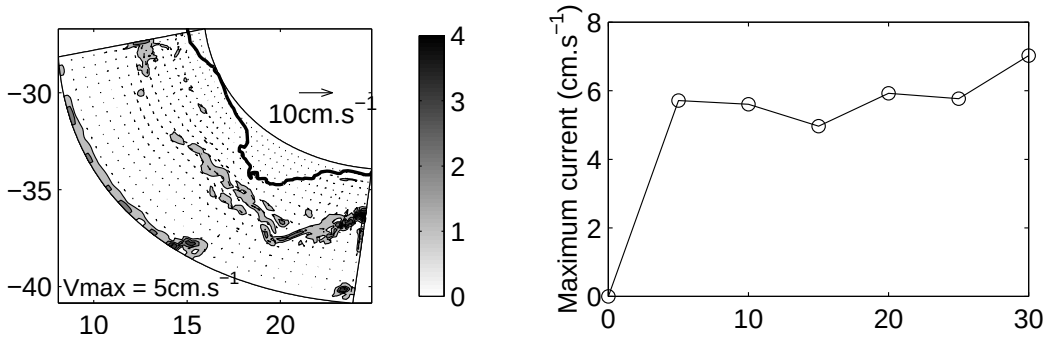

Figure 3.27 Left panel: bottom layer currents ($cm.s^{-1}$) after 1 month for the sigma coordinate test case in high resolution. The greyscale range represents the total velocity in $cm.s^{-1}$. The isolines interval is 1 $cm.s^{-1}$.The horizontal coordinates account for the longitude and the latitude. Right panel: maximum current ($cm.s^{-1}$) over all the domain as a function of time in days.

the s-coordinate related pressure gradient error comes from the discretization of the pressure gradient in the s-coordinate system. If the density field and the s-coordinate system do not vary with time, the error in the pressure gradient should remain constant for this test case (the s-coordinate is dependent of the free surface elevation but this only significantly affects the surface layers). Because only the Coriolis and pressure gradient terms are solved during the test simulation, the spurious currents should reach rapidly a geostrophic equilibrium with the error in the pressure gradient. Hence, after a spin-up of a few days, the averaged spurious currents should not increase with time. It is then sufficient to run the test experiment for only a month to obtain a significant representation of the impact of the pressure gradient error on the circulation. During the test experiment, the maximum spurious currents reach a plateau of about 6 $cm.s^{-1}$ after 5 days (figure 3.27-right). It is a large value but looking at the horizontal currents of the s-bottom level after 1 month of simulation (figure 3.27-left), one might note that this largest currents are along the domain wall (that are open boundaries in the realistic experiment). Hence, these currents are not directly forced by errors in the pressure gradient, but are part of the general circulation generated to compensate the slow motion induced by the pressure gradient errors. At distance from the walls, the bottom spurious currents are of the order of 1 $cm.s^{-1}$ with a maximum of 2 $cm.s^{-1}$ South of the Agulhas Bank (figure 3.27-left). The pressure-gradient-error-related-currents are portrayed after 1 month of simulation at 4 horizontal levels: z = -100 m (figure 3.28-a), z = -500 m (figure 3.28-b), z = -1000 m (figure 3.28-c), and z = -2000 m (figure 3.28-d). At each level, the error results in a poleward along-slope current of around 1 to 2 $cm.s^{-1}$. The current is locally stronger ($\sim$ 5 $cm.s^{-1}$) at the southern tip of the Agulhas Bank for z = -1000 m. If we compare the error induced currents to the time averaged currents of the high resolution realistic experiment (figure 3.33), we can note that the relative error is of approximately 5 % for z = -100 m, 10 % for z = -500 m , and 20 % for z = -1000 m and z = -2000 m. These values are not small for the deep layers. A part of the solution can be induced by errors in the pressure gradient. This might be the case for the deep poleward motion observed in figure (3.33-d) and for the poleward undercurrent observed on figure (3.45-b). One can note firstly that the values obtained for these 2 currents corresponds to observation [*Nelson,* 1989]. Secondly the residual pressure gradient related current obtained in the test case are of the same order of magnitude of the error made in the measurements. Thirdly, the current pathway observed on figure (3.33-d) is

not the same as the pathway followed by the error related current seen in figure (3.28-d).

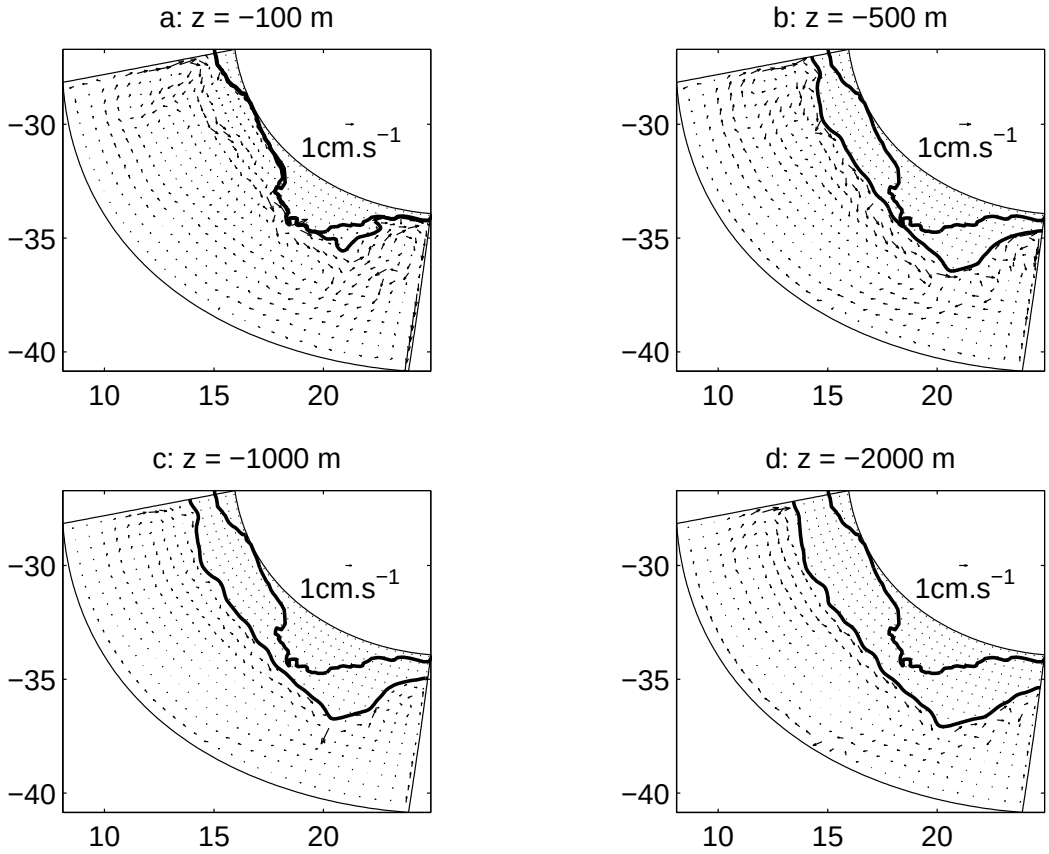

Figure 3.28 Horizontal currents in cm.s^{-1} after 1 month for the test of the pressure gradient error. a: for $z = -100$ m, b: for $z = -500$ m, c: for $z = -1000$ m, and d: for $z = -2000$ m. One vector is represented every 4 vectors. The horizontal coordinates account for the longitude and the latitude.

The realistic simulation in high resolution has been conducted for 10 years. The data for the different modelized variables have been stored in an output file every 2 simulated days. This way, analysis of the model outputs are conducted with a high level of spatial and temporal accuracy. These data are also employed to force an individual based model developed at the University of Cape Town to study the behavior of the eggs, larvae, and juveniles of sardines and anchovies around the south and west coast of Africa. Like for the low resolution experiment, the spin up for the high resolution experiment occurs quickly. After 1 year of simulation, the solution appears to be already adjusted to the different forcing. A high level of mesoscale activity develops during the simulation, activity characterized by the generation of Agulhas rings from the Agulhas Current retroflection area, the shedding of cyclonic eddies form the southern tip of the Agulhas Bank, Cape Peninsula, and Cape Columbine. The upwelling front shows also an important variability, developing a series of meanders, plumes and filaments in a realistic manner. In the following sections, an analysis of the averaged behavior of the model solution and variability as well as comparisons with observations validate the simulation.

As for the low resolution experiment, time series are shown of the volume averaged potential temperature and salinity are portrayed respectively on figure (3.29) and on figure (3.30).

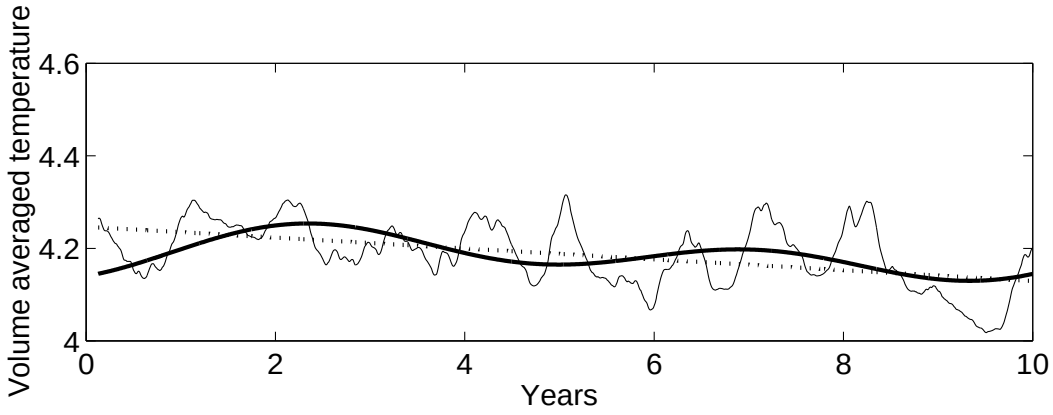

Figure 3.29 Volume averaged potential temperature (^{o}C) for the high resolution experiment as a function of time in years.The thick line represents the data filtered by a low pass filter with a cut off at 4 years. The dotted line represents the trend of the data.

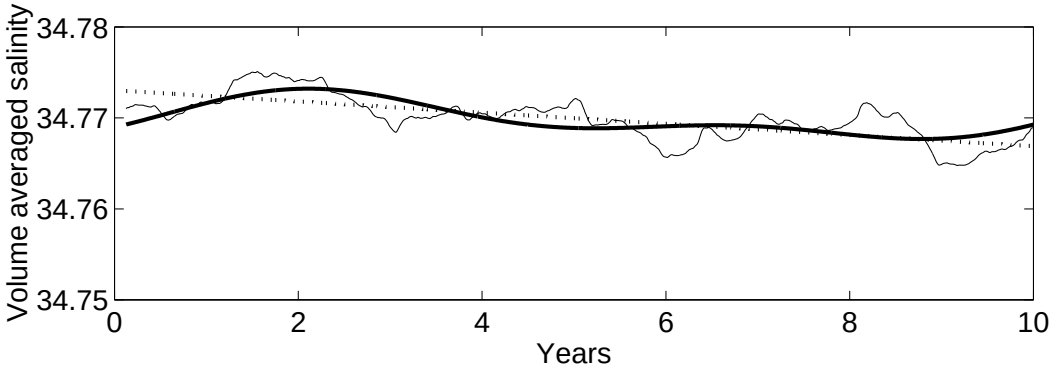

Figure 3.30 Volume averaged salinity (PSU) for the high resolution experiment as a function of time in years. The thick line represents the data filtered by a low pass filter with a cut off at 4 years. The dotted line represents the trend of the data.

The spin up appears to be as quick as for the low resolution experiment. The volume averaged temperature shows seasonal variations and a trend of -0.1^{o}C in 10 years (figure 3.29). A surprising result is the trend observed in the time series of the volume averaged salinity, 10 times greater than for the low resolution experiment (nevertheless it is still small). This exhibits the weaker influence of the open boundaries on the inner solution. Two important events are visible as minimums both in the temperature and salinity time series, at year 6 and after year 9. These minimums correspond to a bifurcation in the pathway of the Agulhas Current associated with a large cyclonic eddy perturbing the solution close to the Agulhas Bank. During the two events, the retroflection area has moved towards the eastern boundary of the domain. These variations in the position of the retroflection of the Agulhas Current have been observed in nature.

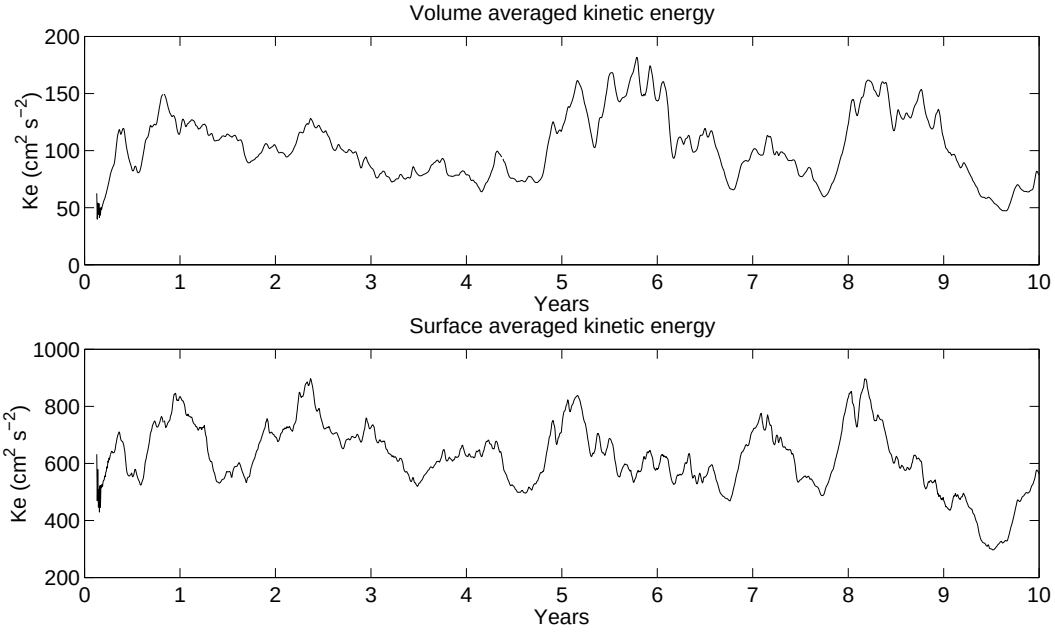

Figure 3.31 Top: Volume averaged kinetic energy (cm^2.s^{-2}) for the high resolution experiment. Bottom: Surface kinetic energy (cm^2.s^{-2}) for the high resolution experiment.

Because smaller structures are resolved in the high resolution experiment, the volume averaged kinetic energy has increased from a mean value of 70 cm^2.s^{-2} to 100 cm^2.s^{-2} with increasing resolution (figure 3.31-top). The 2 events described previously are also visible as maximums in kinetic energy from year 5 to year 6 and from year 8 to year 9. The seasonal pattern in the mean surface kinetic energy is less marked than for the low resolution experiment. This reveals that more intrinsic instability processes, not directly forced by the wind, are now resolved during the high resolution experiment (figure 3.31-bottom). The mean level of surface kinetic energy is also greater (600 cm^2.s^{-2}) in the high resolution experiment than for the low resolution experiment (500 cm^2.s^{-2}).

3.5.1 Time averaged variables

By taking the average in time of the different model variables from year 3 to year 10, it has been possible to verify the improvement of the model solution when the resolution has been increased.

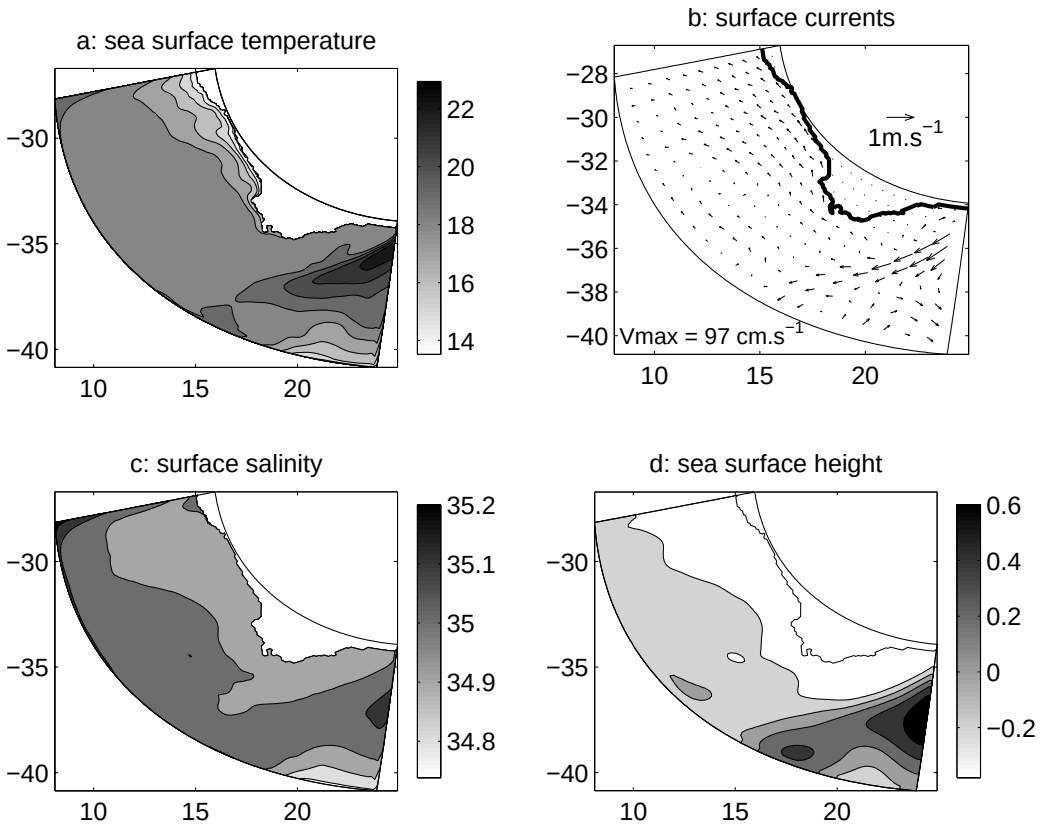

Figure 3.32 Annual surface climatology derived from the results of the high resolution experiment. a: sea surface temperature (^{o}C). b: surface currents (m.s^{-1}), Vmax is the maximum velocity, 1 vector is portrayed every 4 vectors. c: sea surface salinity (PSU). d: sea surface height (m). The horizontal coordinates account for the longitude and the latitude.

For the sea surface temperature (figure 3.32-a), the pathway of the sea surface temperature signature Agulhas Current differs slightly from the low resolution experiment. It no longer rounds the Southern limit of the Agulhas Bank in an unrealistic way. The averaged position of the retroflection area is visible in the image of averaged surface current and sea surface elevation (figures 3.32-b and 3.32-d). Some wave like meanders in the upwelling front along the west coast are noticeable in figure (3.32-a), and a jet that follows the shelf edge is present between the southern tip of the Agulhas Bank and Cape Peninsula (figure 3.32-b) as observed in ADCP current measurements [*Boyd and Oberholster,* 1994]. These specific features of the coastal dynamics of the west coast are subject to a more detailed analysis further in the manuscript. Few differences are noticeable between the low and high resolution experiments for the averaged sea surface salinity (figure 3.32-c).

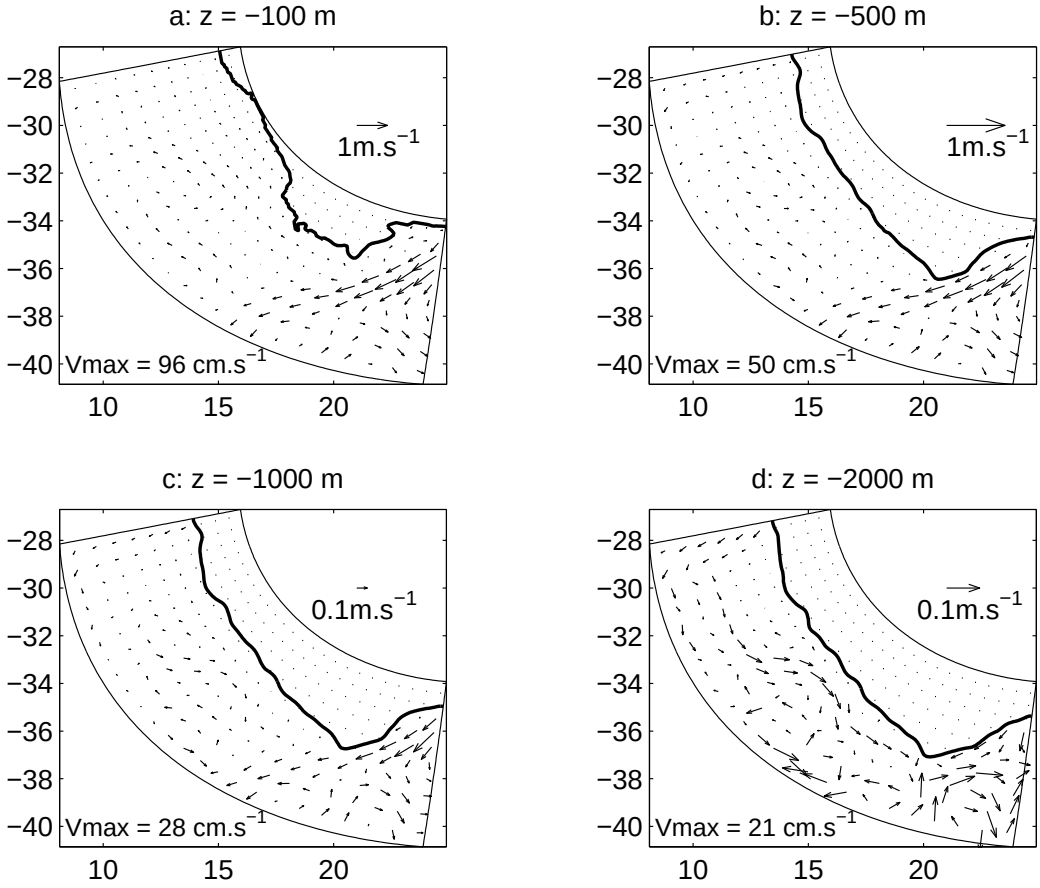

Figure 3.33 Averaged currents in m.s^{-1} for the high resolution experiment. a: for $z = -100$ m, b: for $z = -500$ m, c: for $z = -1000$ m, and d: for $z = -2000$ m. The maximum velocity is given for each level. One vector is represented every 6 vectors. The horizontal coordinates account for the longitude and the latitude.

The time averaged horizontal currents are portrayed for z = -100 m, -500 m, -1000 m, and -2000 m (figure 3.33). The Agulhas Current and the retroflection are present in the 3 first levels. At these 3 levels an anticyclonic recirculation is noticeable where the Agulhas Current encounter the western open boundary. This might be related to an average position for the Agulhas Rings that are shed from the Agulhas retroflection throughout the simulation. Coastal currents along the west coast are equatorward for z = -100 m. For the lowers levels,

the currents along the topography appears to be very weak. In the wide area between the coast and the offshore open boundary the eastern limb of the South Atlantic subtropical gyre manifest itself by a meandering equatorward mean current visible for z = -100 m and z = -500 m. At deeper levels, current in this area appears to be more convoluted and a mean offshore poleward flow is present for z = -2000 m, as in the low resolution experiment.

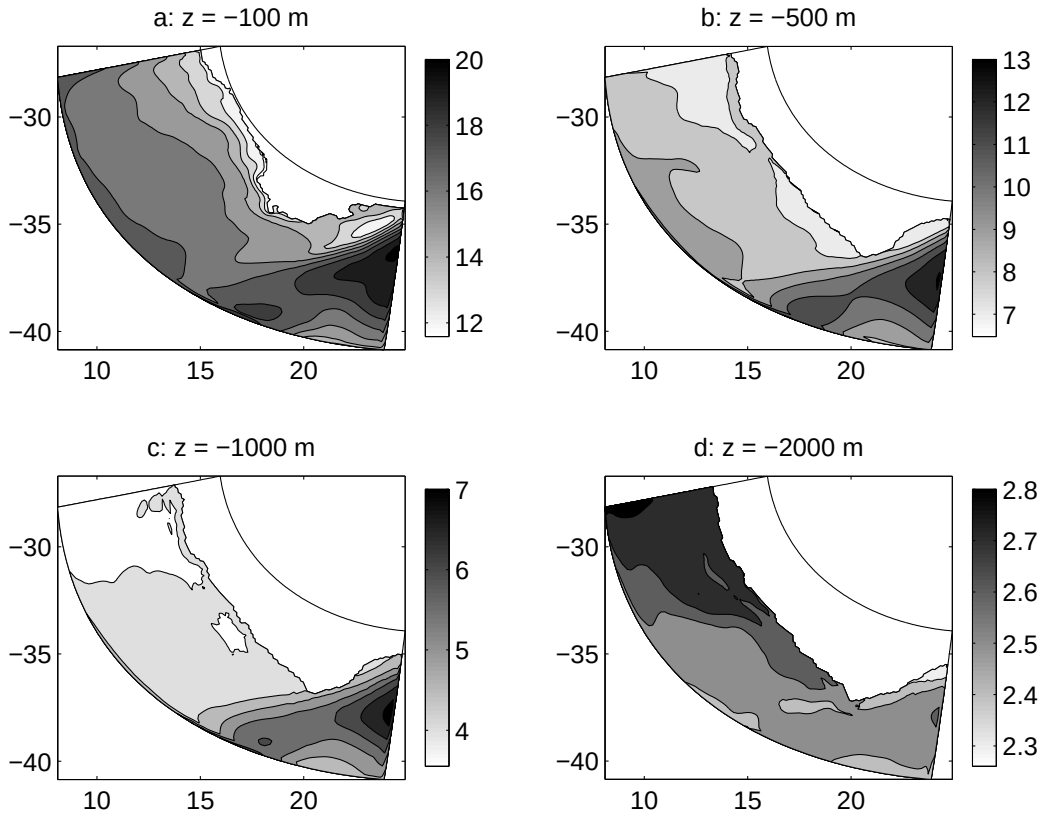

Figure 3.34 Potential temperature annual climatology (^{o}C) for the high resolution experiment. a: for $z = -100$ m, b: for $z = -500$ m, c: for $z = -1000$ m, and d: for $z = -2000$ m. The horizontal coordinates account for the longitude and the latitude.

On the large scale, few differences appear in the comparison between the low and high resolution experiments for the average potential temperature (figures 3.25 and 3.34) and the average salinity (figures 3.26 and 3.35). For the high resolution experiment, the retroflection of the Agulhas Current is visible for temperature and salinity for z = -100 m, -500 m, and -1000 m. The low temperature and salinity tongue, described in section (3.4.2) extending from the Agulhas Bank is no longer present for z= - 500 m and -1000 m. This feature should be related to the smoothed topography of the low resolution experiment. For z = -100 m the subsurface cool water feature on the eastern part of the Agulhas Bank described previously is more marked in this simulation (figure 3.34-a) and can be seen also in salinity. For z = -500 m, a narrow band of warmer water of unknown origin is present along the shelf edge in the northern part of the domain.

If we note $< \bar{u} >$, $< \bar{v} >$ and $< \zeta >$ the time averaged barotropic velocities and free surface elevation, and if we remark that the free surface elevation is small compare to the depth of the ocean depth H, the time averaged vertical integrated equation of continuity

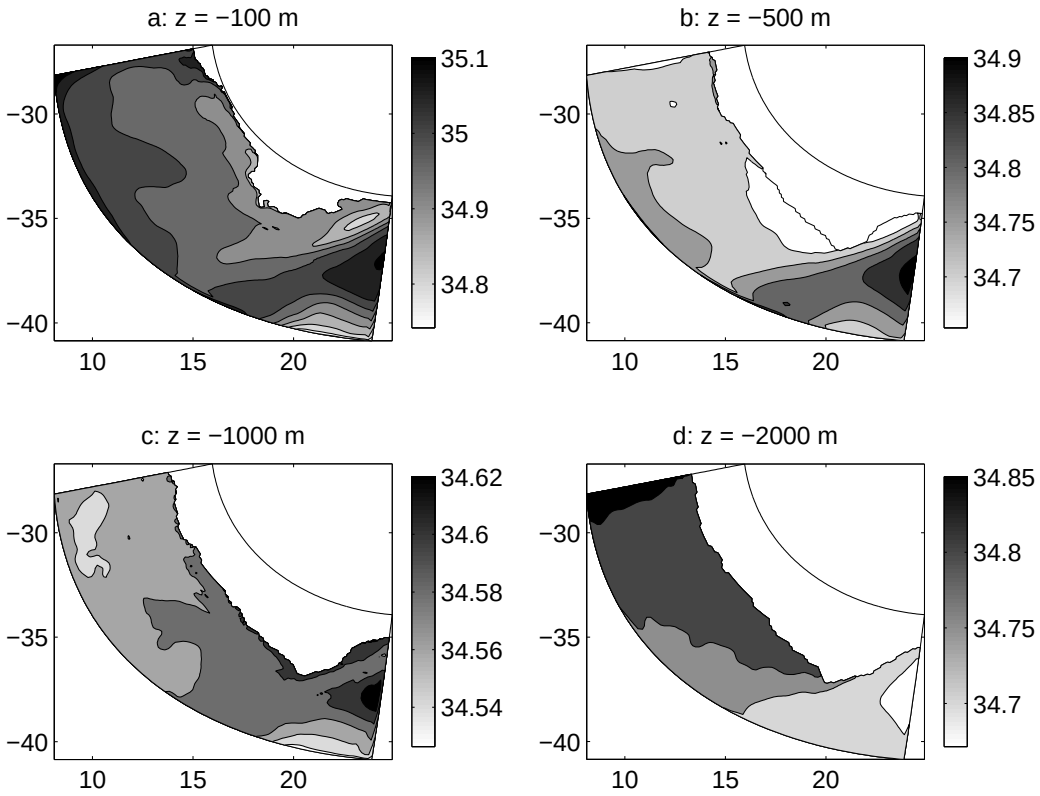

Figure 3.35 Salinity annual climatology (PSU) for the high resolution experiment. a: for $z = -100$ m, b: for $z = -500$ m, c: for $z = -1000$ m, and d: for $z = -2000$ m. The horizontal coordinates account for the longitude and the latitude.

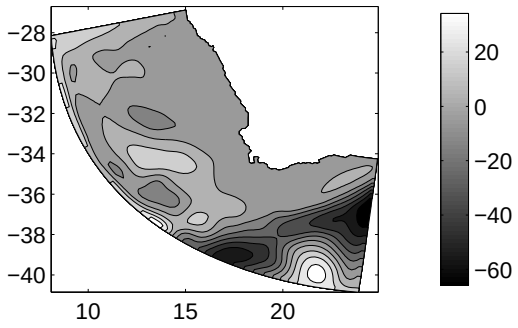

Figure 3.36 Transport stream function (Sv) derived from annual climatology of the high resolution experiment. The isocontour interval is 10 Sv. The horizontal coordinates account for the longitude and the latitude.

takes the form:

$$\begin{aligned} \frac{\partial < \zeta >}{\partial t} + \frac{\partial}{\partial x}(H < \bar{u} >) + \frac{\partial}{\partial y}(H < \bar{v} >) &= 0 \\ \rightarrow \frac{\partial}{\partial x}(H < \bar{u} >) + \frac{\partial}{\partial y}(H < \bar{v} >) &= 0 \end{aligned} \tag{3.43}$$

Hence, the time averaged transport is non-divergent and a time averaged transport function can be extracted from the time averaged barotropic velocities. The resulting time averaged transport function for the high resolution experiment is portrayed on figure (3.36). It shows that the averaged transport associated with the Agulhas Current is around 65 Sv, and that the averaged transport of the simulated part of the Benguela ranges from 10 Sv to 20 Sv. These values can be compared to the measured transport of 75 Sv for the Agulhas Current and of 15 Sv for the a similar part of the Benguela current (figure 1.5) [*Shannon and Nelson,* 1996].

3.5.2 Comparison with temperature and salinity data

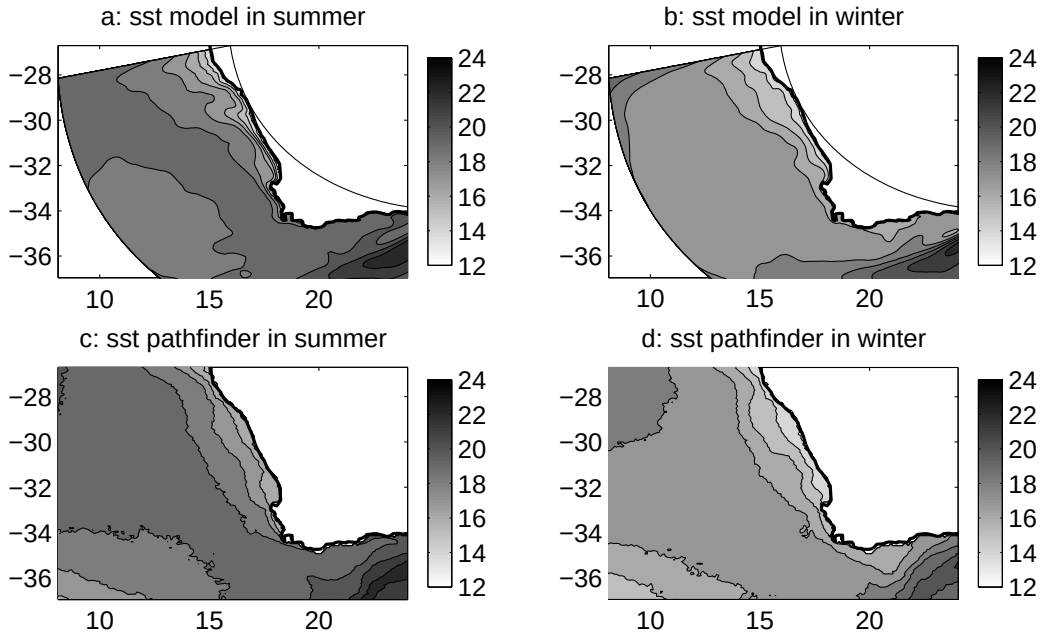

Figure 3.37 a: sea surface temperature for the high resolution experiment for the summer months. b: sea surface temperature for the high resolution experiment for the winter months. c: sea surface temperature from the pathfinder satellite data set for the summer months. d: sea surface temperature for the from the pathfinder satellite data set for the winter months. The interval between the isotherms is 1^oC.

Though the linear parameterization of the sea surface temperature feedback on the sea surface heat fluxes can be seen as a restoring term toward climatological sea surface temperature data, it makes sense to compare the averaged sea surface temperature generated by the model to more accurate data than the ones employed to force the model. In figure (3.37), the model sea surface temperature is compared to sea surface temperature measured from 1987 to 1999 by satellite Pathfinder with an accuracy of 9 km. To make the comparison possible, satellite and model data are averaged separately in the austral winter months (from April

to September) and in the austral summer months (from October to March). It can firstly be noticed that the seasonal sea surface temperature patterns obtained from the high resolution simulation differ from the smooth climatology used to force the model (figure 3.13), whereas it compares remarkably to the Pathfinder averaged data (figure 3.37), denoting a good behavior of simulated smaller scale structures. For the summer months, one can note on the panel (3.37-a) that the upwelling starts from Cape Agulhas with identical values in the Pathfinder dataset (figure 3.37-c). The temperature in a very narrow band close to the coast around 32^o S is 3^oC to 4^oC smaller in the simulated field (figure 3.37-a) than in the observation (figure 3.37-c). This can be related to the wind forcing which is too large close to the coast and/or to a small inaccuracy in the satellite measurement of the sea surface temperature close to the west coast. The summer pathway of the modeled 18^oC isotherm that detaches from Cape Columbine to come back to the coast 150 km downstream along the coast (figure 3.37-a) is identical, between 35^o S and 31^o S, to the pathway of the 17^oC isotherm in satellite data (figure 3.37-c). Further North, in summer, the modeled isotherm tends to move off-shore to come back towards the coast near the northern open boundary. This behavior is not observable on satellite data. A little bump in the 20^oC isotherm is present at the southern tip of the Agulhas Bank both in the model and satellite data for the summer months (figures 3.37-a and 3.37-c). It is the signature of the shelf edge equatorward current flowing from the southern tip of the Agulhas Bank towards Cape Peninsula. On the eastern part of the Agulhas Bank, a reverse plume is present in model data, whereas only a bend in the Agulhas Current is visible on satellite sea surface temperature data. For the winter months, the model solution (figure 3.37-b) is also close to the pathfinder sea surface temperature data (figure 3.37-d). Particularly, the cooling of surface waters on the inner Agulhas Bank and the standing wave pattern (with a wave length of about 150 km) just North of St Helena Bay can be observed in both portrayals (figures 3.37-b and 3.37-d).

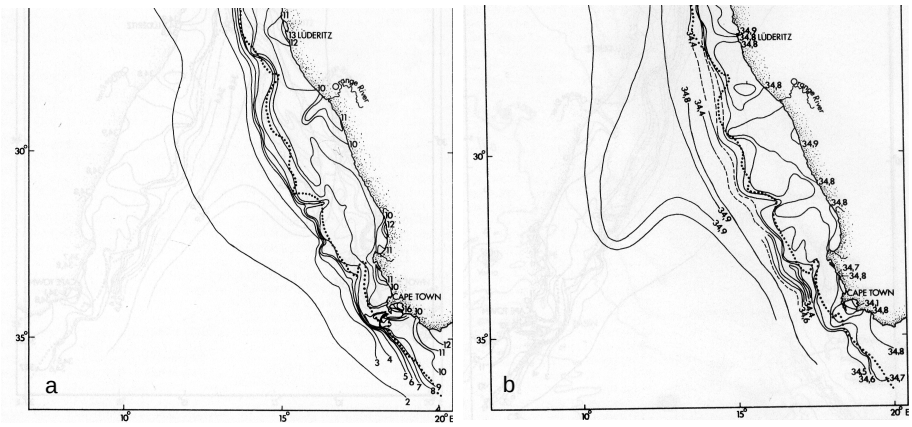

Figure 3.38 a: average sea-bottom temperatures (^{o}C) over the continental margin off south-western Africa. b: average sea-bottom salinities (PSU) over the continental margin off south-western Africa. Adapted from Dingle and Nelson [1993].

Dingle and Nelson [1993] have extracted the temporal average of a large amount of temperature and salinity data for the bottom of the ocean along the west coast of South Africa (figure 3.38). The first level of the s-coordinate follows the bottom of the ocean. Hence, it is straightforward to extract averaged values for the simulated sea bottom temperature and salinity (figure 3.39) to compare to observations. The model bottom temperatures on the abyssal plain (2^oC) and on the slope along the west coast (figure 3.39-a) are identical to the

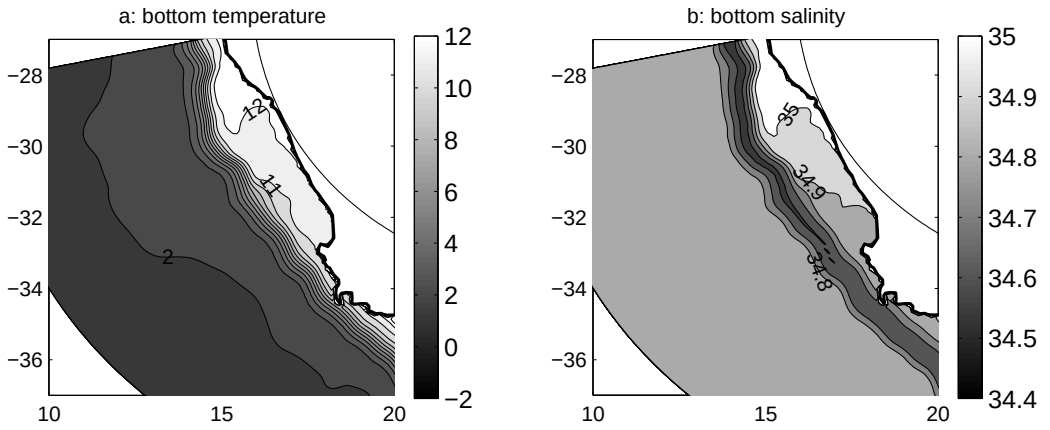

Figure 3.39 a: simulated climatological bottom temperatures (^{o}C) . b: simulated climatological bottom salinities (PSU).

observed ones (figure 3.38-a). On the shelf, the model bottom temperature is warmer ($\sim$ 11-12 ^{o}C) than the observations ($\sim$ 9-10 ^{o}C), this difference can be a consequence of the absence of a parameterization of the bottom mixed layer during the simulations. Because river runoffs are not taken into account during the simulation, the warm signature of the Orange River outflow, noticeable on figure (3.38-a), is not visible on the model outputs. The invasion of colder water on the shelf from the South, described by Dingle and Nelson [1993], is visible both in the model and the observations. The same remarks can be made for the salinity with bottom shelf waters saltier ($\sim$ 34.8-35 PSU, figure 3.39-b) than in the observations ($\sim$ 34.7-34.9 PSU, figure 3.38-b). The minimum of salinity due to the Antarctic Intermediate Water, observed along the slope (34.4 PSU, figure 3.38-b), is a bit smaller than the minimum visible in the outputs of the model (34.6 PSU, figure 3.39-b). This difference can be due to the data employed at the model initialization and in the forcing of the model open boundaries.

These model-data comparisons show a correct behavior of the time averaged model solution. The analysis has now to be extended to check if the variability of the modelized circulation compares also to the observations. This is done in the next section.

3.5.3 Variability

The previous section was focusing on the time average model variables ($< X >$). In this section we will concentrate on the anomalies departing from the time averaged variables ($X' = X - < X >$). By definition, the time average of the anomalies is zero, thus we will concentrate on the variance of the anomalies ($< X'^2 >$). The standard deviation, or root mean square, can be obtained by taking the square root of the variance ($\sqrt{< X'^2 >}$). It is an indicator of the variability produced during the simulations.

The root mean square of the sea surface temperature is portrayed on figure (3.40-top) for the model results from year 3 to year 10 and on figure (3.40-bottom) for monthly Pathfinder satellite data from 1987 to 1999. The model solution and the measured sea surface temperature variability compare fairly well. Quite surprisingly, there is a minimum of variability (1.5 ^{o}C) in St. Helena Bay both for the model solution and for the observations. This can be due to the presence of the Cape Columbine upwelling plume that counters the seasonal variations of surface temperature. On the contrary, a maximum of variability is also present on the inner Agulhas Bank (2.5 ^{o}C) both for the model solution and for the satellite measurements. It can

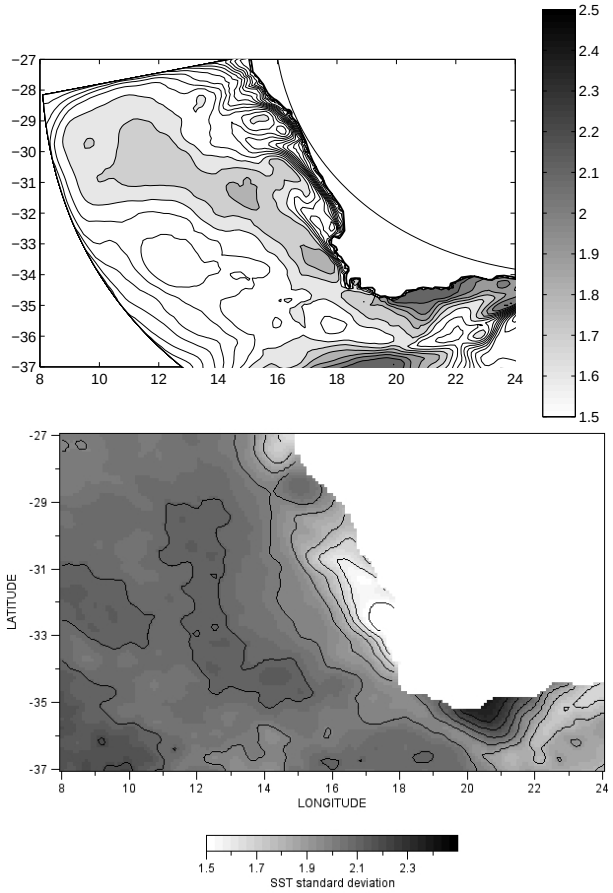

Figure 3.40 Root mean square of the sea surface temperature anomaly (^{o}C). top: from the high resolution experiment. b: from monthly Pathfinder (1987-1999) satellite data. The interval between the isocontours is 0.1 ^{o}C. The horizontal coordinates account for the longitude and the latitude

be related to the strong seasonal variations associated with the local surface forcing of the area. Offshore of Cape Columbine, a maximum in sea surface temperature variability follows the pathway of the cyclonic eddies generated from Cape Columbine and the Cape Peninsula during the model simulation. Offshore of this maximum, a large area with low sea surface modelized temperature variability (1.4^{o}C) is in disagreement with satellite data (2.4 ^{o}C) . This might be related to the absence of the Agulhas rings that induces important variations in sea surface temperature but which are immediately radiated by the offshore open boundary after their generation during the model simulation.

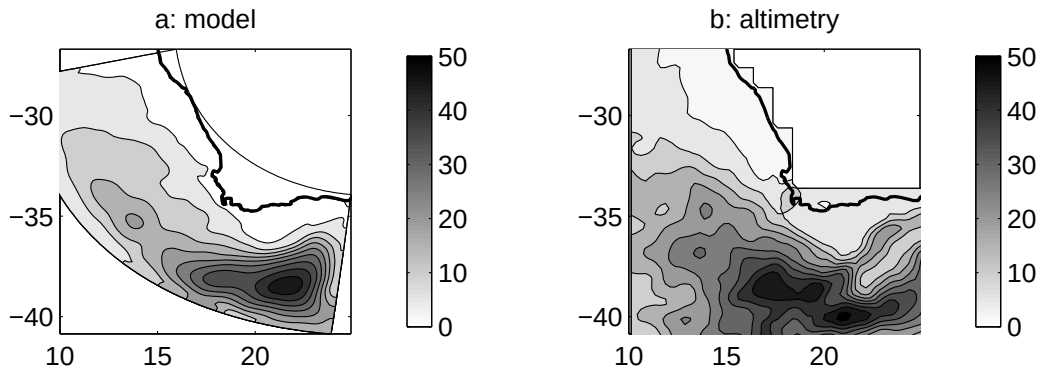

Figure 3.41 Root mean square of the sea surface elevation anomaly (cm). a: from the high resolution experiment. b: from satellite altimer data. The interval between the isocontours is 5 cm. The horizontal coordinates account for the longitude and the latitude.

The root mean square of the sea surface elevation has been computed at high resolution (0.25^o) from combined Topex-Poseidon and ERS1 altimetry data from October 1992 to October 1997 [*Ducet et al.,* 2000]. It shows a local maximum (50 cm) in the Agulhas retroflection area and minimums over the shelves of the South and West coasts (0-5 cm off the west coast and 5-10 cm of the Agulhas Bank, figure 3.41-b). Away from the open boundary sponge layers, this behavior is remarkably well simulated, qualitatively and quantitatively, in the high resolution experiment (figure 3.41-a). Difference between the model and the altimetry variance in sea surface elevation is present around 17.5^o E and 37^o S, in the pathway of the Agulhas rings. At this location, a maximum in sea surface elevation variance is noticeable in the altimetry data, but is not present in the outputs of the model simulation. This discrepancy can be related, as explained previously, to the vicinity of the open boundary not allowing the Agulhas rings to evolve properly.

The eddy kinetic energy per unit of mass $\left(\frac{1}{2}(u'^2 + v'^2)\right)$ has been also derived from high resolution altimetry data [*Ducet et al.,* 2000]. It also shows an important maximum in the Agulhas retroflection area (4000 cm^2.s^{-2}). The variations in the incoming Agulhas Current correspond to a narrow band of high eddy kinetic energy (> 2000 cm^2.s^{-2}) (figure 3.42-b). North of 35^o S and West of 20^o E, the subsurface eddy kinetic energy (computed for z = -50 m) coincides qualitatively and quantitatively with the observed eddy kinetic energy (figure 3.42-a). This shows that the eddies formed from the Cape Peninsula and Cape Columbine have a correct behavior. Because the incoming Agulhas Current is forced at the eastern boundary from smooth climatology data the remote variations in the Agulhas Current, like Natal pulses and meanders, are not resolved by the model. Hence, very low eddy kinetic energy is present along the eastern part of the Agulhas Bank in comparison to the observations. As a consequence, the simulated eddy kinetic energy is 2 times smaller than the observations in the retroflection area.

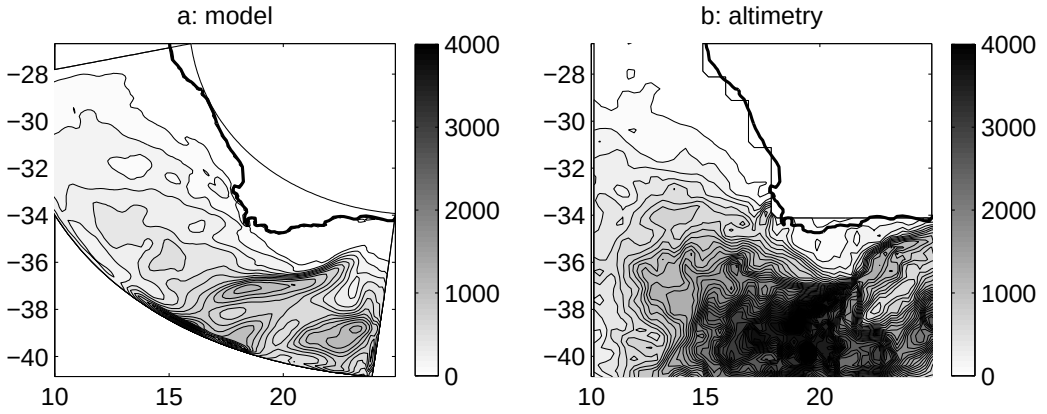

Figure 3.42 Subsurface (-50 m depth) eddy kinetic energy ($cm^2.s^{-2}$). a: from the high resolution experiment. b: from satellite altimer data. The interval between the isocontours is 100 $cm^2.s^{-2}$. The horizontal coordinates account for the longitude and the latitude.

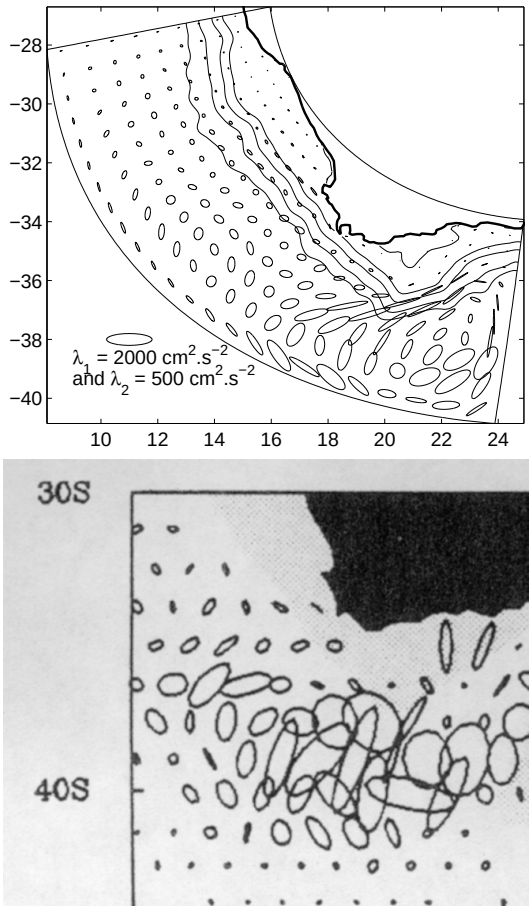

Figure 3.43 Top: subsurface (-50 m depth) velocity-variance ellipses. One ellipse is portrayed every 6 grid points. Bottom: velocity-variance ellipses from the times series components derived from Geosat altimetry data, adapted from Morrow et al. [1994]. The scale is the same in each portrayal, represented by the ellipse in the bottom-left corner of the top panel.

The eddy kinetic energy shows that important variability occurs near steep topography around the South West corner of Africa. Hence, we can expect the variability to be strongly anisotropic. This as been observed from satellite altimer data [*Morrow et al.,* 1994]. An analysis is conducted to see if the model reveals this anisotropic aspect of the current variability. The magnitude and the direction of the eddy variability are represented as in Morrow et al. [1994], using variance ellipses. The current variations being u' and v', following Morrow et al. [1994], the direction θ of the major axis of variability, measured anti-clockwise from the direction of the u velocity component is:

$$\tan\theta = \frac{\lambda_1 - < u'^2 >}{< u'v' >} \tag{3.44}$$

where λ_1 is the variance along the major axis and is given by

$$\lambda_1 = \frac{1}{2}\left(< u'^2 > + < v'^2 > + \sqrt{(< u'^2 > - < v'^2 >)^2 + 4 < u'v' >^2} \right) \tag{3.45}$$

and λ_2 is the variance along the minor axis given by

$$\lambda_2 = \left(< u'^2 > + < v'^2 > \right) - \lambda_1 \tag{3.46}$$

Note that the eddy kinetic energy (EKE) is connected to the velocity variance by

$$EKE = \frac{\lambda_1 + \lambda_2}{2} \tag{3.47}$$

The subsurface variances ellipses are represented for the high resolution model for z = -50 m (figure 3.43-top). They show a high degree of similitude with the variances ellipses derived from Geosat satellite altimer data (figure 3.43-bottom). The remarks made for the eddy kinetic energy are also valid for the variances ellipses: good comparison along the west coast, whilst the ellipses are smaller for the model outputs in the Agulhas retroflection area. The incoming variability pattern of the Agulhas Current is illustrated by the two elongated ellipses on the Eastern part of the Agulhas Bank for the satellite analysis (figure 3.43-bottom). This shows important cross isobath variations (characteristic of the meanders and natal pulses) in the Agulhas Current around 23^o E. As explained previously, this variability generated upstream of the area is not resolved by the model. As a consequence, the simulated variability in the Agulhas retroflection area is two times smaller than the observations. Both the model results and the observations show an important anisotropy in the variability, mostly near strong topographic gradients. This anisotropy is important along the southern tip of the Agulhas Bank. The variability appears to be more isotropic on the south west of the Agulhas Bank (where the Agulhas rings are shed) for the observations. This behavior is not noticeable in the model solution, the Agulhas rings being quasi-immediately in contact with the offshore open boundary. Along the West Coast, where altimeter data are available, the model and satellite variances ellipses compare fairly well. This is especially true near the Cape Peninsula, where the presence of the cape induces a strong anisotropy in the subsurface current variability. Animations of the model output reveals that cyclonic eddies are mostly generated from Cape Columbine, Cape Peninsula and the Southern tip of the Agulhas Bank. These areas of eddy generation coincides with areas of strong anisotropy of the current variability. Another interesting feature is the anisotropy of the variability close to the open boundaries. It happens that the open boundary inhibits the cross boundary velocity variance. This can be an effect of the Flather open boundary scheme that constrains the cross boundary barotropic velocities to remain close to smooth climatology data values.

One can conclude from this section that though the strong variations in the Agulhas Current coming from the Indian Ocean are not taken into account in the model solution, and disregarding the Agulhas ring behavior when they have a size comparable to the model width, the variability developed in the model in the form of eddies, plumes,... compares remarkably well to observations. This is particularly true along the South African West Coast.

3.5.4 Along the West Coast

Because of its importance for the biological components, the model solution of the Benguela upwelling system along the South African West Coast is analyzed in more detail.

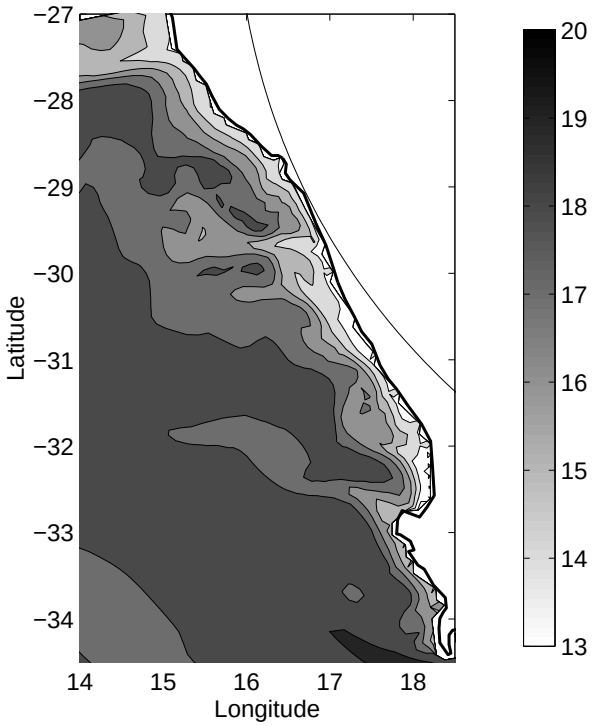

Figure 3.44 sea surface temperature along the west coast of South Africa the 30 November of model year 4.

The upwelling system is characterised by the presence of cold water at the coast induced by the Ekman divergence forced by the summer equatorward winds. As explained in the first chapter, the resulting upwelling front is highly convoluted and shows characteristic patterns such as the upwelling plumes extending from Cape Peninsula, from Cape Columbine and from the Namaqualand upwelling centers around 30.5^o S. Other characteristic features are the cyclonic eddies that are shed from the capes. Because these patterns have been mostly related to the small scale spatial and temporal structure of the wind forcing [*Jury,* 1985a, *Jury,* 1985b, *Jury et al.,* 1985, *Jury,* 1986, *Jury and Taunton-Clark,* 1986, *Jury,* 1988, *Kamstra,* 1985, *Taunton-Clark,* 1985], one might expect that a model solution only forced by a coarse smooth climatological wind field (see figure 3.10) should not generate these elements, characteristic of the Benguela upwelling system. This is not the case. Looking at the modelized sea surface temperature at the beginning of the upwelling season, the 30 November of model year 4 (figure 3.44), one can note that most of observed patterns of the upwelling front are present during the high resolution experiment:

- A small cyclonic eddy, characterized by core of colder water located at 17.2^o E and 33.6^o S, has detached from the Cape Peninsula upwelling center and is advected in a north-westward direction.
- A large upwelling plume, showing the characteristic inverted s shape described by Shannon [1985], extends from Cape Columbine.
- Upwelling filaments extend from a well defined Namaqualand upwelling center at 30.5^o S.

The shape and dimensions of these simulated features compare well with the observations. Hence, the mesoscale activity of the Benguela upwelling system is driven by intrinsic oceanic instability processes and is triggered by topography, as explained by Batten [1997]. The small scale wind structure doesn't appear to be the main driving forcing of this mesoscale activity.

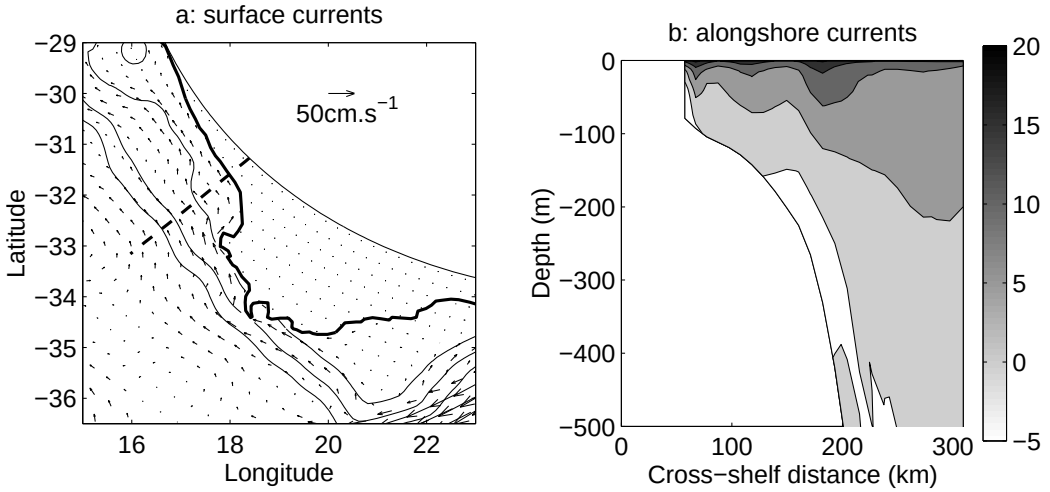

Figure 3.45 a: the South and West Coast time averaged currents (cm.s^{-1}) at 30 m depth. One vector is portrayed every 3 vectors. b: along shore current (cm.s^{-1}, positive towards the equator) cross section North of Cape Columbine. The greyscale range represents the equatorward along shore current in cm.s^{-1}. The isocontour interval is 5 cm.s^{-1}. The position of the cross section is given by the dashed line on panel a

The time averaged subsurface modelized currents are highly controlled by the topography (figure 3.45-a). A large amount off Acoustic Doppler Current Profilers data has been collected by Boyd and Oberlholster [1994] to generate a time averaged map of the 30 m depth currents on the shelves of the South and West coasts of South Africa. Important quantitative similitude occurs in the comparison between the model outputs and the ADCP data:

- A reverse flow of about 10 cm.s^{-1} is visible on the 200 m isobath on the Eastern Agulhas Bank.
- A sluggish circulation is present on the Agulhas Bank.
- A shelf edge jet of about 25 cm.s^{-1} flows from the Southern tip of the Agulhas Bank towards Cape Peninsula and Cape Columbine.
- A convergent flow occurs on the western margin of the Agulhas Bank to fill the Cape of Good Hope jet.

- The flow North of Cape Columbine follows the 200 m isobath that curves inshore at 31.5^o S and moves offshore at 30^o S with characteristic velocities of 20 cm.s^{-1}.

The principal discrepancy between the model and ADCP data is the current in St Helena Bay, in a narrow band just North of Cape Columbine. For the ADCP data, the flow in St Helena Bay is weak and show a cyclonic motion, as explained by Holden [1985] and simulated by the barotropic experiment in the second chapter. For the realistic simulation, an important flow of 20 cm.s^{-1}, follows the Northern part of Cape Columbine to fill St Helena Bay. The results of the second chapter might give an explanation of this phenomenon. In the barotropic experiment, the sluggish circulation is present inside the attached cyclonic eddy that develops on the flat portion of the shelf where the dynamics are controlled by a balance between advection of vorticity and bottom friction. Although weighted by $\frac{\nabla H}{H}$, the Shapiro filter employed to smooth the bottom topography for the realistic experiment removed the flat portion of the shelf in St Helena Bay. The resulting bottom topography corresponds more to the exponential topography employed for the analytical standing shelf wave solution (figure 2.14). In the case of the exponential topography, the vortex stretching term gains importance and the flow sticks to the downwind side of the cape (figure 2.17-a) as for the realistic experiment.

A cross-shelf cross section of the time averaged along shore velocities North of Cape Columbine for the upper 500 m depth is portrayed on figure (3.45-b). It shows an equatorward baroclinic jet of 20 cm.s^{-1} above the shelf break. A net poleward motion with velocities of 5 cm.s^{-1} is present on the shelf break in agreement with the current meter measurements of Nelson [1989]. A subsurface poleward current is also present at the coast with velocities of 5 cm.s^{-1}. This is also in agreement with observations [*Boyd and Oberholster,* 1994, *Nelson,* 1989].

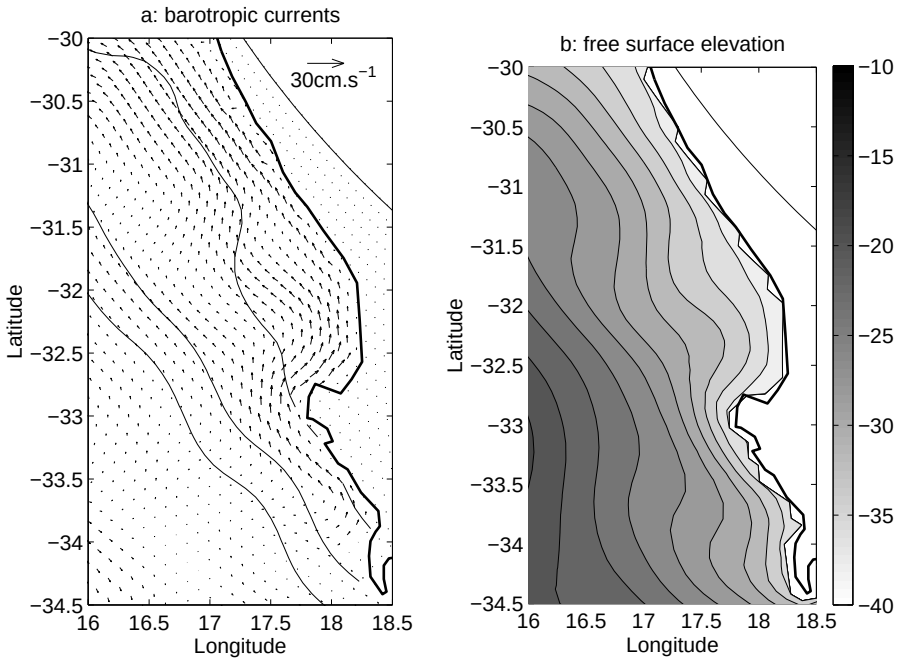

Figure 3.46 a:the South and West Coast time averaged barotropic currents (cm.s^{-1}). All velocity vectors are represented. b: annual averaged free surface elevation. The greyscale range represents the free surface elevation in m.

In order to compare the output of the realistic simulation to the results of the second chapter, the time averaged barotropic velocities and free surface elevation are portrayed for a small area centered on St Helena Bay in figure (3.46). Note that in presence of a baroclinic pressure gradient induced by the stratification, the baroclinic velocities are no longer in geostrophic equilibrium due solely to the pressure gradient induced by free surface elevation. The annual averaged along shore wind stress utilized to force the model in the area limited by the bounds of figure (3.46) is 0.5 $N.m^{-2}$. The characteristic barotropic velocities on the shelf in figure (3.46-a) are of about 7.5 $cm.s^{-1}$ which is slightly smaller than the values obtained in section (2.8) for the case of the exponential shelf for this wind forcing. For both the barotropic velocities and the free surface elevation, a standing wave pattern is noticeable in the lee of Cape Columbine (figure 3.46-a). It has a wave length of approximately 100 km. The wave length for the first barotropic standing wave mode derived in section (2.8), using an exponential topography and an along shore mean current of 7.5 $cm.s^{-1}$ is 60 km. This is 1.6 times smaller than the wave length observed in the realistic experiment. Different arguments can be advanced to explain this difference: firstly, one can note that the topography of the realistic experiment is not constant along West Coast, with the 200 m isobath moving towards the coast around 31.5^o S. This can alter the vorticity equation employed to derived the standing wave equation. Secondly, the presence of stratification can alter the behavior of the standing coastal trapped waves. Looking at the dispersion relation for coastal trapped waves for different stratification [*Huthnance,* 1978], one can note that the wave length decreases for a given phase velocity (hence for a fixed advection by a mean along shore current in the standing wave case) with increasing stratification, invalidating this second argument. Thirdly, the hypothesis made in section (2.8) that the along shore mean current is barotropic is surely not valid in the realistic case where the along shore currents associated with the upwelling are a surface baroclinic jet. The process of a standing barotropic shelf wave excitation by a baroclinic surface jet has not been treated in section (2.8). In this case, the model of a cape moving in still water is invalid. Surprisingly, if we introduce the subsurface velocity observed on figure (3.45) as the mean along shore current (20 $cm.s^{-1}$) in the standing wave equation, we obtain exactly 100 km for the wave length of the first mode. This can not be taken as a proof. Nevertheless, we still can note that the time averaged circulation simulated on the shelf in St. Helena Bay for the realistic experiment is qualitatively in agreement with the results of the standing shelf wave analytical study of section (2.8).

The same analysis is made for the middle of the upwelling season: for the month of February (figure 3.47). For this particular month, the along shore wind stress on the west coast has an averaged value of 0.075 $N.m^{-2}$. The averaged barotropic currents portrayed in figure (3.47-a) have a characteristic velocity of about 10 $cm.s^{-1}$. An interesting feature in figure (3.47) is the separation of the flow into 2 branches past Cape Columbine: one branch filling St Helena Bay, the other one flowing north westward parallel to the coastline to come back to the coast 150 km North of Cape Columbine. This is characteristic of the Columbine divide described by Shannon [1985] (figure 1.13). Whereas the inner branch shows a standing wave pattern comparable of the annual averaged circulation, the behavior of the outer branch resembles the attached cyclonic eddies modelized in the second chapter. For this value of wind stress, the size of the eddy described in chapter 2 is 60 km (figure 2.6), which is smaller than the size of the detachment pattern observed in figure (3.47). On the contrary the length scale predicted by the balance between advection and bottom friction (equation 2.21) is 125 km, which is relatively close to the size of the pattern observed in figure (3.47). This last result should be taken cautiously, since stratification or variations in bottom topography can seriously alter the circulation within St. Helena Bay.

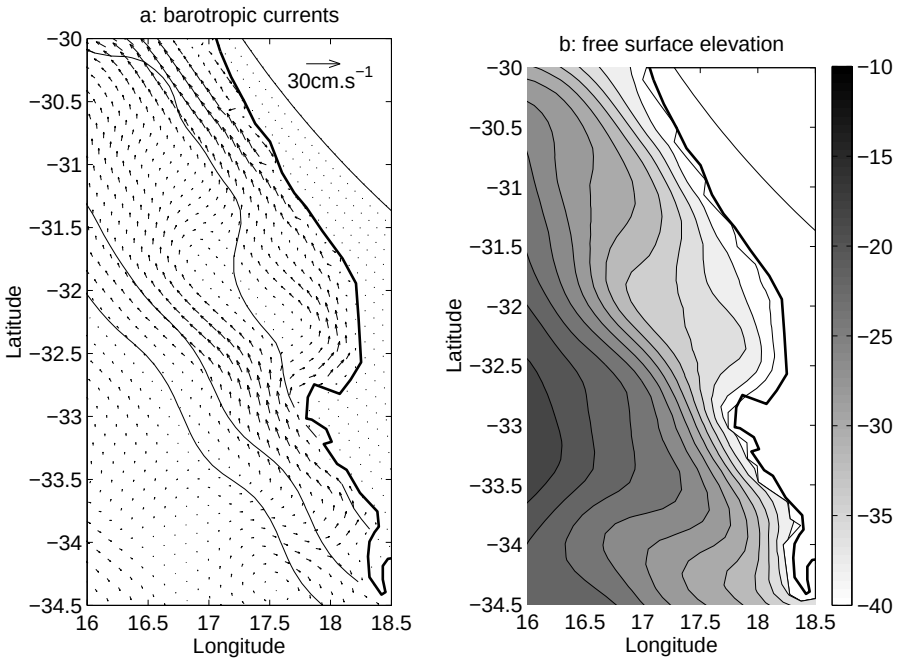

Figure 3.47 a: south and west coast averaged barotropic currents (cm.s^{-1}) for February. All velocity vectors are represented. b: averaged free surface elevation for February. The greyscale range represents the free surface elevation in m.

3.5.5 Generation of cyclonic eddies by the Agulhas Current in the lee of the Agulhas Bank

Though the realistic configurations have been principally set up to study the shelf dynamics around the South-west corner of the African continent, and particularly the Benguela upwelling system, the results of model regarding the Agulhas Current has motivated the redaction of two papers. They focus attention on specific mesoscale processes produced by the model, observed in nature, and not simulated before in this area. The present section describes the generation of cyclonic eddies by the Agulhas Current in the lee of the Agulhas Bank [*Penven et al.,* accepted]. The second paper, still in preparation, forms the next section.

The inter-ocean exchanges brought about by the shedding of Agulhas rings south-west of Africa has been much studied because of their global climatic implications [*Lutjeharms*, 1996; *De Ruijter et al.*, 1999]. Recent models have shown that this movement of warm water from the Indian to the Atlantic may in fact control the rate of thermohaline overturning of the whole Atlantic [*Weijer et al.,* 1999]. There are also other, smaller sources of exchange including Agulhas filaments [*Lutjeharms and Cooper,* 1996] and intrusions of cold subantactic water [*Shannon et al.,* 1989]. In addition, a number of cold, cyclonic eddies have been observed in the South-east Atlantic [e.g. *Duncombe Rae et al.*, 1996; *Gründlingh*, 1995]. For a proper quantification of the inter-ocean exchanges the characteristics of all these components need to be known. The origin, behavior and potential role in inter-ocean exchanges of the cyclonic eddies have not been established. We verify if the high resolution model might simulate these cyclonic eddies, and we investigate the origin of such cyclonic eddies.

The model gives a realistic portrayal of the known circulation in this ocean region (figures 3.48-a and 3.50-b), including mesoscale details such as the Agulhas Current, shear edge features on the landward border of the current, Agulhas rings and the wind-driven coastal

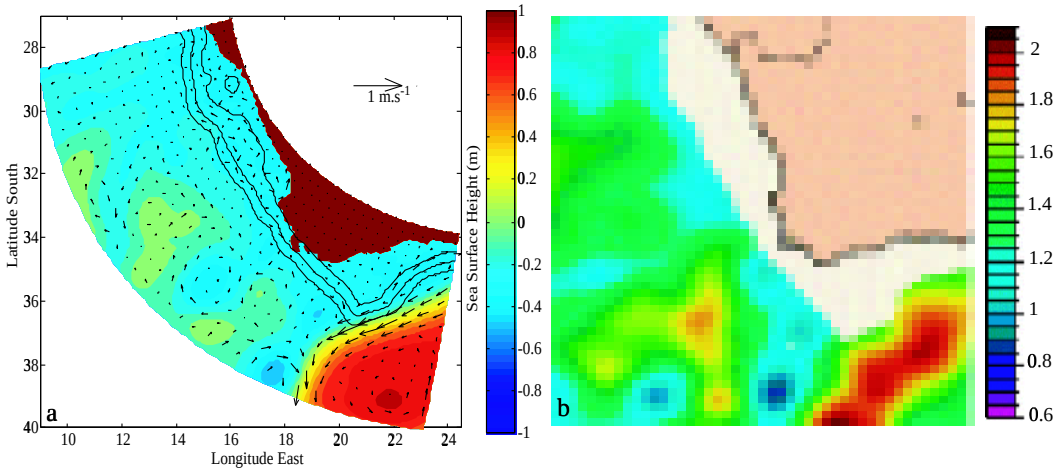

Figure 3.48 (a) Model simulation of the sea surface height and barotropic velocities (1 vector every 4 grid points) on 27 April of model year 2. (b) Naval Research Laboratory, MODAS 2.1, sea surface height derived from in-situ and satellite altimetry data on 16 January 1993.

upwelling along the west coast. The Agulhas Current overshoots the concave eastern part of the Agulhas Bank and has its maximum surface velocities of about 1 m.s^{-1} at the southernmost tip of the shelf. These simulations are all in very good agreement with observation [e.g. *Lutjeharms et al.*, 1989]. The features evident in the modeled sea surface height are also well represented in the sea surface height observed by altimetry (figures 3.48-a and 3.48-b). These consist of an anti-cyclonic Agulhas ring as well as some cyclonic eddies of unknown origin. One of these cyclonic eddies lies between the Agulhas Current and the western side of the Agulhas Bank in both portrayals. Cyclonic eddies are prevalent at this particular location in the model and this portrayal is therefore quite characteristic in this respect.

An analysis of the generation, drift and persistence of cyclonic eddies at this location as observed in satellite altimetry is highly consistent with the model simulations (figure 3.49). They are formed at roughly the same location, drift off in the same westerly direction, are produced with the same frequency, and can dissipate rapidly or grow in intensity. These results give us confidence that these features are not model artifacts. It would be important to establish the depth and other hydrographic characteristics of these particular cyclonic eddies.

The sea surface temperature and current portrayals in the upper panels of figure (3.50) exhibits substantial agreement. The model shows a plume of warm surface water that encircles a cyclonic eddy in the lee of the continental shelf (figure 3.50-b). To the North, there is faint indication of an anti-cyclonic eddy in the current vectors, encircled by the extension of the warm filament. The satellite thermal infrared image shows much the same (figure 3.50-a), except that the locations of the two features are slightly displaced. A vertical temperature section through the two eddies in the model shows the warm surface filaments as well as an anti-cyclonic eddy centered at 35.3^o S and a cyclonic eddy at 36.7^o S (figure 3.50-d). In the model, the eddy is still noticeable at 1500 m depth. An XBT section was undertaken across this region in a very similar location [*Bathmann et al.*, 1994]. It is shown in the left-hand panels of figure (3.50). Regrettably, the sea surface temperature image was largely obscured by cloud on the day of the hydrographic section. Nonetheless, the position of the feature could be located and is shown relative to that of the 27 November 1992 by the dotted line in figure (3.50-a). The vertical temperature section for this line resembles closely that of the

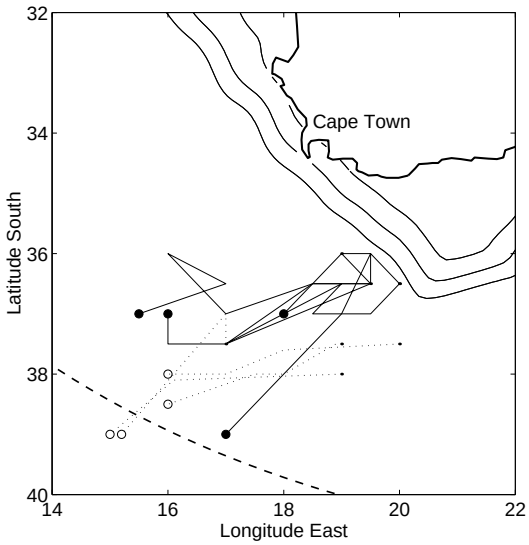

Figure 3.49 The drift patterns for a few characteristic cyclonic eddies west of the continental shelf. The bold tracks are for model eddies shed during model year 3; the dotted tracks for cyclones observed in Naval Research Laboratory, MODAS 2.1 sea surface height analysis for 1993.

model, both in the surface filaments as well as in the presence of both a cyclonic as well as an anti-cyclonic eddy (figures 3.50-c and 3.50-d). The strong resemblance of the hydrographic and model results shows that the cyclonic eddies generated off the Agulhas Bank in the model are not inconsistent with observations and extend to substantial depths.

In the model, the coastal part of the Agulhas Current tends to follow the topography at the southern tip of the Agulhas Bank, carrying warm surface filaments spreading northward towards Cape Peninsula. At times, the southern part of this flow detaches from the topography and a cyclonic meander developes. After approximately 1 month, it detaches from the Agulhas Bank, taking away the warm filament (see Figures 3-a and 3-b). Occasionally, a cyclonic perturbation may follow the shelf break from the eastern Agulhas Bank and trigger the cyclonic eddy generation process. The averaged values of the Rossby ($R_o = 0.04$) and Burger ($S = 3.8$) numbers have been computed as described in Boyer and Tao [1987], taking the width of the Agulhas Current as a characteristic length scale (100 km). They lie in the cyclonic eddy shedding regime found in rotating tank experiments, when a linearly stratified flow encounters an obstacle [*Boyer and Tao,* 1987]. Thus, the generation of cyclones past the Agulhas Bank can be explained by a flow detachment process. Their characteristic diameters range from 50 km to 200 km. Although they are generated irregularely, the number of eddy shed each year is relatively constant, respectively from year 1 to year 10: {3,3,4,4,4,5,4,5,4,5}. Because the model domain has a limited size, most of the cyclonic eddies are radiated through the offshore boundary before decaying (figure 3.49).

The first simulations of the southern Agulhas Current by a model with high spatial resolution suggests that the disposition of the current relative to the southernmost part of the African continental shelf is such that cyclonic lee eddies may be generated. This may be an intermittent process since the Agulhas Current does not follow the most southerly part of the shelf consistently [*Lutjeharms et al.,* 1989]. The model indicates that these eddies may be shed at irregular intervals. They may subsequently move off in a number of directions in the South-West Indian Ocean [*Gründlingh,* 1995]. Their further dispositions, their contribution to

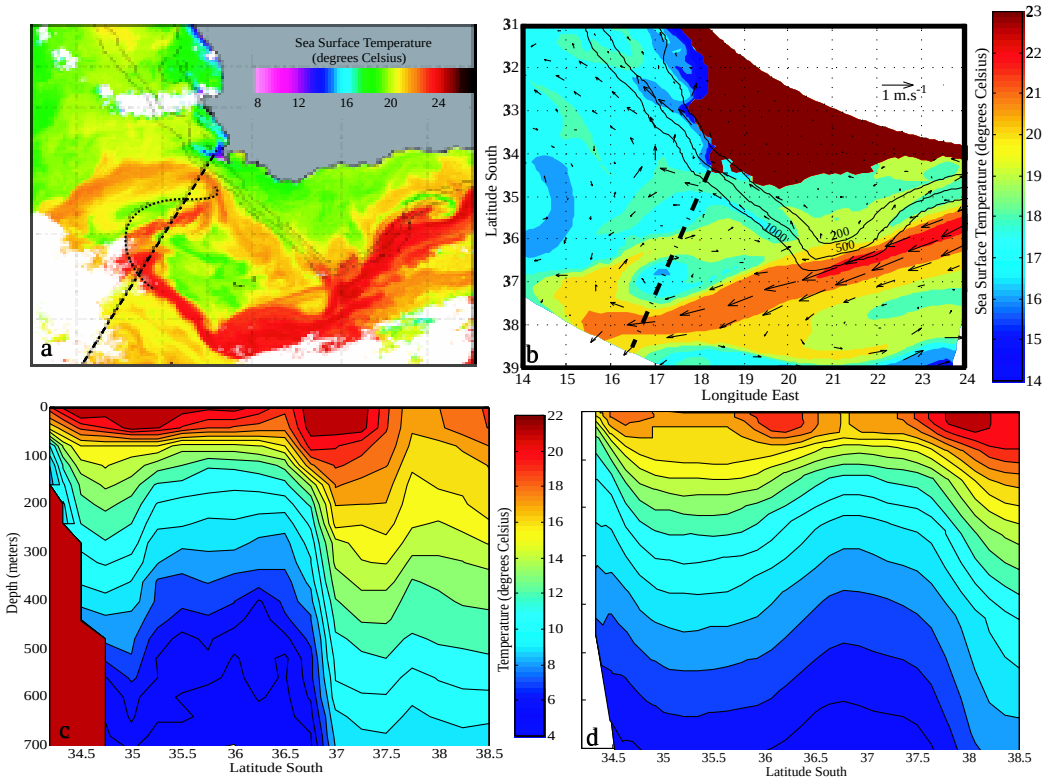

Figure 3.50 A comparison between a characteristic cyclonic eddy generated off the Agulhas Bank in the model (b and d) and one observed at sea (a and c). The panel b shows the simulated surface currents and sea surface temperature on 21 November of model year 4. It also shows the line along which a vertical temperature section (d) has been extracted from the model at the same date. The sea surface temperature generated from NOAA 11 AVHRR data (a) is for 27 November 1992. The straight broken line shows the cruise track of the research vessel "Polarstern" that left Cape Town on 3 December 1992. The dotted line shows the location of the warm filament on 4 December 1992 when the vessel would have been in the center of this feature. The vertical temperature section (c) was measured by XBT (expendable bathythermograph) from the ship. The locations of the 200 m, 500 m and the 1000 m isobaths are shown in panels a and b.

the melange of water masses in this ocean region as well as their potential role in stabilizing Agulhas rings (Kizner, personal communication) all need to be determined. If all cyclonic rings in the south-western Atlantic have this suggested origin, they will not contribute to inter-ocean exchanges since they are generated *in situ*.

3.5.6 Shear edge eddies of the southern Agulhas Current

The southern and the northern parts of the Agulhas Current consistently exhibit differences in their path characteristics. Whereas the trajectory of the northern part is unusually stable for a western boundary current [*Gründlingh,* 1983], the southern part has large meanders [*Harris et al.,* 1978, *Lutjeharms,* 1981]. This contrasting kinematic behavior is a consequence of the steepness of the continental shelf slope [*De Ruijter et al.,* 1999a]. A very steep slope and narrow continental slope constrains the northern part of the current whereas a more gradual slope along the wider continental shelf south of Africa (the Agulhas Bank) allows more sideways meandering. The exception is a small region of weaker slope along the northern Agulhas Current, at the Natal Bight, where small meanders and accompanying eddies have also been observed [*Gründlingh and Pearce,* 1990] along the edge of the current. Cyclonic eddies are embedded in the landward border of current meanders in the southern Agulhas Current and seem to gain energy from the lateral shear due to the juxtaposition of fast moving water in the current and more sluggish water over the shelf. These cyclonic shear eddies may have a substantial influence on adjacent shelf waters of the Agulhas Bank. They are usually attended by warm plumes drawn from the surface waters of the current [*Harris et al.,* 1978, *Lutjeharms,* 1981, *Schumann and van Heerden,* 1988, *Lutjeharms et al.,* 1989, *Goschen and Schumann, 1990*]. These plumes have in fact been the prime manifestation of shear edge eddies that has been used for their study by thermal infrared sensing from satellite. Depending on the reigning wind conditions, this anomalously warm surface water may then spread over substantial parts of the adjacent shelf [*Lutjeharms et al.,* 1989, *Goschen and Schumann, 1994*]. It has even been surmised [*Swart and Largier,* 1987] that this warm surface water may thus make an important contribution to the intense seasonal thermocline over the eastern part of the Agulhas Bank [*Schumann and Beekman,* 1984]. This hypothesized contribution has as yet not been quantified. Regrettably, few of these shear edge eddies have to date been hydrographically surveyed. A study by Lutjeharms et al. [1989] has used two sets of hydrographic observations as well as satellite imagery to give a general description of these features. More eddies are found the further downstream one measures. In general their lateral dimensions also increase downstream. They seem to be particularly prevalent in the shelf bight on the eastern side of the Agulhas Bank. Judged by the trailing plumes of warm water, they all move downstream, but an insufficient number of time series in the satellite imagery has prevented a statistically reliable propagation speed to be derived. Once past the southern tip of the Agulhas Bank, warm plumes may be advected equatorward into the southern Atlantic Ocean, making a modest contribution to the inter-ocean leakage of heat and salt [*Lutjeharms and Cooper,* 1996]. The fate of the eddies themselves remains unknown. Shear edge eddies my have a diameter of about 50-100 km and are represented by a well-defined thermal dome (figure 3.53-b) inshore of the landward border of the Agulhas Current. This portrayal of these eddies is complicated by the intermittent passage of a Natal Pulse through the region. Natal Pulses are substantial, single meanders in the trajectory of the Agulhas Current [*Lutjeharms and Roberts,* 1988] that are generated by current instability at the Natal Bight [*De Ruijter et al.,* 1999a] and that propagate downstream at a rate of about 20 to 30 km.day^{-1}. When they move past the Agulhas Bank, they seem to slow down to roughly 5

km.day^{-1} [*Lutjeharms and Roberts,* 1988, *Van Leeuwen et al.,* 2000] and become difficult to distinguish from the other meanders normally found here. Like these other meanders, Natal Pulses also incorporate cyclonic eddies [*Gründlingh,* 1979] that move downstream with them. Once past the southernmost tip of the Agulhas Bank, Natal Pulses may trigger the shedding of an Agulhas ring [*Van Leeuwen et al.,* 2000] by loop occlusion at the Agulhas retroflection [*Lutjeharms and van Ballegooyen,* 1988]. The role this process plays in interocean exchanges South of Africa has been extensively reviewed by De Ruijter et al. [1999b] and Lutjeharms [1996]. It is not known what happens to the cyclone that is carried in a Natal Pulse once the meander has passed the tip of the Agulhas Bank. There is evidence that a cyclonic eddy may on occasion be generated in the lee (western side) of the Agulhas Bank by the passing Agulhas Current [*Penven et al.,* accepted] and it has been surmised that the cyclonic eddy that comes with a Natal Pulse may be absorbed by such a lee eddy. Similarly, it has been hypothesized that shear edge eddies may be absorbed by cyclonic eddies in a passing Natal Pulse, thus enhancing it and even contributing to the efficaciousness with which it influences Agulhas ring shedding downstream. The outputs of the high resolution experiment are employed in order to understand the processes involved in the generation and subsequent behavior of shear edge eddies

(a) Simulation of the shear edge features

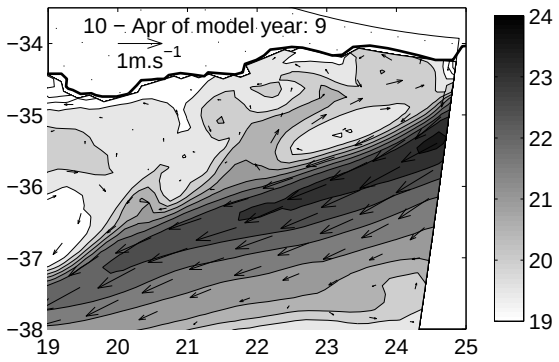

Figure 3.51 Sea surface temperature (^{o}C) and surface currents (m.s^{-1}) over the Agulhas Bank for the 10 April of model year 9. The greyscale range represents the sea surface temperature in ^{o}C. The interval between the isocontours is 0.5 ^{o}C.

The sea surface temperature over the Agulhas Bank for the 10 April of model year 9 is given in figure (3.51). Simulated surface currents are also shown. Temperatures in the core of the Agulhas Current are 23^{o}C and 24 ^{o}C and decrease downstream. Temperatures on the shelf lie between 18 ^{o}C and 20^{o}C . These values are all very representative for these features for this time of year [*Schumann and Beekman,* 1984, *Lutjeharms,* 1996]. The core of the Agulhas Current does not follow the shelf edge very rigorously, but overshoots the bight in the Agulhas Bank at about 23^o E, and eventually crosses the 1000 m isobath at the southernmost tip of the shelf (figure 3.51). Velocities in the current are up to 1 m.s^{-1}; over the Agulhas Bank in general much lower ($<$ 20 cm.s^{-1}). Both these values are very realistic [*Schumann and Perrins,* 1982]. Two surface plumes of warm water at the inshore edge of the Agulhas Current are evident in figure (3.51). A small plume lies at 20^{o}30' E, the larger one starts at 22^o E. The latter represents a fully developed shear edge feature around the concave part of the shelf break with surface counter currents of up to 40 cm.s^{-1}. The implied shear

edge eddy has dimensions of approximately 80 by 150 km. These simulations of the surface characteristics of this region show a high verisimilitude to those evident in figure (3.53-a) and give a most realistic portrayal of the known conditions for the region, i.e. for this time of the year.

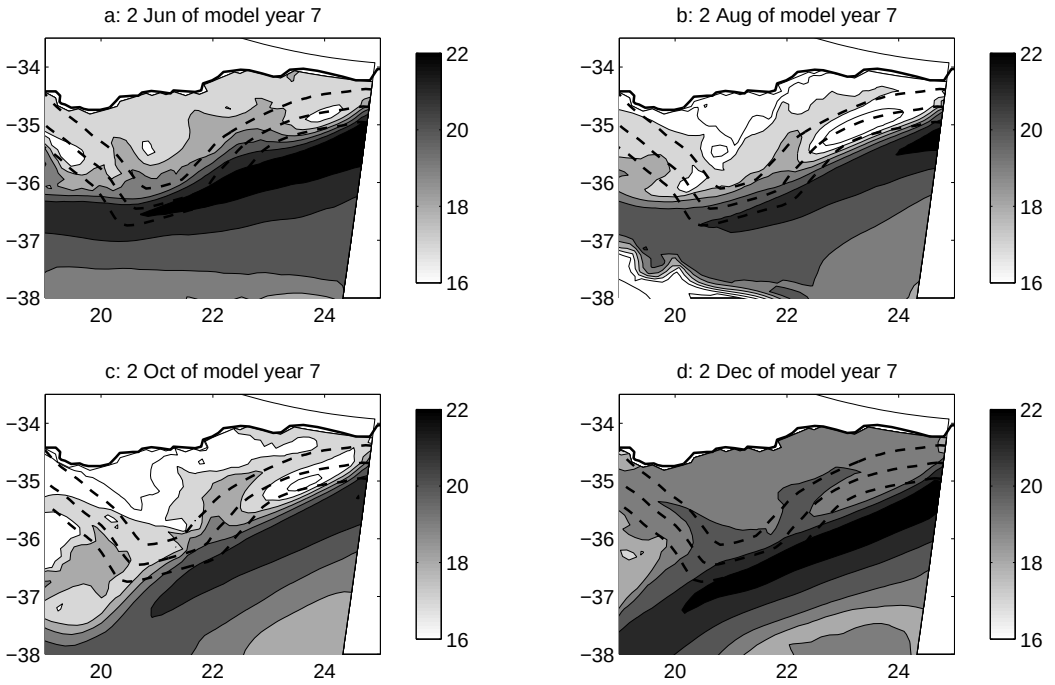

Figure 3.52 The simulated sea surface temperature (^{o}C) for the Agulhas Bank and direct vicinity for a: 2 June, b: 2 August, c: 2 October and d: 2 December of model year 7. The greyscale range represents the sea surface temperature in ^{o}C. The interval between the isocontours is 1 ^{o}C. The dashed lines represent the 200 m, 500 m and 1000 m isobaths.

A portrayal of model results for all seasons of model year 7 is given in figure (3.52). Two aspects of the inter-seasonal variability for the sea surface is immediately apparent. The first is the expected seasonal temperature variations. Both the temperatures in the core of the Agulhas Current and those of the shelf waters exhibit a seasonal cycle of at least 2^{o}C. These values also are realistic [*Christensen,* 1980]. The second thing that is clear is that the location of the simulated Agulhas Current is not entirely stable. This is particularly noticeable downstream of the Agulhas Bank - from June to October the current shifted by at least 240 km. Along the eastern edge of the Agulhas Bank, the meandering of the Agulhas Current is less noticeable, but inspection of its location at about 23^o E in June (figure 3.52-a) and in October (figure 3.52-c) shows a noticeable southward shift. The main shear edge eddy is a recurrent feature of the Agulhas Bank bight, but may lie farther upstream (figure 3.52-a) or downstream (figure 3.52-d). Figures (3.51) and (3.52) therefore demonstrate that the model simulates the known surface conditions very well.

To judge the full effectiveness of the model, one would want to test this in the vertical as well. A vertical section is shown in figure (3.54). The simulated section in this figure is taken across the eastern Agulhas Bank, across a warm plume, a shear edge eddy as well as the landward edge of the Agulhas Current. The location as well as the time of year has been selected to make comparison easier with a hydrographic section taken at this location and portrayed in figure (3.53-b). The main features are represented well, including the thermal

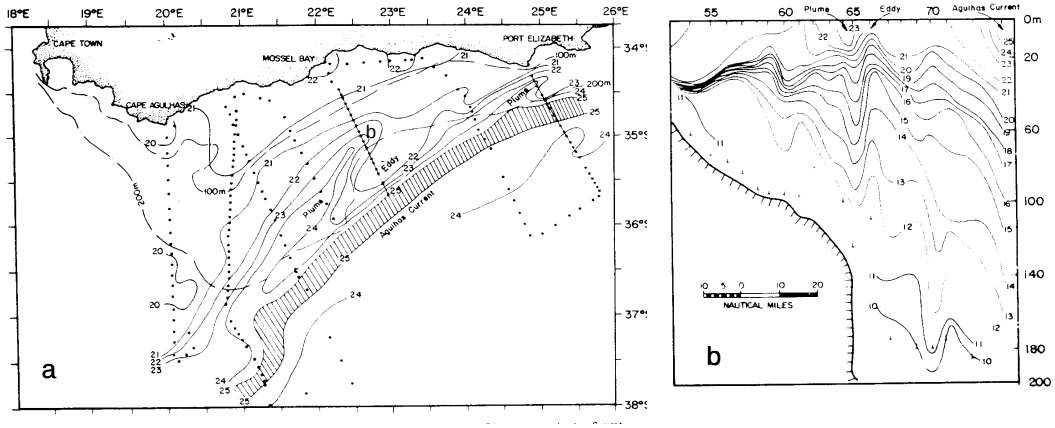

Figure 3.53 a: distribution of temperature (^{o}C) at 10 m over the Agulhas Bank in March 1968. b: Temperature cross section across a border eddy south of Mossel Bay. Adapted from Lutjeharms et al. [1989].

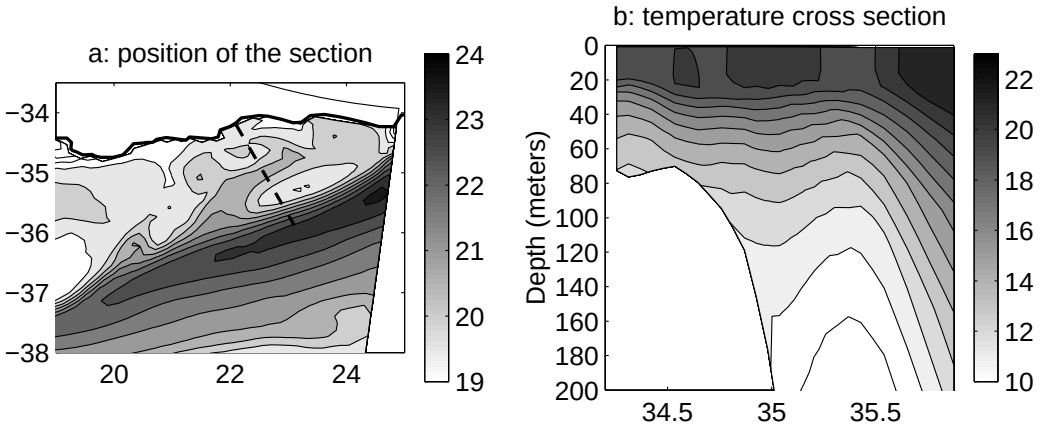

Figure 3.54 a: This panel is identical to that in Figure (3.51). The broken line indicates the location of a simulated vertical section from the land across the shelf and shelf edge an crossing the edge of the Agulhas Current that is given in the right panel. b: A vertical temperature section to 200 m depth along the broken line in the upper panel. Note the warm water of the Agulhas Current, the dome of cold water forming a shear eddy and the plume of warm water extending to a depth of 20 m.

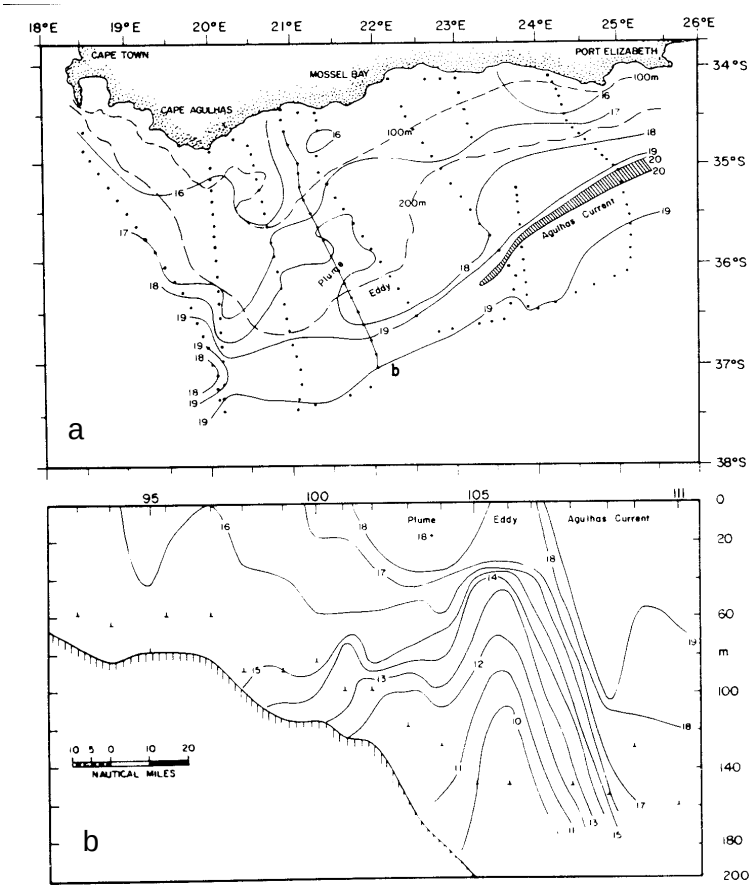

Figure 3.55 a: distribution of temperature (^{o}C) at 10 m over the Agulhas Bank in September 1968. b: Temperature cross section across a border eddy south of Mossel Bay. Adapted from Lutjeharms et al. [1989].

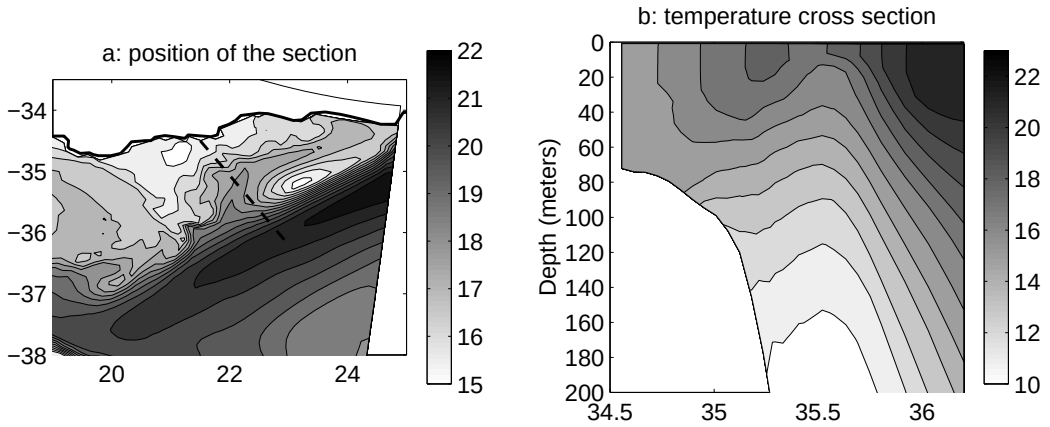

Figure 3.56 a:The sea surface temperature (^{o}C) simulated for 15 September of model year 7. Otherwise as in Figure (3.51). The broken line indicates the location of a simulated vertical section from the land across the shelf and shelf edge an crossing the edge of the Agulhas Current that is given in the right pane. b: potential temperature (^{o}C) vertical section to 200 m along the line.

gradient of the edge of the Agulhas Current, the shape and size of the cold dome representing the eddy as well as the depth and shape of the warm surface plume heading upstream. The plume overlies the landward edge of the eddy, as represented by the strongest horizontal, sub-surface temperature gradient. This corresponds to what has been observed in nature [*Lutjeharms et al.,* 1989]. Even the vertical gradient of the seasonal thermocline over the Agulhas Bank is entirely representative for this time of year [*Lutjeharms et al.,* 1996]. Shear edge eddies are also present in winter as can be seen in figure (3.56) for the model and in figure (3.55) for hydrographic data. For this time of the year, the thermic vertical structure is also remarkably well represented by the model, showing a relatively homogeneous temperature (15^oC) onto the Agulhas Bank (figures 3.56-b and 3.55-b). The sea surface temperature shows the warm plume that rounds the shear edge eddy both in the model (figure 3.56-a) and in the hydrographic data (figure 3.56-a). The reverse plume appears to be further downstream ($\sim$ 100 km) in the hydrographic data than in the model results. At this time of the year, the cold dome happens to be more marked than in summer. Regrettably there are insufficient data on shear edge features of the Agulhas Current to afford more inter-comparisons between the model simulations and actual observations. Nonetheless, those that have been presented here are such that they give us considerable confidence in the reliability of the model.

(b) Evolution of shear edge eddies

A time series for sea surface elevation off the Agulhas Bank and general vicinity is portrayed in figure (3.57). It is given with 8 day intervals, starting on 7 December of model year 7. In the first image (figure 3.57-a) there is a well-developed Agulhas Current with a large cyclonic shear eddy in the eastern bight of the edge of the Agulhas Bank. West of the Agulhas Bank there is a weakly developed anti- cyclone about 250 km in diameter. The presence of an anti-cyclone in this region has been shown to occur at least 12 % of the time [*Lutjeharms and Valentine,* 1988]. The model also shows a small anti-cyclone in the north-easterly corner of the modeled field over the Agulhas Bank. It remains largely unchanged throughout the sequence. We are unsure if it is an artifact of the boundary conditions. A week later (figure 3.57-b), the shear edge eddy has shrunk somewhat in size, having split off a very small eddy that is now moving downstream at about the rate such eddies are known to propagate [*Lutjeharms et al.,* 1989]. The anti-cyclonic eddy had grown somewhat in strength. On the next panel these developments continue (figure 3.57-c). By 1 January (figure 3.57-d) the smaller shear edge eddy has grown in size and has left the eastern shelf edge. The large shear eddy in the bight has again spawned a protrusion, this time considerably bigger. A week later this protrusion has split of as a slightly larger eddy and is moving downstream as did its predecessor. Its predecessor has by now developed into a strong Agulhas Bank lee eddy, characterized by a sea surface height 25 cm lower than its South Atlantic environment. Two weeks later (figure 3.57-g) the second shear edge eddy had been absorbed into this lee eddy, had strengthened it to a 30 cm anomaly, and the lee eddy can be seen moving away into the South Atlantic Ocean [*Penven et al.,* accepted]. Such cyclones have been observed in this region in altimetry [*Gründlingh,* 1995] and from hydrographical measurements [*C. Veth, S. Drijfhout,* personal communication]. They have on occasion been traced in altimetry to this location that is associated with a lee eddy. On the last panel of this sequence (figure 3.57-h) the lee eddy has moved totally eastward and the main shear edge eddy is producing another downstream protrusion. Note that the downstream leakage from this main shear eddy is always associated with a slight offshore meander in the Agulhas Current trajectory.

These images are a piecemeal selection from a more detailed series. This process can

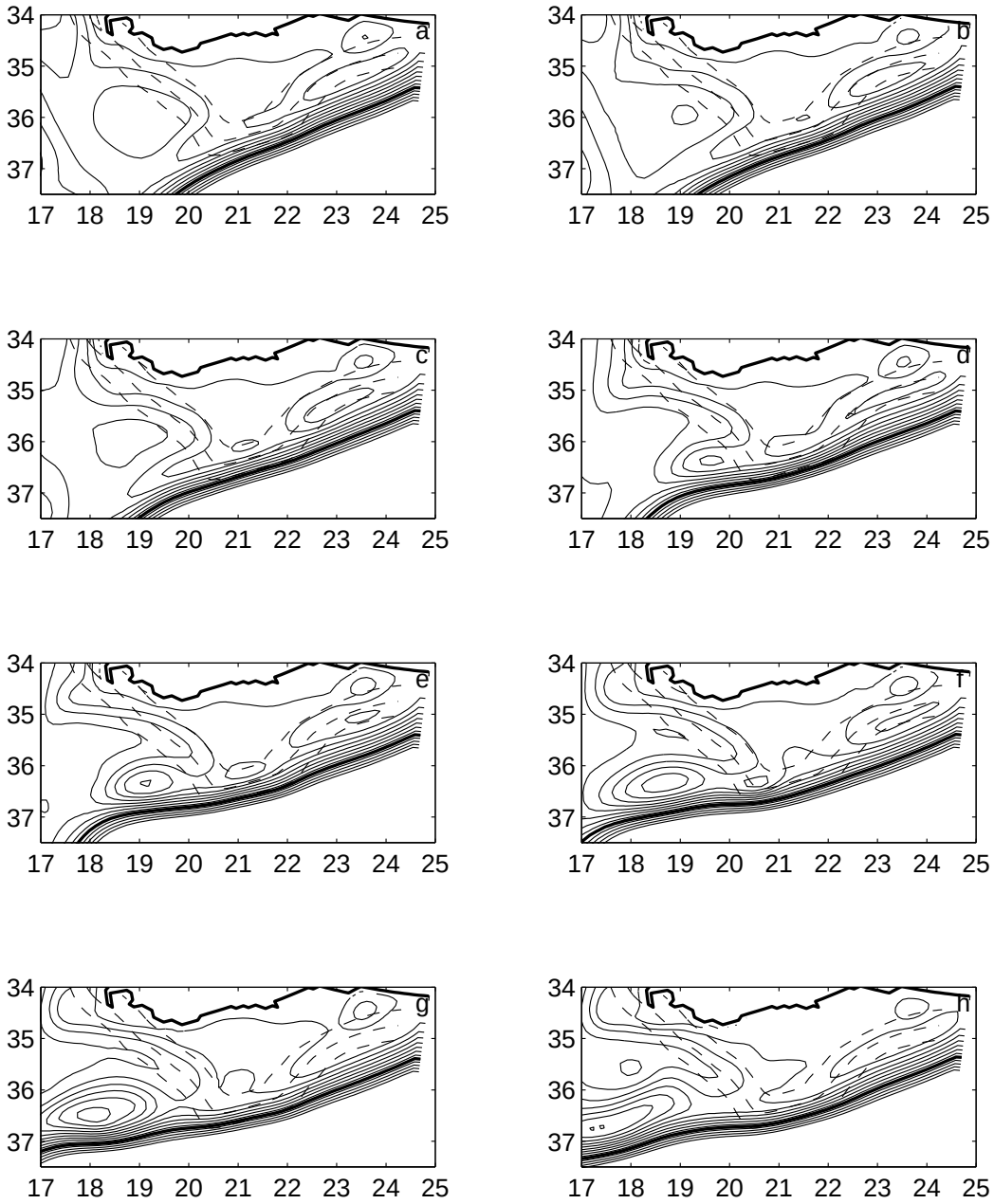

Figure 3.57 The simulated evolution of shear edge eddies along the eastern side of the Agulhas Bank. The broken lines denote the 200 m, 500 m and 1000 m isobaths. Shown is the sea surface height (contour lines from -60 to 20 cm, the latter being the value south of the Agulhas Current). The interval between the isocontours is 5 cm. The dates are a: 7 December of model year 7, b: 15 December 7, c: 23 December 7, d: 1 January 8, e: 7 January 8, f: 15 January 8, g: 23 January 8 and h: 1 February 8.

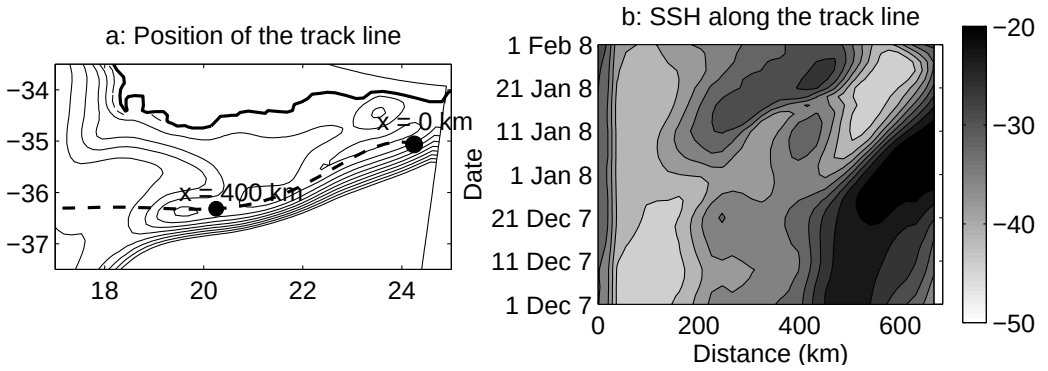

Figure 3.58 Tracking the westward leakage of cyclonic vorticity in the form of a bud-off eddy. The left panel (a) depicts the sea surface height (5 cm between the isocontours). Note the cores of the shear edge eddy between 23^{o}E and 24^{o}E and the Agulhas Bank lee eddy between 18^{o}E and 19^{o}E. The broken line is used to track the movement of water with a cyclonic motion (low sea surface height). The Hovmüller diagram on right panel (b) shows the movement in time (increasing upward on the ordinate). The distance on the abscissa is from the easternmost point on the solid line in the upper panel, i.e. x=0 is at 24.25 E and 35 S; the distances on the abscissa are positive traveling westward. The interval between the isocontours is 3 cm.

therefore be shown with considerably better temporal resolution (figure 3.58). The left panel shows the setting for this region with the thick broken line indicating the path along which the sea surface elevation will be followed (figure 3.58-a). In figure(3.58-b), clear greyscale shows low sea surface deepening in comparison to the surroundings, thus cyclonic motion. Hence, the displacement of cyclonic shear edge eddy and the lee eddy can be followed along the broken line by looking at low sea surface height values. The Hovmüller diagram in the right panel (figure 3.58-b) shows the development over time, starting at the bottom and moving upward. Note that the direction is not the same as in the left panel (figure 3.58-a), but has been inverted. Starting from 1 December of model year 7 (see figure 3.57-a) there is a well-developed shear edge eddy at 100 km and an anticyclone at 500 km, i.e. in the lee of the Agulhas Bank. The subsequent leakage of cyclonic eddies from the shear edge eddy to the lee of the bank is shown most clearly by the clear track from the left-hand side of the panel to the right-hand side starting on 1 January and ending at 450 km distance on 20 January. On the first part of its trip, the shear edge eddy travels along the line at approximately 6 km.day^{-1}. On the 15 January, at the Southern tip of the Agulhas Bank (x = 350 km), it accelerates up to 32 km.day^{-1}. On the 20 January, it is absorbed into by a larger cyclonic eddy developing in the lee of the Agulhas Bank [*Penven et al.*, accepted] The replacement of an anti-cyclone by a cyclone in the lee of the Agulhas Bank is represented by the change from dark to clear at 500 km distance along the line on about 1 January of model year 8. These simulations leave one with the impression that it is the Agulhas Current that sequesters the shear edge eddy in the eastern bight of the Agulhas Bank and, when it meanders, allows a certain part of the eddy to escape. The cyclonic vorticity of this propagating eddy may then be taken up by a lee eddy. How does this scenario compare to what has been observed at sea? Satellite imagery for the region shows that warm plumes, assumed to be associated with shear edge eddies, consistently exhibit a downstream motion. A plume might of course be associated either with an independent, separated eddy or with the leading edge of a protrusion from a shear eddy trapped in the eastern bight. Therefore both possibilities remain open:

there may be distinct eddies moving downstream, or occasional protrusions still attached to a trapped eddy. Statistically, the bight is known for the prevalence of shear edge eddies [*Lutjeharms et al.*, 1989] so that the concept of a near-stationary, but leaky, eddy at this location is not inconsistent with the data. However, with very limited data it cannot be confirmed in a rigorous manner at present. If this single simulation of the evolution of shear edge eddies at the Agulhas Current edge seems reasonably sound, how representative is it of other such sequences in the model?

(c) Interannual variation in eddy evolution

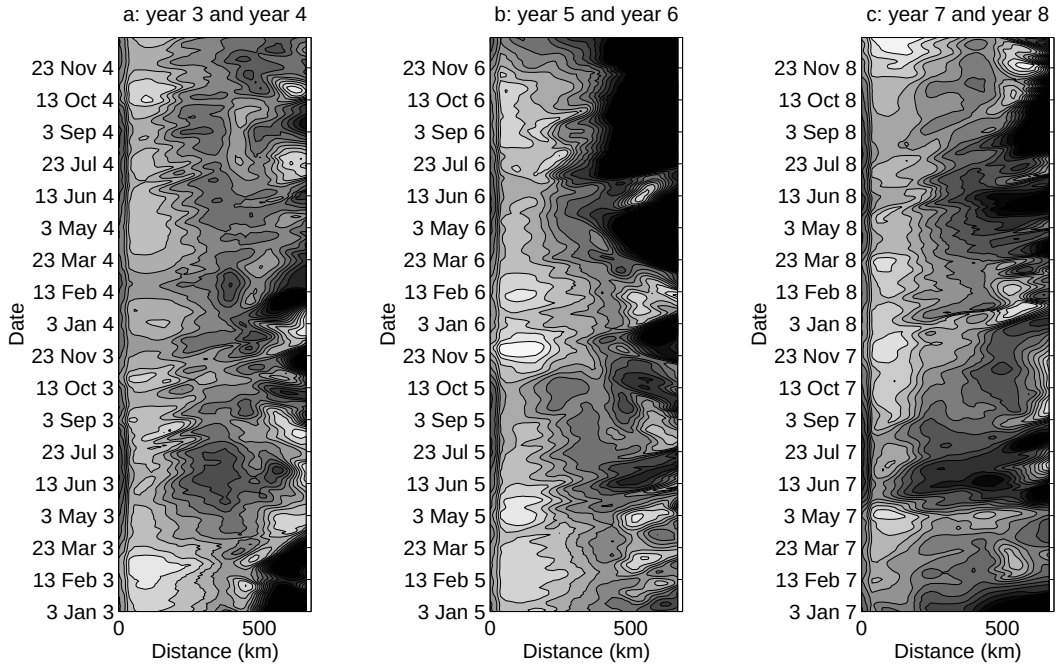

Figure 3.59 Hovmüller diagrams of simulations of the temporal behavior of circulatory features along the Agulhas Bank. The sea surface elevation along the line defined on Figure (3.58-a). The interval between the isocontours is 3 cm. The left panel (a) represents model years 3 to 4, the central panel (b) years 5 to 6 and the right hand panel (c) years 7 to 8. Otherwise the images are identical to that of the lower panel of Figure 7.

The simulated behavior of shear edge eddies along the edge of the Agulhas Bank for a 6-year period in the model run is presented in figure (3.59). Except for the extended periods the portrayal is identical to that of figure (3.58-b). The sea surface height is tracked along the line used in figure (3.58-b). A number of notable features are immediately apparent. First, their is considerable inter-annual and intra-annual variation, generated by the internal physics of the model itself. In this depiction, the center of the trapped shear eddy is located at a distance of 100 km in figure (3.59). This location seems to be relatively invariant, but the dimensions and intensity of the eddy varies considerably with time. There are events lasting about 6 weeks when it is particularly well-developed (e.g. November year January year 6, figure 3.59-b), and longer periods when is seems very weak or totally absent. The absence of a trapped shear eddy seems to coincide roughly with the presence of the Agulhas Current closer inshore. This movement of the current is reflected by the appearance of sea surface height elevations at a distance of about 300 km along the track and a simul-

taneous sea level enhancement in the far eastern part of the domain (left side of columns in Figure 8). On June of model year 7 (figure 3.59-c) these two regions of higher sea level nearly touched, showing strong perturbations in the large scale currents. At the western-most part of the field (right side of columns in figure 3.59) marked positive and negative departures from the mean sea surface height show the spasmodic exchange of a cyclonic and an anticyclonic motion. This may be interpreted as the replacement of a northward meander in the simulated Agulhas Current with a cyclonic lee eddy (e.g. May year 3, figure 3.59-a). Perhaps of most interest is the clear signs of intermittent but frequent leakage of cyclonic motion (figure 3.59-b) from the upstream region to the downstream region. These are shown as feint clear lines from left to right in the columns of figure 3.59. More marked eddy leakage can be observed on Mars 3, September 3, June 4, September 5, December 5, September 6, May 7, December 7, September 8 (figure 3.59). They indicate that these eddies that carry cyclonic motion downstream propagate at roughly 8 km.day^{-1}, very close to estimates made from satellite imagery [*Harris et al.,* 1978, *Lutjeharms et al.,* 1989] for shear edge eddy progression and even for the movement of Natal Pulses along the Agulhas Bank [*Lutjeharms and Roberts,* 1988, *Van Leeuwen et al.,* 2000]. The frequency with which there is a movement of from the trapped shear eddy downstream seems to have some regularity if not affected by the large scale movement of the Agulhas Current (e.g. March to November of year 4; figure 3.59-a). The spawning of a traveling eddy seems to occur at intervals of roughly 20 days in the model. Observations to date are insufficient to validate this, mostly due to interference to the satellite thermal infrared measurements by cloud cover. However, indications are of a considerably more irregular process.

(d) Shear edge eddy trapping by topography

The strong indication by the model that a shear eddy will get trapped in the bight of the shelf and that this is largely determined by the interaction of the Agulhas Current with the topography of the bight is tested in this section by a set of idealized numerical experiments. The bight that lies at the eastern side of the Agulhas Bank around 23^o E, is characterized by the bend toward shore of the 500 m isobath, the isobaths deeper than 1500 m running quasi rectilinearly South-westward. This creates an embayment of about 200 km long and 100 km wide. The goal of this section is to show that the interaction between a density driven current with a topographic accident such as the Agulhas Bight is able to generate a standing recirculation process identical to the large shear edge eddy observed in the realistic experiments.

The ROMS model has been configured as follows:

- The grid is regular and isotropic ($\Delta x = \Delta y = 10$ km). The length of the domain is 700 km in the x direction and the width is 300 km in the y direction.

- For the sake of simplicity, the model domain consists of a periodic channel along the x direction.

- The bottom topography is defined analytically and is periodic to satisfy mass conservation in the periodic channel. Figure (3.60-a) represents the bottom topography employed. It consists of a large shelf ending on a slope. A perturbation of the slope in the middle of the domain account for the Agulhas Bight.

- In the vertical, 20 s-levels are evenly distributed.

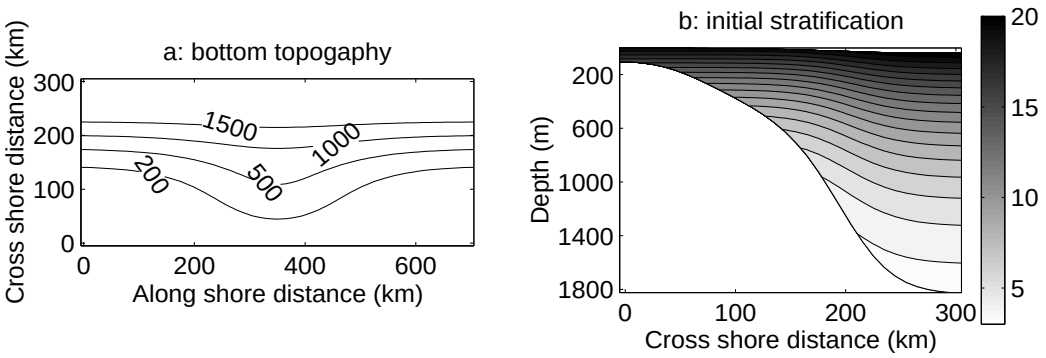

Figure 3.60 a: bathymetry (m) employed for an idealized model of the circulation along an indentation in a shelf slope. b: The vertical potential temperature (^{o}C) distribution used for initial and boundary conditions, on a section from the coast to the deep ocean.

- The equation of state takes a linear form depending solely on temperature: $\rho = 1025 - 0.28\times$T.
- All the surface fluxes are set to zero (no wind stress, no heat flux)
- No bottom flux for temperature and linear parameterization for the bottom momentum flux: $\kappa\frac{\partial u}{\partial z}|_{z=-h} = -ru, \quad r = 3\times 10^{-4}$ m.s^{-1}.
- The vertical mixing coefficient for momentum and temperature are constant: $\kappa_M = 10^{-3}$ m^2.s^{-1}, $\kappa_T = 10^{-5}$ m^2.s^{-1}.
- Figure (3.60-b) shows the cross section of the analytical function employed for the temperature initial condition. It reproduces a typical cross section across the Agulhas Current. The velocity and free surface elevation are set to zero at the model start.
- The temperature is relaxed towards its initial value with a nudging time of 5 days during all the simulation.
- The Coriolis parameter f is constant equal -10^{-4}. The β related processes are not taken into account.

After 60 days of simulation, the model has reached a steady state where the along shore velocities have been adjusted to the stratification. The resulting surface current attains values of 90 cm.s^{-1} above the 1000 m isobath. The width of the current ranges between 50 and 100 km. We are in the parameter range of the Agulhas Current. The resulting free surface elevation is portrayed on figure (3.61-a). Its slope represents the along shore geostrophic surface currents. Although the temperature is constrained to remain close to its initial value, the free surface elevation reveals that a cyclonic recirculation stands in the bight. Hence, this simulation shows that the interaction between the Agulhas Current and the topography of the bight is likely to generate a cyclonic eddy. To test if the recirculation might be induced by an advection process, the same experiment has been conducted, removing the advective terms from the different prognostic equations. After 60 days, the figure (3.61-b) represents the resulting sea surface elevation. The along shore currents have roughly the same characteristics as the previous experiment. Surprisingly, the cyclonic recirculation has grown in size and intensity. It tends to propagate towards x negative, as a coastal trapped wave, but the nudging of temperature retains it close to the bight. Hence, the resulting shape of the recirculation is

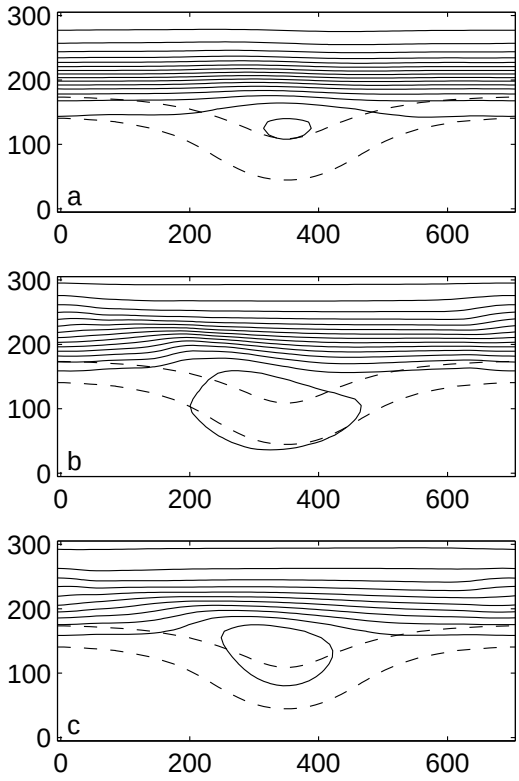

Figure 3.61 Sea surface height (5 cm interval) after 60 model days. The currents have been adjusted with the density structure. In the upper panel (a) advective terms and bottom friction have been retained, in b there is no advection of momentum and in c both the advection of momentum and the bottom friction have been left out.

distorted. This reveals that whereas the advection doesn't seems to be the driving mechanism of the recirculation in the bight, its alongshore component can help to obtain a standing process. Bottom friction can be a serious candidate for driving this process. The model of the arrested topographic wave [*Csanady,* 1978], can explain the crossing of the isobaths by a barotropic current. A last experiment has been conducted, removing this time the advection terms and the bottom friction. Without the damping effect of the bottom friction, the solution was not stationary after 60 days. The resulting free surface elevation (figure 3.61-c) is less steep than for the previous experiments. Nevertheless, the cyclonic pattern is larger and more intense than for the first case. This implies that whereas bottom friction plays an important contribution during the adjustment of the current to the density field in this simulation, it is not responsible of the cyclonic recirculation.

(e) Summary

The realistic model simulates the creation of cyclonic shear edge eddies and their attendant surface plumes of warm water with a high degree of verisimilitude. The dimensions of the features, their hydrographic structure and geostrophic velocities in the model bear a strong resemblance to what has been observed. The model shows that a shear edge eddy remains trapped in the bight on the eastern side of the shelf break of the Agulhas Bank and that eddies that travel downstream represent leakages from this resident shear eddy. This is not inconsistent with observations to date, but cannot be unambiguously verified. Although the current axis shows some degree of meandering in the model, this is much less than in nature, suggesting that much larger parts - or even the full - trapped eddy might occasionally escape and move downstream. Once they reach the southernmost tip of the Agulhas Bank, the traveling eddies may be absorbed by a cyclonic eddy in the western lee of the bank or may start such an eddy. The model does not indicate unequivocally whether such absorption has an effect on the timing of the eastward departure of the lee eddy. An idealized model of a baroclinic current along an indented shelf edge shows the development of a trapped shear edge eddy. If the advection of momentum is excluded, the cyclonic eddy tends to propagates along shore as a coastal trapped wave. If bottom friction is removed, the solution is no longer stationary. This eliminates two candidates for the generation process of a standing cyclonic eddy in the bight.

3.5.7 Transport patterns from the Agulhas Bank to the South African West Coast

The previous sections validate the results of the realistic simulation of the circulation around the South-western corner of Africa. These results can now be utilized to study the physical processes affecting the recruitment of pelagics in the Benguela upwelling system.

The spawning of sardines and anchovies occurs essentially during the austral spring and fall. The wind induced mixing and the Ekman transport of the coastal waters towards the deep Ocean are unfavorable for the reproduction along the West coast. To reproduce, sardines and anchovies spawn onto the Agulhas Bank. After a few days, eggs and larvae reach the upwelling system of the South African West Coast. A few months after spawning, an important biomass of young recruits concentrate in St Helena Bay. Hutchings [1992] identified the key processes for the recruitment of sardines and anchovies in the Southern Benguela:

(1) Feeding of the adults during the spawning on the Agulhas Bank.

(2) Feeding of the larvae.

(3) Transport of the eggs and larvae from the Agulhas Bank to the Benguela upwelling system.

(4) Migration and retention of the larvae in the Coastal productive area.

(5) Feeding of young recruits.

If we consider that the swimming capabilities of the larvae are limited in comparison to the magnitude of the surrounding currents, the points 3 and 4 involve principally physical processes of transport from the Agulhas Bank to the South African West Coast, dispersion, offshore Ekman transport and retention at the coast.

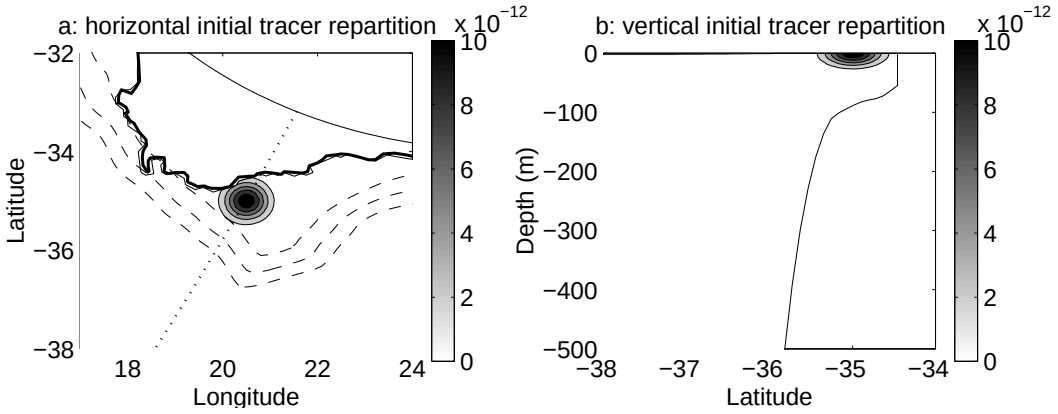

Figure 3.62 Initial condition for the tracer. a: horizontal repartition. b: vertical repartition.

In order to explore these physical processes of transport and dispersion, short term simulations has been conducted, starting from different moments of the long term simulation, in which a passive tracer, representing the probability of presence of an egg, has been introduced into the model. At the beginning of each short term simulation, the initial value of the tracer 'egg' is defined as a tridimentional Gaussian patch (figure 3.62):

$$T_{egg} = C_0\, e^{-\left(\frac{R_{Earth}}{40}\frac{\pi}{180}(\Phi-\Phi_0)\right)^2} e^{-\left(\frac{R_{Earth}}{40}\frac{\pi}{180}\cos\frac{\pi\Phi}{180}(G-G_0)\right)^2} e^{-\left(\frac{z}{20}\right)^2} \tag{3.48}$$

Where R_{Earth} is the radius of the Earth in km, Φ is the latitude, Φ_0 is the latitude of the center of the patch, G is the longitude, G_0 is the longitude of the center of the patch, z is the vertical coordinate in m, and C_0 is a coefficient set up to obtain $\iiint_V T_{egg}\, dv = 1$. Hence, only 1 egg is injected into the model at the beginning of each simulation, with a Gaussian probability of presence to be in a circle of 40 km radius centered at Φ_0 and G_0, in the 20 first meters from the surface. For these simulations, the initial patch is centered at $\Phi_0 = 35^o$ S and $G_0 = 20.5^o$ E accounting for an egg spawned on the spawning ground of the western Agulhas Bank (see Hutchings [1992]). This initial patch is portrayed on figure (3.62). During the simulation the tracer 'egg' is forced by the advective and the vertical mixing schemes of the model, employing the coefficient of vertical mixing of momentum. The open boundaries for this tracer are passive and radiative to allow its evacuation from the model domain. After the tracer release, the short term experiments are conducted for 3 months to include all the whole egg and larvae states for sardines and anchovies. After the larvae state, the swimming capabilities of the fishes invalidate the use of a passive tracer to simulate their behavior.

The impact of the wind forcing of the transport patterns from the Agulhas Bank to the Benguela upwelling system is studied by releasing the tracer 'egg' each month of the summer

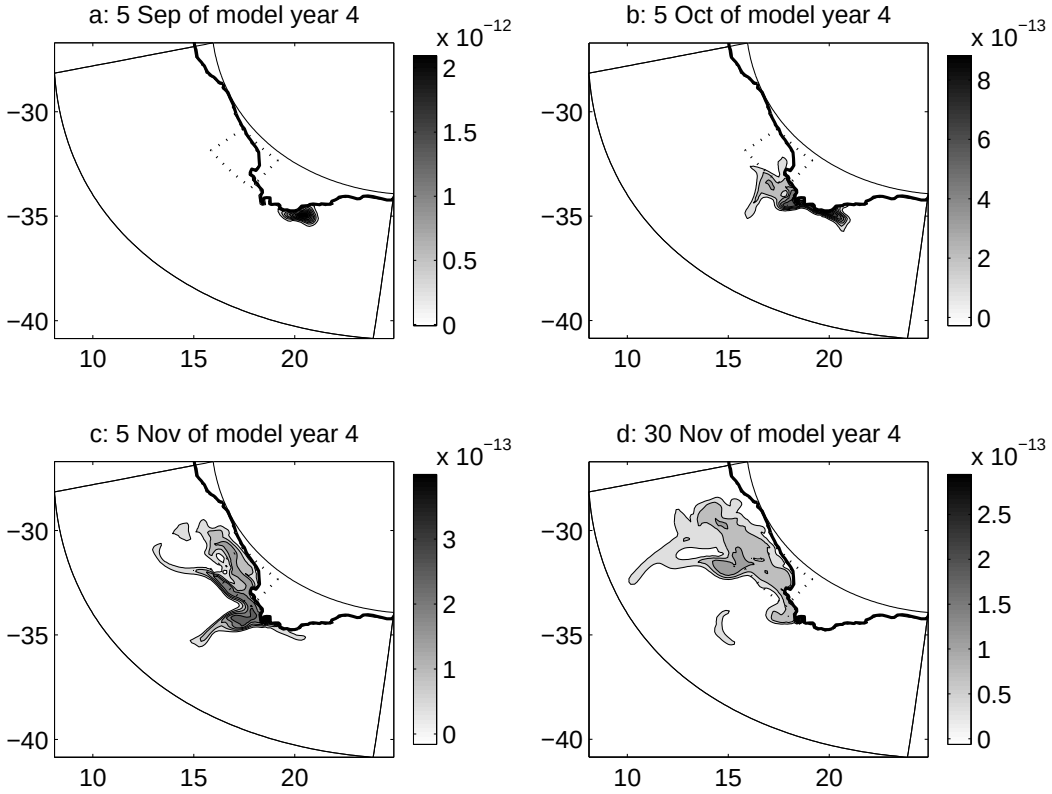

Figure 3.63 Time series of the tracer surface concentration for an egg released the 1 September of model year 4. a: after 5 days. b: after 35 days. c: after 65 days. d: after 90 days.

period, for the low and high resolution experiments, from September of model year 4 to April of model year 5. A time series of the surface tracer behavior for a release just before the upwelling season, the 1 September of model year 4 for the high resolution experiment is portrayed on figure (3.63). Because of the important vertical mixing present in the surface mixed layer, the surface distribution of the tracer is representative of the horizontal repartition for all the mixed layer. The averaged wind stress for this period of 3 months is around 0.075 $N.m^{-2}$, starting at 0.049 $N.m^{-2}$ for September and finishing at 0.088 $N.m^{-2}$ for the end of November. After 5 days, the tracer didn't moved considerably, sticking to the coast near Cape Agulhas (figure 3.63-a). After 1 month, a portion of the tracer reaches Cape Columbine, but the core of the patch stays near Cape Peninsula. For this period, the patch didn't disperse considerably (figure 3.63-b). At the beginning of November (figure 3.63-c), the patch has separated into 3 tongues: 1 extending from Cape Peninsula due to the presence of an upwelling filament, 1 following the shelf edge jet from Cape Columbine, and 1 filling St Helena Bay. At the end of November, the probability of presence of the egg is approximately uniformly distributed on the shelf along the west coast (figure 3.63-d).

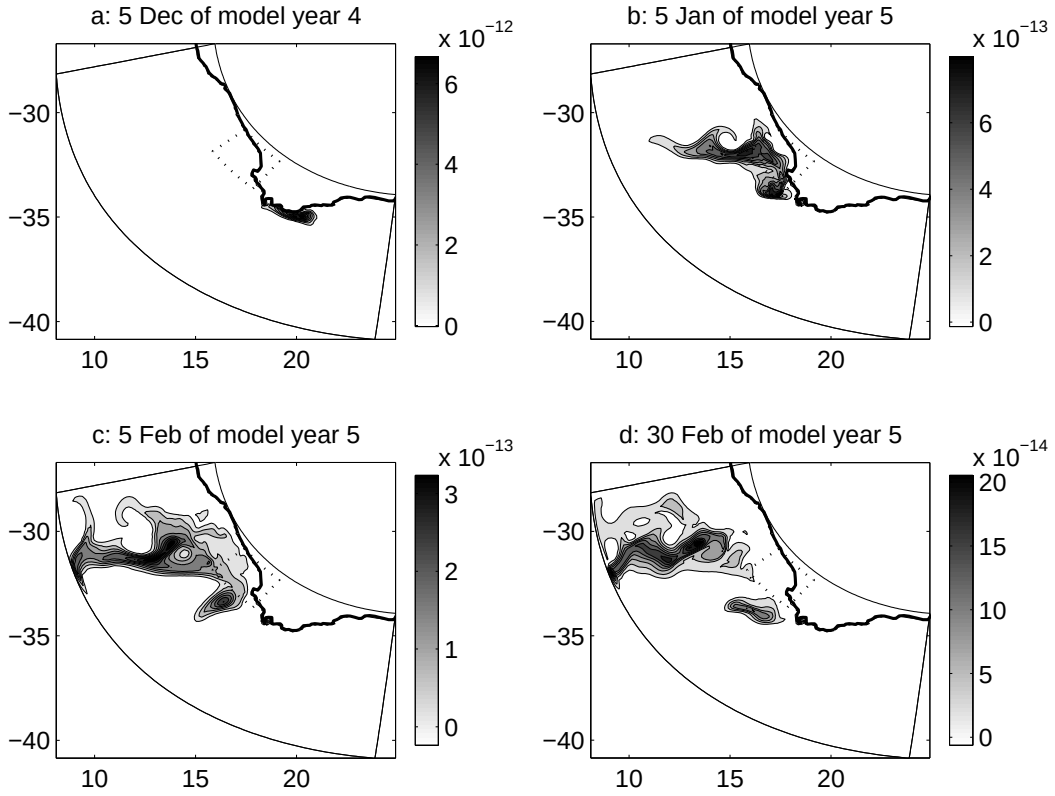

Figure 3.64 Time series of the tracer surface concentration for an egg released the 1 December of model year 4. a: after 5 days. b: after 35 days. c: after 65 days. d: after 90 days.

Figure (3.64) represents the time series of the tracer evolution for an egg spawned in the middle of the upwelling season, the 1 December of model year 4. For this period, the averaged wind stress is 0.085 $N.m^{-2}$, starting in the beginning of December at 0.088 $N.m^{-2}$ and ending at the end of February at 0.075 $N.m^{-2}$. For this simulation, things are going quickly. After 5 days, the Northern part of the patch has already reached Cape Peninsula (figure 3.64-a). After 1 month, the all of the tracer patch has passed Cape Peninsula, the effect of the offshore Ekman transport is important with the major part of tracer heading north-westward, away

from the West Coast. A secondary maximum of tracer concentration is trapped around 34^o S and 17^o E, inside a cyclonic eddy shed from Cape Peninsula (figure 3.64-b). The effect of the offshore transport is dramatic after 2 months, for the beginning of February (figure 3.64-c), the largest concentration of tracer is now situated more than 400 km offshore from the coast. After 3 months, there is almost no chance for a passive larvae issued from an egg released in December to remain on the shelf along the West Coast (figure 3.64-d).

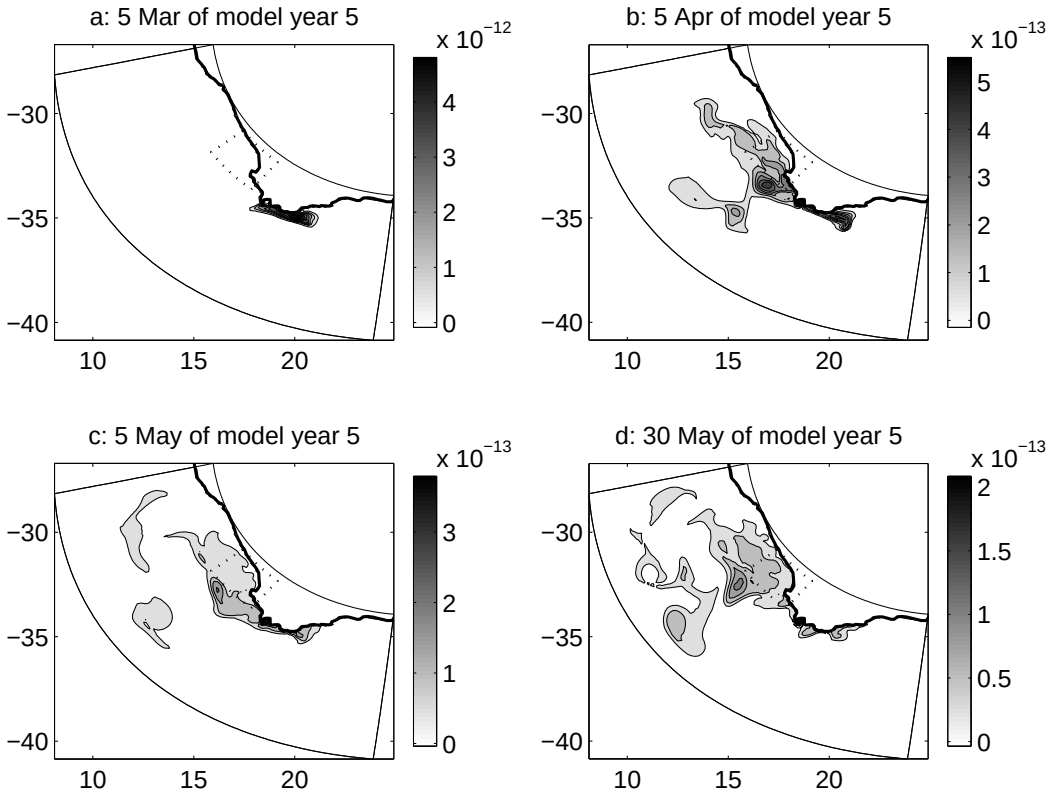

Figure 3.65 Time series of the tracer surface concentration for an egg released the 1 March of model year 5. a: after 5 days. b: after 35 days. c: after 65 days. d: after 90 days.

For the last time series, the egg is released at the end of the upwelling season, the 1 March of model year 5. The averaged wind stress along the 3 months of simulation is 0.045 N.m^{-2}, starting at 0.075 N.m^{-2} for the beginning of March and ending at 0.028 N.m^{-2} for the end of May. The displacement start quickly. After 5 days (figure 3.65-a), the pattern is similar as the previous time series (figure 3.64-a). After 1 month (figure 3.65-b), an important portion of the tracer is already present in St Helena Bay. There are also 2 patches of tracer that are trapped into cyclonic eddies generated from the Cape Peninsula-Cape Columbine area. For the beginning of May, the dispersion has slowed down with the diminishing wind stress and few variations are present between the last 2 months (figures 3.65-c and 3.65-d). After 3 months, the tracer distribution is approximately equivalent to the end of the case for the release in September (figure 3.63-d).

To quantify the probability for an egg spawned on the Western Agulhas Bank to reach the nursery ground of St Helena Bay, time series of the tracer integrated on the volume limited by the dashed line on figure (3.65) has been portrayed on figure (3.66). This integrated value accounts for the probability of the presence in the nursery ground of St Helena Bay of an egg spawned on the Western Agulhas Bank. For the low resolution experiments, the pattern is

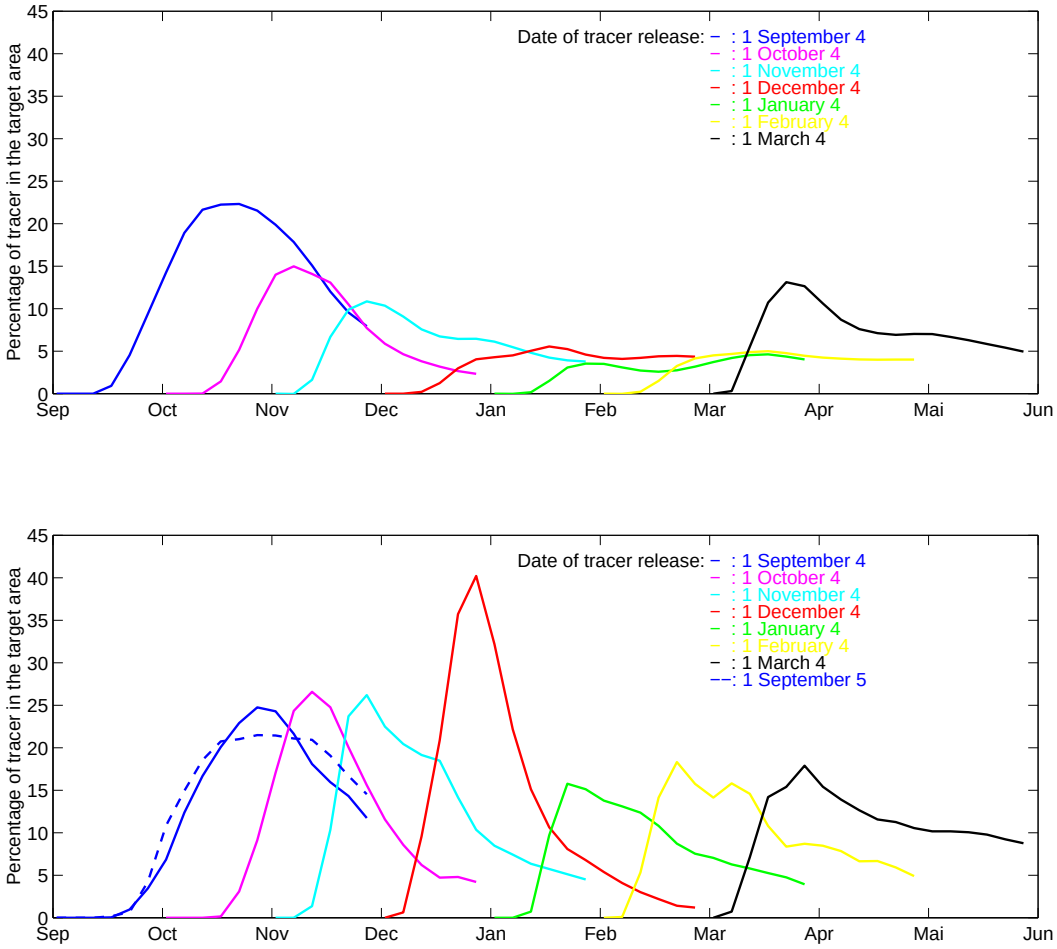

Figure 3.66 Time series of the tracer concentration integrated on the volume of the target zone, in percentage of the total amount of tracer released. Top: for the low resolution experiment. Bottom: for the high resolution experiment.

clear (figure 3.66-top). The probability of an egg to reach St Helena Bay is maximum (almost 25 % chance) if it is released before the upwelling season. This maximum occurs after around 45 days. The more we advance in the upwelling season, the more the offshore Ekman transport is active, and the less the eggs have a chance (only 5 % for January) to reach the nursery ground. The chance increases again at the end of the upwelling season. The time series for the high resolution experiment follows a more complex pattern (figure 3.66-bottom). For a release in September the percentage of tracer in the target area follows approximately the same curve as for the low resolution experiment. For October and November, the maximum is the same as for September, but the tracer arrives more rapidly in St. Helena Bay. The tracer is also washed out more quickly from the bay, as we advance in the upwelling season. For the release in December, the curve differs dramatically from the low resolution experiment, showing an important amount of tracer entering the zone in less than a month and leaving the area in also less than a month. Figure (3.64-b) reveals that this narrow maximum of tracer in St Helena Bay can be associated with the crossing of the area by a patch of tracer trapped in a small eddy. This shows that the mesoscale activity alters considerably the transport pattern from the Agulhas Bank to St Helena Bay. For the releases of January, February and March, the amount of tracer in St. Helena Bay follows a relatively constant pattern: rapid increase to reach a maximum of 15 % after less than 1 month and slow decrease. The impact of the interannual variability observed in the outputs of the high resolution experiment is tested for the transport of eggs by making the comparison between an experiment for an egg released the 1 September of model year 5 and the experiment for an egged release the 1 September of model year 4. The dashed line on figure (3.66) reveals that although a certain degree of interannual variability is present in the model outputs, the global transport patterns do not differ dramatically from one year to the other. This allows sardines and anchovies to adapt their reproductive strategies to these relatively stable global transport patterns. One can note that differences in the transport behavior between the low resolution and the high resolution experiments occur principally during the upwelling season, when the mesoscale activity along the west coast is the strongest. This result connects to the conclusion of the second chapter that shows that during the upwelling season, although the Ekman transport can carry the material away from the coast, eddies can trap it for a certain amount of time in the coastal domain.

3.6 Summary

In this chapter, a primitive equation model, the Regional Oceanic Model Systems, has been configured to reproduce the characteristic patterns of the circulation around the South-western corner of Africa. The model resolves the free surface, hydrostatic, tri-dimensional primitive equations featuring high order schemes and new parameterizations over variable topography using stretched, terrain following coordinates. The horizontal, orthogonal, curvilinear grid has been designed in a pie shape to fit the curve of the South African coastline. Specific open boundary conditions involving a radiative one way nesting of seasonal time averaged data from a large scale oceanic model allow long term stable simulations. Two configurations are set up: a low resolution one with a grid space ranging from 18 km to 31 km and a high resolution one with a grid space ranging from 9 km to 16 km. The surface fluxes are derived from the coarse monthly climatology of the COADS dataset.

After a spin-up of 2 years, the model has reached a statistical equilibrium. The high resolution experiment produces important intrinsic instabilities associated with the upwelling process and the Agulhas Current dynamics, with formation of plumes, filaments and eddies.

For the low resolution experiment, whereas on a large scale the time averaged circulation, temperature and salinity compares to the observations, some aspects of the solution such as the Agulhas Current retroflection or the coastal circulation are not correctly represented. In the high resolution case, the solution is much more satisfactory and compares quantitatively to the known circulation. The volume averaged level of kinetic energy is higher than for the low resolution experiment due to the better resolved mesoscale processes. The averaged position of the retroflection of the Agulhas Current now corresponds to the observations, and important aspects of the coastal circulation such as the coastal jets are now properly resolved. The signature of the Agulhas Current is still present at 1000 m depth. At this depth and below, the circulation in the Benguela is slow, meandering and principally poleward. The depth integrated transport for the Benguela is ranging from 10 to 20 Sv and is more than 60 Sv for the Agulhas Current, in agreement with previous studies. The time averaged sea surface temperature compares quantitatively to satellite data. The principal difference is the stronger upwelling observed in the model outputs. This can be related to the low resolution dataset employed for the wind forcing. The bottom temperature and salinity values stay in reasonable agreement with long term observations.

The length of the experiment allows a statistic analysis of the variability. The sea surface temperature variance shows a maximum on the Agulhas Bank where the currents are weak and a minimum in St Helena Bay where the presence of the upwelling plume seems to balance the seasonal variations. This pattern is quantitatively confirmed by sea surface satellite data. The root mean square of sea surface height is compared to altimeter data. It reveals both in model and data a maximum in variability in the Agulhas retroflection area and minimums on the shelves along the South and the West coasts. The same pattern is observed from the subsurface eddy kinetic energy. Although the modelized EKE compares quantitatively to data north of 35^o S, where the variability is produced in-situ, an important difference is noticeable in the area influenced by the Agulhas Current. This discrepancy can be explained by the smooth time averaged data used to generate the Agulhas current at the Eastern boundary and by the constrain generated by the western boundary on the spawning off the Agulhas rings. This difference is confirmed by the ellipses of subsurface velocity variance. They also reveals an important anisotropy of the variability near Cape Columbine, near Cape Peninsula and South of the Agulhas Bank. These area of anisotropy in variability are also the preferred area for eddy generation. Important anisotropy in variability is also present along the open boundaries which tend to minimize the cross boundary variability.

Although the wind forcing is coarse in space and time, the modelized upwelling system of the west coast shows important features such as the upwelling plume of Cape Columbine, the Namaqualand upwelling center, the upwelling eddies generated by the major capes, and the filaments spreading from the main upwelling front. This shows that the temporal and spatial small scale structures of the wind field are not the primary generators of the mesoscale activity of the upwelling system. It is rather induced by intrinsic instability processes. On the shelves, the time averaged circulation is highly controlled by the topography. A part of the Agulhas Current tends to follow the western part of the Agulhas Bank to feed the Good Hope jet. A surface equatorward baroclinic jet follows the shelf edge and a poleward undercurrent flows along the shelf break. The subsurface coastal counter current is present in the high resolution simulation. Standing coastal wave patterns can be noticed in St Helena Bay, in agreement with the analysis of the second chapter, but the treatment of the topography induces a steepening of the shelf, inhibiting the generation of a cyclonic mean circulation in the bay.

Mesoscale processes in association to the Agulhas Current are also simulated by the model. They include:

- Cyclonic eddies that are shed from the southern tip of the Agulhas bank, where the Agulhas Current detaches from the topographic control.
- Shear edge eddies that are formed on the eastern Agulhas Bank, where the Agulhas Current overshoots the concave part of the shelf break.

This analysis of the model outputs gives confidence in the validity of the simulation. A set of experiments has been set up to study the transport patterns of sardines and anchovies from the spawning area of the western Agulhas Bank to the nursery ground of St Helena Bay. A passive tracer has been released at different times of the simulation. Each 'tracer simulation' has been conducted for 3 months. The amount of tracer that manages to reach St Helena Bay is highly dependent on the date of the release. If the tracer release occurs before the upwelling season, it fills slowly St. Helena Bay. An important portion of tracer is still along the West Coast after 3 months. On the contrary, if the tracer release is done during the upwelling season, though the tracer arrives very quickly in the West Coast, it is also rapidly carried away by the Ekman transport. If the release occurs after the upwelling season the amount of tracer in St. Helena Bay increases again. During the upwelling season, the loss of tracer is more important for the low resolution experiment than for the high resolution experiment. This reveals that the mesoscale activity is able to counter the effects of the offshore Ekman transport, or that the along shore jets responsible of transport are not well reproduced for the low resolution experiment.